RESULTS AND DISCUSSION

The present research work entitled "***Rational design, synthesis, in-silico screening and evaluation of some heterocyclic compounds as neurotherapeutic agents***" aimed to design new chemical entities fulfilling the structural requirements as multi-target-directed-ligands possessing multifunctional monoamine oxidase and acetylcholinesterase inhibitory activities. The various aspects of synthetic work, characterization and biological testing results for each series of synthesized compounds are discussed below.

5.1. 2-AMINO-6-NITROBENZOTHIAZOLE DERIVED EXTENDED HYDRAZONES [BTA-1 to BTA-30]

5.1.1. Synthesis

2-Amino-6-nitrobenzothiazole derived extended hydrazones (**BTA-1** to **BTA-30**) were obtained by refluxing hydrazide with appropriate aldehyde or ketone according to the reaction scheme depicted in **Scheme 4.4.**, by optimizing the various reaction variables, viz. solvents, catalyst, temperature, stirring time, etc.

All the final products were stable to open air environment. The intermediates (**BTE** and **BTH**) and final products were obtained in good yields (50 to 86%) except compounds **BTA-2** (49.42%), **BTA-4** (48.33%), **BTA-8** (48.59%), **BTA-20** (48.57%), **BTA-22** (46.08%), **BTA-23** (36.72%) and **BTA-26** (23.98%).

All the products (**BTA-1** to **BTA-30**) were obtained as crystalline solids. The final compounds were of yellow (**BTA-1** to **BTA-24** and **BTA-30**), reddish brown (**BTA-25**), maroon (**BTA-26** to **BTA-28**) or dark brown (**BTA-29**) colour. The final compounds were recrystallized using ethanol as a solvent.

5.1.2. Characterization

5.1.2.1. Physicochemical characterization

5.1.2.1.1. Melting point

Melting points were determined in one end open capillary tubes on Sonar melting point apparatus and were uncorrected. All the synthesized compounds displayed a phase

change from solid to liquid state and thus exhibited melting range between 2 to 5 °C indicating the purity of compounds. The observed melting point ranges for the synthesized compounds **BTA-1** to **BTA-30** are presented in the **Table 4.4.**

5.1.2.1.2. Solubility

The solubility of all the synthesized compounds was determined in number of solvents at room temperature. All intermediates (**BTE** and **BTH**) and final compounds (**BTA-1** to **BTA-30**) were insoluble in water and chloroform but soluble in methanol and ethanol (a few required slight warming), DMSO and DMF. The isatin fragments **ISN-1**, **ISN-2** and **ISN-3** were soluble in chloroform, methanol and ethanol in addition to DMSO and DMF. The observed solubility data is listed in **Table 4.4.**

5.1.2.1.3. Thin layer chromatography

Thin layer chromatography (TLC) was performed during the synthesis to monitor the progress of the reaction. For each reaction, single distinct spot of product and absence of reactant spot in TLC analysis indicated the completion of reaction and the purity of synthesized compounds. TLC was also performed for the final compounds (**BTA-1** to **BTA-30**) after purification to determine their R_f values. The observed R_f values are presented in the **Table 4.4.** Depending upon the polarity of compounds, the composition of eluents used for TLC analysis were (i) Chloroform: Methanol: Toluene (8:2:1); (ii) Chloroform: Methanol: Toluene (8:1:2).

5.1.2.1.4. Determination of partition coefficient (LogP)

The synthesized compounds were found to exhibit experimental LogP values in the range 1.2 – 3.9 (Shake flask method) indicating that they possess adequate lipophilicity necessary for their solubility in the lipid phase. The experimental (determined through Shake flask method) and calculated LogP (software generated) values are listed in **Table 4.4.**

5.1.2.2. Spectral characterization and elemental analysis

5.1.2.2.1. Ultraviolet (UV) spectroscopy

All the compounds showed prominent absorption bands with respect to the chromophore. The compounds of **BTA** series exhibited absorption bands due to C=N and C=O chromophores at λ_{max} 250-300 nm and 290-393 nm respectively owing to $n \rightarrow \pi^*$ transition.

5.1.2.2.2. Infrared (IR) spectroscopy

The extended hydrazones showed characteristic absorption in the functional group region at 3200-3550 cm^{-1} and 1600-1700 cm^{-1} which confirmed the presence of NH (str) and C=O (str) of the amide (hydrazino linker) respectively. Further, formation of extended hydrazones was confirmed by the presence of strong stretching of -C=N at 1520-1640 cm^{-1} due to imine (C=N str) group. The presence of characteristic absorptions around **2850-3000 cm^{-1}** (**BTA-1** to **BTA-30**) confirmed the presence of **CH_2 stretching**. The characteristic absorption in the range 1300-1460 cm^{-1} and 1500-1560 cm^{-1} confirmed the presence of Ar-NO_2 (str) while the absorption in the range 1150-1300 cm^{-1} confirmed the presence of C-N (str) respectively. The presence of OH (str) and OCH_3 (str) was confirmed by the presence of absorption in the range 3400-3700 cm^{-1} (**BTA-6**, **BTA-9**, **BTA-12** and **BTA-24**) and 1000-1300 cm^{-1} (**BTA-13**, **BTA-18**, **BTA-19** and **BTA-20**) respectively. The presence of C=O group of indole ring of isatin was confirmed by the characteristic absorption in the range 1680-1740 cm^{-1} (**BTA-28** to **BTA-30**).

The presence of halogens was confirmed by the absorptions in the range of 500-850 cm^{-1} for C-Cl (**BTA-4**, **BTA-15**, **BTA-16**, **BTA-17**, **BTA-21**, **BTA-23**, **BTA-25** and **BTA-29**) and C-Br (**BTA-3, BTA-10** and **BTA-26**) and 950-1200 cm^{-1} for C-F (**BTA-5**) groups.

5.1.2.2.3. Nuclear magnetic resonance (NMR) spectroscopy

^{1}H NMR spectra of all the 2-amino-6-nitrobenzothaizole derived extended hydrazones showed a characteristic singlet peak at δ 6.26-7.75 ppm and δ 8.37-8.69 ppm indicating –NH– and –CONH– protons, respectively. The singlet at δ 7.40-8.45 ppm (**BTA-8** to **BTA-21**), δ 2.21-2.91 ppm (**BTA-1** to **BTA-7**) and **δ 3.34-4.12 ppm** (**BTA-1** to **BTA-30**) indicated the C-H, C-CH_3 and **CH_2** protons respectively. The appearance of multiplets at δ 8.01-8.98 ppm, δ 6.54-8.54 ppm and δ 6.35-8.62 ppm confirmed the presence of benzothiazole (**BTA-1** to **BTA-30**), aromatic (**BTA-2** to **BTA-26**) and isatinyl (**BTA-28** to **BTA-30**) protons respectively. Singlet at δ 2.91 ppm indicated the presence of N-CH_3 protons (**BTA-11**). In ^{1}H NMR spectra of extended hydrazones having indolyl group, a singlet was observed at δ 10.33-10.99 ppm (**BTA-28** and **BTA-30**) due to >NH of indole ring. The singlet at δ 3.87-3.91 ppm (**BTA-13**, **BTA-18** to **BTA-20**) and δ 4.46-5.12 ppm (**BTA-6**, **BTA-9**, **BTA-12** and **BTA-24**) indicated the presence of OCH_3 and OH protons, respectively. The disappearance of signals of amino

NH and carbimino NH indicated the presence of exchangeable protons (**BTA-7**; **Figure 4.7.**)

In ^{13}C NMR spectra of extended hydrazones, the appearance of signals in the range of δ 158.20-158.96 ppm confirmed the presence of carbonyl group. Moreover, ^{13}C NMR spectra showed signals in the range of δ 140.84-160.68 ppm which was due to C=N carbon. Characteristic signals at δ 13.98-23.35 ppm (**BTA-1** to **BTA-7**, **BTA-11**), **δ 76.88-79.91** (**BTA-1** to **BTA-30**), δ 167.72-167.83 ppm (**BTA-28** to **BTA-30**) and δ 23.48-29.38 ppm (**BTA-27**) corresponded to CH_3, **CH_2,** oxindole C=O and cyclohexyl CH_2 respectively. Clustered signals in the range δ 112.63-171.74 ppm corresponded to the presence of benzothiazole and aromatic carbons (**BTA-1** to **BTA-30**). The presence of $–OCH_3$ groups was also confirmed by presence of signals in the range of δ 56.05–56.95 ppm (**BTA-13**, **BTA-18** to **BTA-20**).

5.1.2.2.4. Mass spectrometry

Compounds **BTA-26** and **BTA-28** were subjected to mass analysis. **BTA-26** (Mol. wt. = 527.19) showed an $[M+1]^+$ peak at 528.42 while the presence of 2 atoms of bromine was indicated by the [M+2] and [M+4] peaks at 529.89 and 532.02 respectively (**Figure 4.25.**). **BTA-28** (Mol. wt. = 396.38) showed an $[M+1]^+$ peak at 397.65 (**Figure 4.29.**), thereby confirming the structure of the compounds.

5.1.2.2.5. Elemental analysis

All the compounds **BTA-1** to **BTA-30** were subjected to elemental analysis and the observed values were within ± 0.4% of the calculated values.

5.1.2.2.6. Powder X-ray diffraction analysis

N'-(2,6-dichlorobenzylidene)-2-(6-nitrobenzothiazol-2-ylamino)acetohydrazide (**BTA-17**) was subjected to the powder X-ray diffraction analysis to confirm the crystallinity of the compound. The diffraction pattern of **BTA-17** (**Figure 4.15.**) indicated the crystalline nature of the compound.

5.1.3. Biological evaluation

5.1.3.1. MAO enzyme inhibition studies

5.1.3.1.1. *In-vitro* MAO inhibition assay

The *in-vitro* activity of 2-amino-6-nitrobenzothiazole derived extended hydrazones **BTA-1** to **BTA-30** against MAO isozymes was determined using crude rat brain mitochondrial

suspensions by a UV-based spectrophotometric method. Clorgyline and selegiline were used as reference inhibitors for MAO-A and MAO-B respectively (**Table 5.1.**).

Table 5.1. *In-vitro* and computational MAO inhibition data for **BTA-1** to **BTA-30**

Code	MAO-A			MAO-B			SI[a]
	In-vitro	Computational		*In-vitro*	Computational		
	IC_{50} (µM) ± SEM	ΔG*	K_i (µM)	IC_{50} (µM) ± SEM	ΔG*	K_i (µM)	
BTA-1	7716 ± 12.69	-5.84	52.25	137.80 ± 5.81	-5.18	159.85	55.99
BTA-2	82.82 ± 7.83	-6.32	23.31	4.68 ± 0.62	-6.94	8.12	17.69
BTA-3	0.42 ± 0.003	-7.59	2.71	0.097 ± 0.002	-6.81	10.14	4.33
BTA-4	9.99 ± 0.034	-6.07	35.27	1.14 ± 0.013	-6.38	21.13	8.76
BTA-5	2.39 ± 0.008	-6.66	13.15	0.088 ± 0.007	-7.03	7.01	27.16
BTA-6	7.25 ± 0.003	-6.86	9.3	0.59 ± 0.014	-7.22	5.09	12.29
BTA-7	181.0 ± 0.921	-5.3	130.69	10.62 ± 0.009	-5.83	53.21	17.04
BTA-8	1272 ± 7.84	-5.85	51.66	1.472 ± 0.003	-6.7	12.26	864.13
BTA-9	47.81 ± 3.86	-6.29	24.45	4.68 ± 0.028	-6.12	32.79	10.22
BTA-10	23.37 ± 2.99	-5.53	89.13	1.39 ± 0.017	-6.45	18.76	16.81
BTA-11	1780 ± 9.87	-5.82	53.79	13.40 ± 0.075	-5.49	94.32	132.84
BTA-12	19.99 ± 4.52	-6.36	21.86	1.85 ± 0.001	-6.36	21.9	10.80
BTA-13	52.46 ± 1.32	-6.71	11.97	1.99 ± 0.005	-6.36	21.96	26.36
BTA-14	16.40 ± 0.26	-6.62	13.97	5.46 ± 0.014	-5.0	217.66	3.00
BTA-15	1.005 ± 0.008	-7.32	4.28	1.043 ± 0.008	-6.68	12.66	0.96
BTA-16	19.87 ± 0.25	-5.91	46.29	0.071 ± 0.001	-6.86	9.5	279.86
BTA-17	2.55 ± 0.007	-6.55	15.77	0.022 ± 0.004	-7.04	6.88	115.91

BTA-18	263.7 ± 6.79	-6.01	39.38	2.07 ± 0.012	-6.36	21.63	127.39
BTA-19	323.31 ± 11.31	-4.08	1010	4.52 ± 0.016	-5.96	42.73	71.53
BTA-20	7114 ± 15.29	-3.59	2330	14.95 ± 0.011	-5.3	129.87	475.85
BTA-21	579.9 ± 9.85	-5.64	103.05	2.84 ± 0.003	-6.31	23.85	204.19
BTA-22	87.90 ± 4.76	-7.83	1.83	0.0044 ± 0.0002	-7.79	1.95	19977.27
BTA-23	2.06 ± 0.037	-6.63	13.87	0.019 ± 0.001	-7.75	2.09	108.42
BTA-24	4.31 ± 0.045	-6.91	8.56	0.53 ± 0.005	-7.26	4.75	8.13
BTA-25	9.54 ± 0.017	-6.31	23.86	0.73 ± 0.003	-7.39	3.81	13.07
BTA-26	9.26 ± 0.013	-6.51	16.97	3.26 ± 0.001	-6.18	29.43	2.84
BTA-27	NT	-5.88	48.64	NT	-6.6	14.52	-
BTA-28	1.82 ± 0.003	-6.92	8.4	0.135 ± 0.0002	-6.83	9.8	13.48
BTA-29	1.38 ± 0.002	-7.2	5.31	0.0018 ± 0.0003	-7.78	1.97	766.67
BTA-30	19.75 ± 0.016	-6.25	26.09	2.25 ± 0.0018	-6.33	23.05	8.78
CLG	0.0044 ± 0.462	-	-	-	-	-	-
SEL	67.25 ± 1.02	-	-	0.020 ± 0.0008	-	-	-
HRM	3.00	-5.3	130.82	7000	-	-	-
SAF	-	-	-	0.100	-5.93	45.23	-

*ΔG is expressed in $kcalmol^{-1}$; Reference inhibitors: CLG: Clorgyline, SEL: Selegiline, HRM: Harmine, SAF – Safinamide; [a]SI – The selectivity index is the selectivity for the MAO-B isoform and is given as the ratio of experimental IC_{50}(MAO-A)/IC_{50}(MAO-B); NT: Not tested.

NOTE: Each IC_{50} value is the mean ± SEM. It refers to the assay concentration of test compound which leads to 50% inhibition of enzyme activity. Level of statistical significance: $P < 0.05$ versus the corresponding IC_{50} values obtained against MAO-A and MAO-B, as determined by ANOVA/Dunnett's.

The inhibition data are expressed in terms of IC_{50} values (**Table 5.1.**). The IC_{50} values suggested that most of these molecules were selective inhibitors of MAO-B with their

inhibitory activities in the nanomolar to micromolar range. The IC_{50} values were in the range 0.42 ± 0.003 µM (**BTA-3**) to 7716 ± 12.69 µM (**BTA-1**) for MAO-A, and 0.0018 ± 0.0003 µM (**BTA-29**) to 137.80 ± 5.81 µM (**BTA-1**) for MAO-B. Incorporation of methylene spacer onto the semicarbazone template resulted in increased inhibition and selectivity towards MAO-B compared to MAO-A, whereas structural variations attempted at the carbimino terminal by incorporation of monoaryl or diaryl or isatin residue in all compounds of the series generally resulted in variations in the activity.

Among the synthesized compounds, N'-(1-(4-bromophenyl)ethylidene)-2-(6-nitrobenzothiazol-2-ylamino)acetohydrazide (**BTA-3**) was found to be most active MAO-A inhibitor with IC_{50} value of 0.42 ± 0.003 µM, whereas the most active MAO-B inhibitor, N'-(5-chloro-2-oxoindolin-3-ylidene)-2-(6-nitrobenzothiazol-2-ylamino)aceto-hydrazide (**BTA-29)** was found to exhibit an IC_{50} value of 0.0018 ± 0.0003 µM with the selectivity index of 766.67 against MAO-B in the study, followed by N'-(diphenylmethylene)-2-(6-nitrobenzothiazol-2-ylamino)acetohydrazide (**BTA-22**, IC_{50} = 0.0044 ± 0.0002 µM) with the selectivity index of 19977.27 against MAO-B. On comparing the potency of these compounds to the reference inhibitor, it was found that compound **BTA-29** was ~11-fold and compound **BTA-22** was ~4.5-fold more potent than selegiline.

The *in-vitro* MAO inhibitory data (**Table 5.1.)** suggested that structural variations attempted at the imino terminal of the hydrazone scaffold (in terms of hydrophobic sites) resulted in interesting inhibitory profile against both the isozymes.

SAR for MAO-A inhibition

- Among the compounds **BTA-1** to **BTA-30**, the presence of CH_3 or phenyl ring at R^1 and a halogen substituted phenyl ring at R^2 favoured MAO-A inhibition than others.

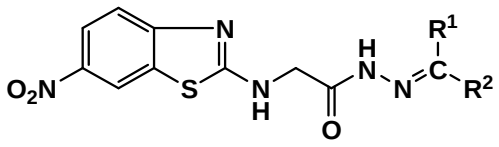

BTA-1 to BTA-27

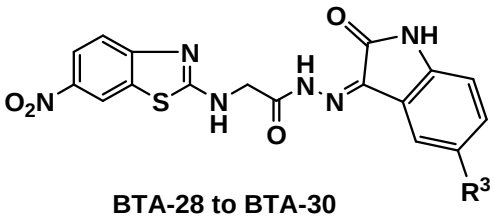

BTA-28 to BTA-30

- The monoaryl and methyl or diaryl substitution yielded better inhibition than dimethyl (**BTA-1**) or diphenyl (**BTA-22**) or monoaryl substitutions (**BTA-2** and **BTA-8**).

- Among the monoaryl and methyl (**BTA-2** to **BTA-7** and **BTA-26)** or diaryl (**BTA-18** to **BTA-21**) derivatives (R^1 and R^2), the bromo (**BTA-3**) and chloro (**BTA-23**) substituents showed superior MAO-A activity while with nitro (**BTA-7**) substituent caused a dramatic decrease in the activity.

- Further, among the monoaryl derivatives with –H at R^1, compounds with the bulky substituents such as NO_2 (**BTA-14**), OCH_3 (**BTA-13**, **BTA-18 to BTA-20**) and $N(CH_3)_2$ (**BTA-11**) groups caused a drastic decrease in the MAO-A inhibition. This clearly justifies the requirement of optimal hydrophobic feature in the form of aryl ring with less bulky and electronegative substituents (Br, F, Cl, in compounds **BTA-3**, **BTA-5** and **BTA-23**) for MAO-A inhibition.

- Replacement of isolated hydrophobic moieties with a large rigid hydrophobic isatinyl residue (**BTA-28** to **BTA-30**) retained the MAO-A activity with an exception of nitro derivative (**BTA-30**) which caused a decrease in the MAO-A activity.

SAR for MAO-B inhibition

- In general, better MAO-B inhibitory activity was observed by replacing H at R^1 with the CH_3 group (compare **BTA-3** to **BTA-6**, **BTA-26**, and **BTA-8** to **BTA-15**, **BTA-18** to **BTA-21**). However, compounds **BTA-16** (IC_{50} = 0.071 ± 0.001 µM) and **BTA-17** (IC_{50} = 0.022 ± 0.004 µM) were the exceptions, as they displayed excellent activity when R^1 = H.

- An increase in the methoxy substitutions on the phenyl ring at the imino terminal caused a decrease in inhibitory activity towards MAO-B (compare **BTA-13** with **BTA-18**, **BTA-19** and **BTA-20**).

- In contrast, fluoro (**BTA-5**, ~0.22 times less active than selegiline) or bromo (**BTA-3**, ~0.2 times less active than selegiline) or chloro (**BTA-4**) substitution at the para

position of the phenyl ring at R^2 on the imino terminal with the presence of CH_3 at R^1 increased inhibitory potency towards MAO-B.

- Hydroxyl substitution at para position on the phenyl ring at the imino terminal resulted in slight reduction in the activity (compounds **BTA-6** and **BTA-12**) whereas NO_2 substitution caused a further decrease in the inhibitory activity (compounds **BTA-7** and **BTA-14**) towards MAO-B.

- However, dichloro substitutions on the phenyl ring at R^2 with H at R^1 on the imino terminal increased the inhibitory activity of compounds (**BTA-17**, **BTA-16** and **BTA-15**). The ranking order of these dichloro derivatives observed was 2,6-Cl_2 (**BTA-17**, inhibition activity almost equivalent to selegiline) > 2,4-Cl_2 (**BTA-16**, ~0.28 times less active than selegiline) > 2,3-Cl_2 (**BTA-15**).

- Among the diphenyl substituted derivatives (**BTA-22** to **BTA-25**), unsubstituted derivative (**BTA-22**) was found to be the most active one (~4.54 times more active than selegiline) followed by 4-chloro (**BTA-23**, ~1.05 times more active than selegiline) and 4-hydroxy (**BTA-24**) substituted diphenyl derivatives, while dichloro substitution (**BTA-25**) reduced the activity slightly.

- Among the compounds **BTA-28** to **BTA-30**, 5-Cl derivative (compound **31**) was found to be highly potent against MAO-B (~11.11 times more active than selegiline) followed by its unsubstituted analog (**BTA-28**). However, 5-NO_2 substitution reduced the activity (**BTA-30**).

Thus, it was observed that introduction of the electron-withdrawing groups like Cl, F, Br on the hydrophobic aryl ring at the imino terminal increased the activity, while the presence of bulkier substituents such as methoxy, nitro and $N(CH_3)_2$ groups greatly reduced the MAO-B inhibition. Overall, incorporation of methylene ($–CH_2–$) spacer increased the potency of some hydrazones and selectivity of all the compounds against MAO-B.

5.1.3.1.2. Kinetic analysis of lead MAO inhibitors BTA-3 and BTA-29

To determine the type of inhibition mechanism of these compounds against rat brain MAO-A and MAO-B, kinetic studies were carried out with the representative lead MAO-A and MAO-B inhibitors, **BTA-3** and **BTA-29**, respectively. The type of inhibition was established from the analysis of Lineweaver-Burk reciprocal plots (**Figure 5.1.)** indicating the plot for compounds **BTA-3** (**Figure 5.1. (A)**) and **BTA-29** (**Figure 5.1. (B)**) to be linear and intersected at Y-axis (K_m increases while V_{max} remains unaffected), indicating a competitive type of inhibition for both **BTA-3** and **BTA-29** against MAO-A and MAO-B respectively. These results further proved that **BTA-3** and **BTA-29** were reversible MAO-A and MAO-B inhibitors respectively.

5.1.3.1.2.1. Determination of K_i

To get information regarding the strength of interactions between the enzyme and the inhibitor, the dissociation constant (K_i) was calculated for the inhibitor for each type of mode of inhibition. K_i values for competitive inhibitors **BTA-3** and **BTA-29** were computed using the GraphPad Prism software. The K_i value of 37.86 ± 0.125 nM was estimated for **BTA-3** against MAO-A and 3.997 ± 0.003 nM for **BTA-29** against MAO-B. On comparing the IC_{50} values with the K_i values, an 11-fold difference was observed for **BTA-3** and 0.45-fold difference was observed for **BTA-29** which reflects tight binding of these inhibitors to the enzyme.

5.1.3.1.3. Reversibility and irreversibility study

The lead MAO-A and MAO-B inhibitors, **BTA-3** and **BTA-29** respectively, were subjected to time-dependent inhibition studies to assess the reversibility of enzyme inhibition. The reversibility studies was carried out using the slightly modified method described by Legoabe *et al*. When **BTA-3** and **BTA-29** were preincubated with MAO-A and MAO-B enzymes respectively for various periods of time viz. 0, 15, 30 and 60 min; no time-dependent drop in the rates of MAO-A catalyzed oxidation of serotonin by **BTA-3** (**Figure 5.1. (C)**) and MAO-B catalyzed oxidation of benzylamine by **BTA-29** (**Figure 5.1. (D)**) was observed, indicating that the inhibition is reversible for both MAO-A and MAO-B at least for the time period of 60 min. Interestingly, an increase in the catalytic rates of MAO-A and MAO-B was observed with increase in the preincubation time of **BTA-3** and **BTA-29** with the respective enzymes.

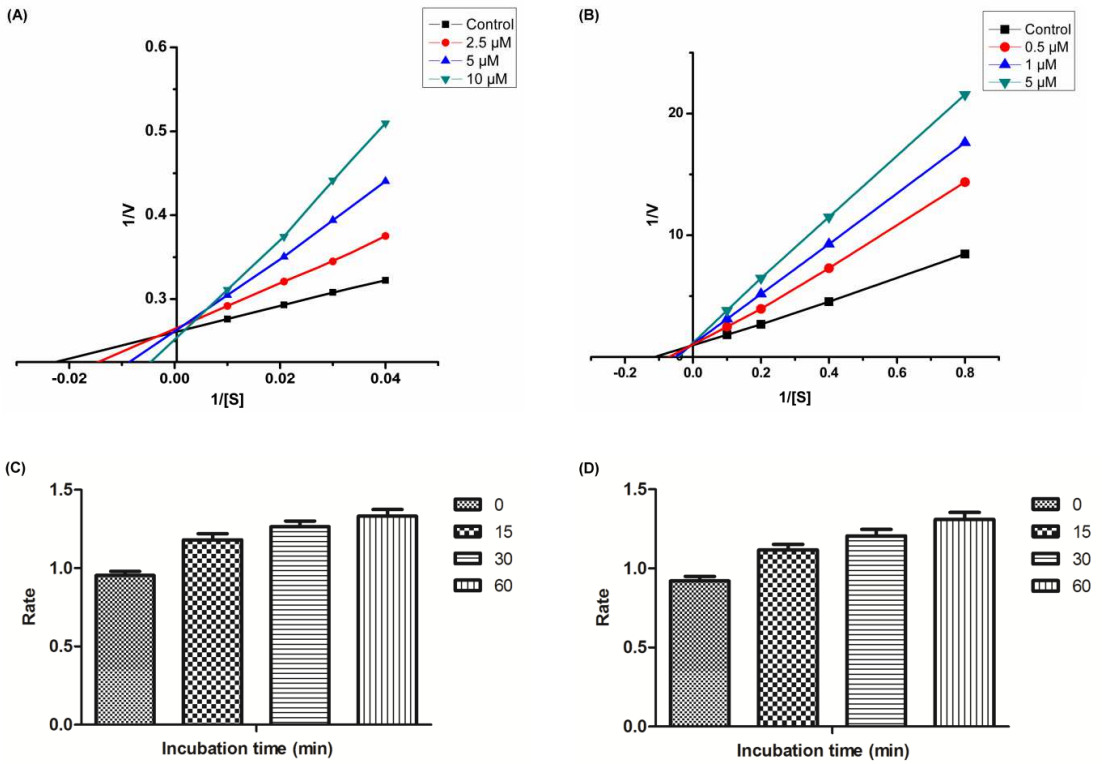

Figure 5.1. Kinetics of rat brain MAO-A inhibition by **BTA-3** and MAO-B inhibition by **BTA-29**. (A) Lineweaver-Burk plot of the rat brain MAO-A catalyzed oxidation of serotonin in the absence (control) and presence of various concentrations of **BTA-3** (2.5 µM, 5 µM, 10 µM). (B) Lineweaver-Burk plot of the rat brain MAO-B catalyzed oxidation of benzylamine in the absence (control) and presence of various concentrations of **BTA-29** (0.5 µM, 1 µM, 5 µM). Time-dependant MAO-A inhibition by **BTA-3** and MAO-B inhibition by **BTA-29** (C) MAO-A catalyzed oxidation of serotonin by **BTA-3** (D) MAO-B catalyzed oxidation of benzylamine by **BTA-29**. Rate data (V) are expressed as nmol product formed/min/mg protein.

5.1.3.1.4. Molecular modeling studies of MAO inhibitors

We proceeded to expand our investigation to this series of extended hydrazones against human MAO-A (hMAO-A) and human MAO-B (hMAO-B), in order to understand their interactions within the active site of MAO-A and MAO-B isozymes. Ligand docking studies were performed with AutoDock 4.2 using a single catalytic sub-unit of hMAO-A and hMAO-B isoforms. The co-crystallized structures of hMAO-A (PDB Code: 2Z5X) and hMAO-B (PDB Code: 2V5Z) was obtained from the Brookhaven Protein Data Bank. The conformers possessing the best score among the largest cluster were considered for further structural and binding interaction studies. The results of the docking studies were

expressed theoretically as binding free energies (ΔG) and inhibition constants (K_i values) for each of the ligand-protein complex and are presented in **Table 5.1.**

5.1.3.1.4.1. Binding pose analysis of MAO-A inhibitors

Evaluation of the virtual ligand-protein complexes of all compounds within the catalytic site of MAO-A resulted in the below mentioned interpretations: Particularly, all the test compounds occupied the active site cavity of MAO-A and were framed within the binding pocket surrounded by the amino acid residues Ile180, Asn181, Phe208, Val210, Gln215, Ile 325, Ile335, Phe352, Tyr407, Tyr444 and FAD which was almost similar to the reference MAO-A inhibitor, harmine (**Figure 5.2. (A)** and **(B)**). Compounds **BTA-1**, **BTA-3**, **BTA-4**, **BTA-5**, **BTA-6**, **BTA-7**, **BTA-26**, **BTA-9**, **BTA-10**, **BTA-12**, **BTA-13**, **BTA-14**, **BTA-15**, **BTA-17**, **BTA-19**, **BTA-21,** **BTA-23**, **BTA-24**, **BTA-25**, **BTA-28**, **BTA-29** and **BTA-30** (**Figure 5.2. (A)**); and **BTA-2**, **BTA-8**, **BTA-11**, **BTA-16**, **BTA-18**, **BTA-20** and **BTA-22** (**Figure 5.2. (B)**) shared a common binding orientation within the active site of MAO-A.

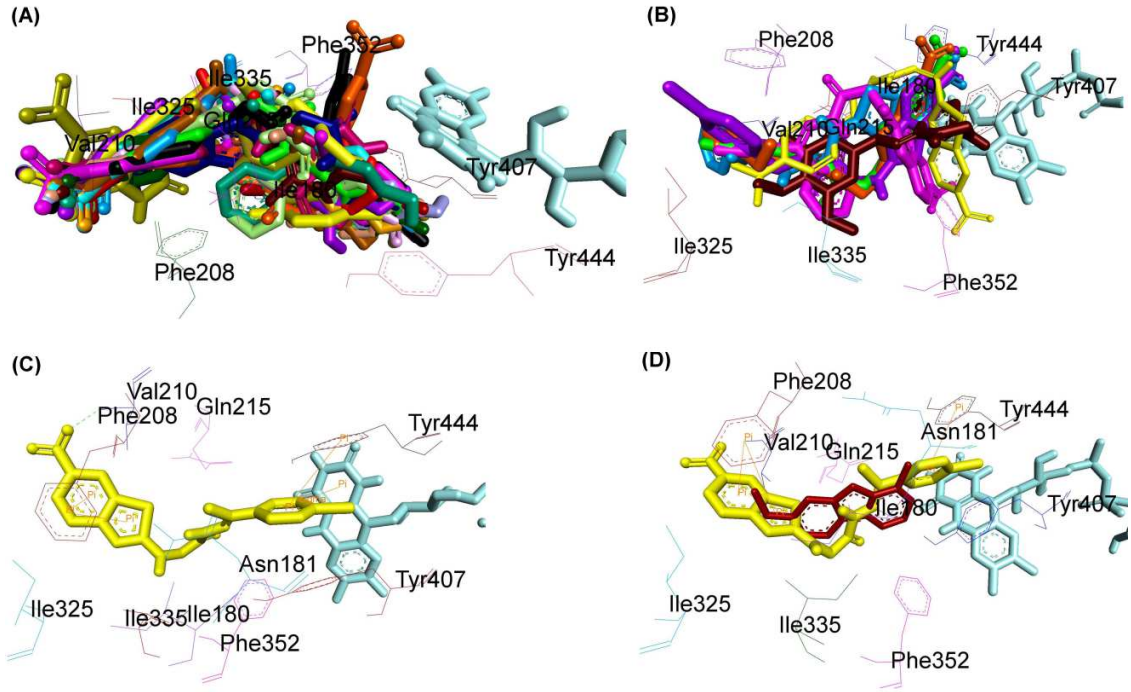

Figure 5.2. Structural screenshot of superimposed MAO-A inhibitors docked into the binding pocket of MAO-A. FAD is displayed in cyanin. Selected amino acids are depicted in black. (A) Shared binding orientation of **BTA-1**, **BTA-3**, **BTA-4**, **BTA-5**, **BTA-6**, **BTA-7**, **BTA-26**, **BTA-9**, **BTA-10**, **BTA-12**, **BTA-13**, **BTA-14**, **BTA-15**, **BTA-17**, **BTA-19**, **BTA-21,** **BTA-23**, **BTA-24**, **BTA-25**, **BTA-28**, **BTA-29** and **BTA-30** displayed in dark blue, dark brown, pink, dark green, light brown (sandy brown), orange,

maroon, fluorescent green, light blue, gray, light orange, light pink, fluorescent blue, red, light violet, yellow, light green, peacock green, black, dark pink, skin and dirty green color respectively. (B) Shared binding orientation of **BTA-2**, **BTA-8**, **BTA-11**, **BTA-16**, **BTA-18**, **BTA-20** and **BTA-22** displayed in sky blue, fluorescent green, yellow, violet, orange, dark brown and dark pink color respectively. (C) Binding orientation of **BTA-3** (yellow) within the MAO-A binding pocket showing π – π (orange colored lines) and H-bond (green dashes) interactions. (D) Superimposed binding orientation of **BTA-3** (yellow) within the MAO-A binding pocket originally docked with harmine (maroon).

In all the compounds of **Figure 5.2. (A)**, the 6-nitrobenzothiazole moiety is located towards the gateway of the MAO-A cavity while the hydrazino linker containing the arylidene or diarylmethylene or isatin residue occupied the centre of the cavity towards FAD. Whereas in all the compounds of **Figure 5.2. (B)**, the binding orientation is exactly the reverse i.e. the hydrazino linker containing the arylidene or diarylmethylene or isatin residue is situated towards the opening of the cavity space and the 6-nitrobenzothiazole moiety extended towards the FAD. Residues Tyr407, Tyr444 and FAD formed the bottom of the aromatic cage which is accountable to the binding orientation of the compounds and consequently their activity, binding affinity, selectivity and stability. In addition, almost all the inhibitors are stabilized by H-bond and π – π interactions.

In most of the potent compounds, preferably both H-bond and π – π interactions were found to be accountable for mediating inhibition against MAO-A isozyme. For our convenience, we focused our attention only on the binding mode of most active inhibitor **BTA-3**.

5.1.3.1.4.2. Binding mode of the lead MAO-A inhibitor BTA-3

The best-ranked docking solutions revealed that the active site of MAO-A can effectively accommodate the lead MAO-A inhibitor **BTA-3** (**Figure 5.2. (C)**) with 6-nitrobenzothiazole moiety positioned towards the entrance of the MAO-A cavity space while the 4-bromo phenyl moiety facing towards FAD and the hydrazino linker occupies the centre space of the cavity. The protein-inhibitor **BTA-3** complex was found to be stabilized mainly by the H-bond and π – π stacking interactions. The most energetically favourable binding mode of **BTA-3** within the active site of MAO-A is illustrated in **Figure 5.2. (C)**. In the complex, the benzene and thiazole ring of benzothiazole moiety of the ligand allowed a π – π stacking interaction with the phenyl ring of Phe208; likewise similar interaction has been found between the phenyl ring at the carbimino terminal and

the phenyl ring of Tyr444. An H-bond interaction between the oxygen of NO_2 of 6-nitrobenzothiazole allowed H-bond interaction with NH of Val210 is also observable. Further the docked pose of **BTA-3** (yellow) within the MAO-A binding pocket superimposed with the docked pose of harmine (maroon) is illustrated in **Figure 5.2. (D)** which indicated a similar binding pattern as that of reference inhibitor, harmine.

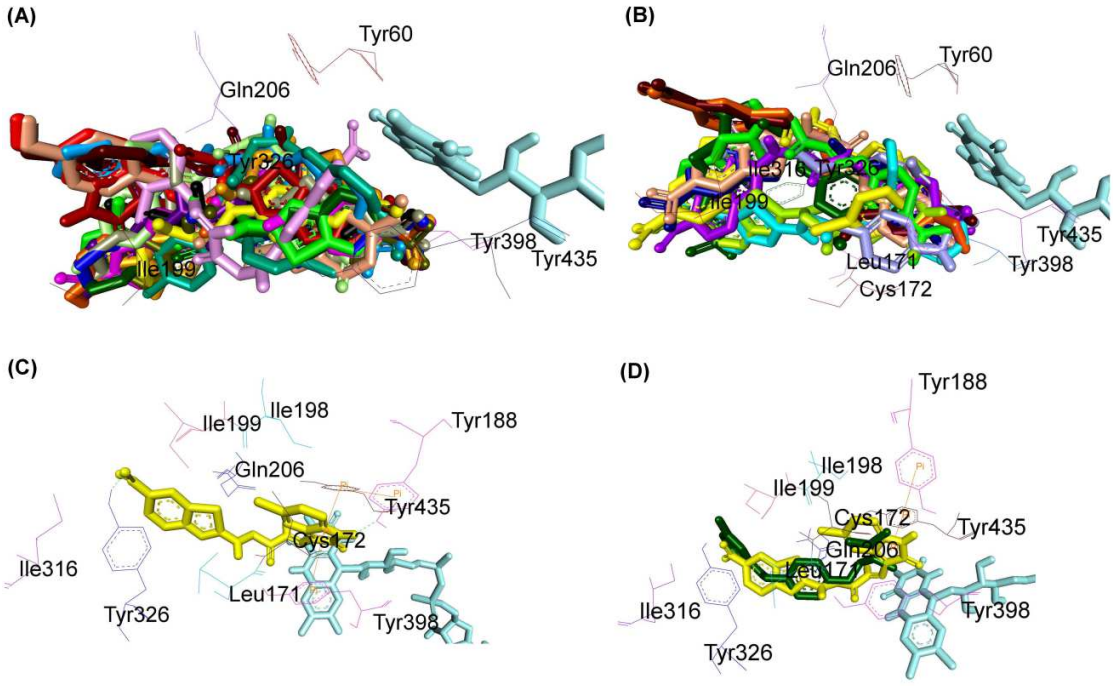

Figure 5.3. Structural screenshot of superimposed MAO-B inhibitors docked into the binding pocket of MAO-B. FAD is displayed in cyanin. Selected amino acids are depicted in black. (A) Shared binding orientation of **BTA-1**, **BTA-2**, **BTA-3**, **BTA-5**, **BTA-6**, **BTA-7**, **BTA-26**, **BTA-8**, **BTA-9**, **BTA-10**, **BTA-12**, **BTA-15**, **BTA-17**, **BTA-19**, **BTA-23**, **BTA-24**, **BTA-25** and **BTA-30** displayed in black, dark blue, dark brown, dark violet, red, dark pink, light green, dark green, sky blue, dirty green, dark orange, light pink, fluorescent green, light orange, gray, skin, peacock green and maroon color respectively. (B) Shared binding orientation of **BTA-4**, **BTA-11**, **BTA-13**, **BTA-14**, **BTA-16**, **BTA-18**, **BTA-20**, **BTA-21**, **BTA-22**, **BTA-28** and **BTA-29** displayed in dark blue, fluorescent green, dark orange, dark violet, skin, dark brown, dark green, yellow fluorescent blue, parrot green and light violet color respectively. (C) Binding orientation of **BTA-29** (yellow) within the MAO-B binding pocket showing $\pi - \pi$ (orange colored lines) and H-bond (green dashes) interactions. (D) Superimposed binding orientation of **BTA-29** (yellow) within the MAO-B binding pocket originally docked with safinamide (dark green).

5.1.3.1.4.3. Binding pose analysis of MAO-B inhibitors

All the inhibitors were accommodated within the catalytic binding pocket of MAO-B. The binding mode of all the test compounds within MAO-B traverses both the hydrophobic pockets, an entrance cavity bordered by the residues Leu171, Ile198, Ile199, Ile316 and Tyr326; and substrate cavity enclosed by the residues Tyr60, Cys172, Gln206, Tyr398 and Tyr435 which is almost analogous to the binding sites of safinamide, the reference MAO-B inhibitor (**Figure 5.3. (A)** and **Figure 5.3. (B)**). Compounds **BTA-1**, **BTA-2**, **BTA-3**, **BTA-5**, **BTA-6**, **BTA-7**, **BTA-26**, **BTA-8**, **BTA-9**, **BTA-10**, **BTA-12**, **BTA-15**, **BTA-17**, **BTA-19**, **BTA-23**, **BTA-24**, **BTA-25** and **BTA-30** (**Figure 5.3. (A)**); and **BTA-4**, **BTA-11**, **BTA-13**, **BTA-14**, **BTA-16**, **BTA-18**, **BTA-20**, **BTA-21**, **BTA-22**, **BTA-28** and **BTA-29** (**Figure 5.3. (B)**) shared a common binding orientation within the active site of MAO-B.

In all the compounds of **Figure 5.3. (A)**, the arylidene or diarylmethylene or isatin residue is located in the entrance cavity space of MAO-B while the 6-nitrobenzothiazole nucleus extended towards the substrate cavity facing FAD and the flexible hydrazino linker occupied the central region of the cavity of MAO-B. Whereas in all the compounds of **Figure 5.3. (B)**, the case is exactly the reverse i.e. the 6-nitrobenzothiazole scaffold lies in the entrance cavity of MAO-B and the arylidene or diarylmethylene or isatin residue is situated in the substrate cavity towards the FAD. Moreover, H-bond, $\pi - \pi$ stacking and hydrophobic interactions impart stability to these inhibitors.

All the compounds possessed H-bond interactions except **BTA-2**, **BTA-3**, **BTA-4**, **BTA-5**, **BTA-7**, **BTA-26**, **BTA-9**, **BTA-10**, **BTA-12**, **BTA-16**, **BTA-19**, **BTA-22**, **BTA-23** and **BTA-25**. H-bond interactions were observed with Glu84 for **BTA-6** and **BTA-24**; likewise with Pro102 for **BTA-30**; with Cys172 for **BTA-20** and **BTA-28**; with Tyr188 for **BTA-29**; with Ile198 for **BTA-8**, **BTA-15** and **BTA-17**; with Thr201 for **BTA-11**, **BTA-13** and **BTA-18**; with Gln206 for **BTA-1**, **BTA-11**, **BTA-20**, **BTA-21** and **BTA-30**; with Tyr326 for **BTA-1**, **BTA-11**, **BTA-14**, **BTA-17**, **BTA-29** and **BTA-30**; with Tyr435 for **BTA-15** and **BTA-17**; and with FAD for compound **BTA-15**. Also, all compounds showed $\pi - \pi$ interactions except **BTA-15**. $\pi - \pi$ interactions were observed with Tyr60 for **BTA-25**; likewise with Glu84 for **BTA-24**; with Tyr119 for **BTA-8**; with Tyr326 for **BTA-18**; with Tyr398 for **BTA-1**, **BTA-2**, **BTA-3**, **BTA-4**, **BTA-5**, **BTA-6**, **BTA-26**, **BTA-10**, **BTA-12**, **BTA-13**, **BTA-18**, **BTA-19**, **BTA-20**, **BTA-28**, **BTA-29** and **BTA-30**;

with Tyr435 for **BTA-2**, **BTA-3**, **BTA-4**, **BTA-5**, **BTA-7**, **BTA-26**, **BTA-8**, **BTA-9**, **BTA-10**, **BTA-11**, **BTA-14**, **BTA-16**, **BTA-17**, **BTA-19**, **BTA-23**, **BTA-28**, **BTA-29** and **BTA-30**; and with FAD for **BTA-25**. Additionally, π – σ interaction were observed with Phe168 for **BTA-22**; likewise with Ile199 for **BTA-21**; with Tyr326 for **BTA-19**; with Leu328 for **BTA-18**; and with FAD for **BTA-1**, **BTA-2**, **BTA-3**, **BTA-5**, **BTA-6**, **BTA-8**, **BTA-10**, **BTA-12**, **BTA-17** and **BTA-28**. Thus, in most of the potent compounds, preferably π – π stacking and H-bond interactions were found to be responsible for imparting stability and inhibition against MAO-B. For our convenience, we focused our attention only on the binding mode of the most active inhibitor **BTA-29**.

5.1.3.1.4.4. Binding mode of lead MAO-B inhibitor BTA-29

The most energetically favourable binding mode of **BTA-29**, shown in **Figure 5.3. (C)**, places the ligand within the active site cavity of MAO-B occupying the entrance and substrate binding sites. Docking simulations showed a clear preference to accommodate the 6-nitrobenzothiazole moiety within the entrance cavity of MAO-B while the hydrophobic pocket forming the substrate cavity is embedded by the 5-chloroisatin moiety facing towards the FAD and the flexible hydrazino linker lies in the central region of the active cavity space. The main stabilizing factors that keep stable the protein-ligand complex were found to be the hydrophobic contacts, π – π stacking and hydrogen bonding interactions. In the complex, the 5-membered ring of isatin moiety is stacked against the aromatic rings of Tyr398 and Tyr435. The oxygen atom of NO_2 of 6-nitrobenzothiazole scaffold is hydrogen bonded to H atom of OH of Tyr326; likewise H of NH of isatin is hydrogen bonded to oxygen of OH of Tyr188. Also, in this orientation, this complex is involved in hydrophobic contacts with Ile199, Tyr326 and Leu171. Because the addition of chlorine would enhance the lipophilicity of the heteroaryl ring at the carbimino terminal, these interactions may explain the observation that chlorine substitution enhances MAO-B inhibitory potency. These interactions as a whole resulted in the firmness of the ligand-protein complex. **Figure 5.3. (D)** illustrates the docked pose of **BTA-29** (yellow) within the catalytic site of MAO-B superimposed with the docked pose of safinamide (dark green) pointing out to the fact that **BTA-29** possess similarity in the binding mode with safinamide further supporting our findings.

5.1.3.2. AChE enzyme inhibition studies

5.1.3.2.1. *In-vitro* AChE inhibition assay

The *in-vitro* activity of extended analogs of 2-amino-6-nitrobenzothiazole derived hydrazones **BTA-1** to **BTA-30** against rat AChE was determined using a colorimetric method of Ellman *et al.*, with donepezil and tacrine as reference compounds (**Table 5.2.**). The results of AChE inhibition are expressed in terms of IC_{50} values.

Table 5.2. *In-vitro* and computational AChE inhibition data for **BTA-1** to **BTA-30**

Code	*In-vitro*	Computational	
	IC_{50} (µM) ± SEM	**ΔG***	**K_i (µM)**
BTA-1	73.70 ± 4.62	-5.03	204.8
BTA-2	16.36 ± 0.019	-5.55	85.54
BTA-3	11.84 ± 0.014	-5.57	81.97
BTA-4	19.01 ± 0.018	-5.1	182.07
BTA-5	8.09 ± 0.009	-5.55	85.51
BTA-6	15.03 ± 0.011	-5.46	99.66
BTA-7	7834 ± 10.97	-3.83	1560.0
BTA-8	4.65 ± 0.005	-5.73	63.52
BTA-9	2454 ± 1.98	-4.25	773.05
BTA-10	3.025 ± 0.002	-5.65	72.19
BTA-11	31.76 ± 0.17	-5.47	98.22
BTA-12	2.093 ± 0.006	-5.98	41.09
BTA-13	18.19 ± 0.015	-5.3	130.53
BTA-14	96.48 ± 0.038	-4.72	348.15
BTA-15	43.74 ± 0.024	-5.1	183.04

BTA-16	164.5 ± 1.32	-4.47	526.62
BTA-17	1.95 ± 0.004	-6.02	38.95
BTA-18	286.5 ± 2.29	-4.67	374.94
BTA-19	20.39 ± 0.007	-5.13	174.72
BTA-20	5850 ± 10.31	-4.09	997.12
BTA-21	0.84 ± 0.002	-6.8	10.38
BTA-22	0.3367 ± 0.001	-7.16	5.68
BTA-23	4.881 ± 0.008	-5.59	80.33
BTA-24	1.550 ± 0.012	-7.03	6.99
BTA-25	3.45 ± 0.009	-5.71	65.53
BTA-26	12.28 ± 0.013	-5.51	91.39
BTA-27	NT	NT	NT
BTA-28	1.302 ± 0.002	-6.57	15.18
BTA-29	0.035 ± 0.005	-7.01	7.22
BTA-30	2966 ± 3.68	-4.34	658.71
DPZ	0.021 ± 0.01	-6.01	39.45
TAC	0.225 ± 0.04	-	-

*ΔG values are expressed in kcal mol^{-1}; Reference inhibitors: DPZ: Donepezil, TAC: Tacrine; NT: Not tested. Each IC_{50} value is the mean ± SEM. Level of statistical significance: $P < 0.05$ versus the corresponding IC_{50} values obtained against AChE, as determined by ANOVA/Dunnett's.

From the AChE inhibition data some interesting SAR was obtained. The IC_{50} values suggested that all the synthesized compounds **BTA-1** to **BTA-30** displayed inhibitory activities in the nanomolar to micromolar range. The IC_{50} values were in the range 0.035 ± 0.005 µM (**BTA-29**) to 7834 ± 10.97 µM (**BTA-7**). Among the synthesized compounds, N'-(5-chloro-2-oxoindolin-3-ylidene)-2-(6-nitrobenzothiazol-2-ylamino)acetohydrazide (**BTA-29**) was obtained as the lead candidate showing highest inhibition

with IC_{50} value of 0.035 ± 0.005 µM, which was ~0.6 fold active compared to donepezil and ~6.43 fold stronger compared to tacrine; followed by **BTA-22** (N'-(diphenylmethylene)-2-(6-nitrobenzothiazol-2-ylamino)acetohydrazide) and **BTA-21** (N'-(4-(4-chlorobenzyloxy)benzylidene)-2-(6-nitrobenzothiazol-2-ylamino)acetohydrazide) with IC_{50} values of 0.3367 ± 0.001 µM and 0.84 ± 0.002 µM respectively. Among these three compounds, **BTA-29** and **BTA-21** possessed chloro group on the heteroaryl/aryl ring present at the carbimino terminal of the hydrazino template.

Structural variations attempted in all compounds of the series generally resulted in improvement in the activity. Incorporation of the $–CH_2–$ linker to the amino terminal of hydrazino template along with increase in the lipophilicity caused by the incorporation of monoaryl or diaryl rings or isatin residue at the carbimino terminal of the hydrazino template resulted in diverse inhibition against AChE.

A careful insight and analysis of the results of AChE inhibition activity presented in **Table 5.2.** led to several eventual structure-activity relationships (SAR).

Structure-activity relationship (SAR)

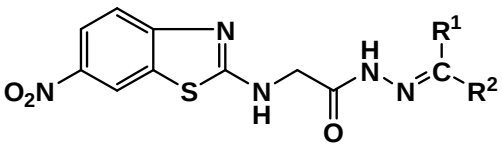

BTA-1 to BTA-27

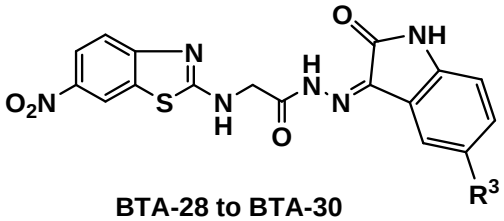

BTA-28 to BTA-30

- In general, improvement in AChE inhibitory activity was observed by substituting H at R^1 with the methyl group (compare **BTA-2**, **BTA-3**, **BTA-4**, **BTA-5**, **BTA-6**, **BTA-26** and **BTA-9**, **BTA-11**, **BTA-13**, **BTA-14**, **BTA-15**, **BTA-16**, **BTA-18**, **BTA-19**, **BTA-20**) with the exception of **BTA-21**, **BTA-17**, **BTA-12**, **BTA-10** and **BTA-8** which possess good activity.
- An increase in the methoxy substitutions on the phenyl ring at the carbimino terminus of hydrazino template decreased the activity towards AChE (compare **BTA-13**, **BTA-18**, **BTA-19**, **BTA-20**).

- In contrast, introduction of fluoro (**BTA-5**) or bromo (**BTA-10** and **BTA-3**) or chloro group (**BTA-4**) at the para position of the phenyl ring at R^2 along with the methyl group at R^1 increased potency with the exception of **BTA-10** and **BTA-21** which possess good activity when R^1 = H.
- Hydroxyl group substitution at para position on the phenyl ring at the carbimino terminus resulted in increase in the activity (**BTA-24**, **BTA-12** and **BTA-6**) whereas NO_2 group substitution reduced the activity (**BTA-14** and **BTA-7**).
- Further, dichloro substitutions on the phenyl ring at R^2 with H at R^1 expressed variations in activity of compounds (**BTA-15 to BTA-17**). The ranking order of dichloro derivatives was observed to be 2,6-Cl_2 (**BTA-17**) > 2,3-Cl_2 (**BTA-15**) > 2,4-Cl_2 (**BTA-16**).
- Among the diphenyl substituted derivatives (**BTA-22 to BTA-25**), unsubstituted derivative (**BTA-22**) was found to be the most active one followed their 4-hydroxy (**BTA-24**) and 4,4'- dichloro (**BTA-25**) analogs, while 4-chloro substitution (**BTA-23**) reduced the activity slightly.
- Among the isatin-3-substituted analogs **BTA-28 to BTA-30**, 5-Cl derivative (**BTA-29**) was found to be highly potent against AChE followed by its unsubstituted analog (**BTA-28**). However, 5-NO_2 substitution excessively reduced the activity (**BTA-30**).

Thus, it was observed that compounds bearing chloro and hydroxyl substituents on the heteroaryl/aryl ring at the carbimino terminal of the hydrazino template displayed better inhibitory potency against AChE while introduction of bulkier substituents such as methoxy or nitro groups reduced the activity. These results guided us towards the influence of the steric groups and electronic substituents on the AChE inhibitory profile.

5.1.3.2.2. Kinetic analysis of lead AChE inhibitor BTA-29

To determine the type of inhibition mechanism of these compounds against rat brain AChE, a kinetic study was carried out with **BTA-29**, the selected representative lead AChE inhibitor. The type of inhibition was established from the analysis of Lineweaver-Burk reciprocal plots (**Figure 5.4.**) showing both increasing slopes (decreased V_{max}) and intercepts (higher K_m) with higher inhibitory concentration suggesting a mixed-type of

AChE inhibition (**Figure 5.4.**) and therefore supporting the dual binding site of this compound. These results further proved that the **BTA-29** was reversible AChE inhibitor.

5.1.3.2.2.1. Determination of K_i

To get information regarding the strength of interactions between the enzyme and the inhibitor, the dissociation constant (K_i) was calculated for the inhibitor for each type of mode of inhibition. K_i value for mixed inhibitor **BTA-29** was computed using the GraphPad Prism software and was estimated to be 6.18 ± 0.005 nM.

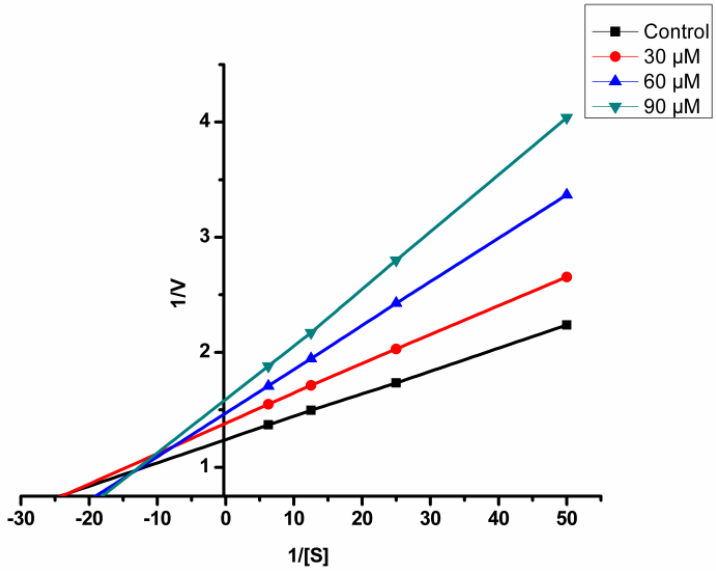

Figure 5.4. Kinetics of rat brain AChE inhibition by **BTA-29**. Lineweaver-Burk plot of the rat brain AChE catalyzed oxidation of ATCI in the absence (control) and presence of various concentrations of **BTA-29** (30 µM, 60 µM, 90 µM). Rate data are expressed as nmol product formed/min/mg protein.

5.1.3.2.3. Reversibility studies of lead AChE inhibitor BTA-29

The most active AChE inhibitor, **BTA-29**, was subjected to time-dependent inhibition studies to assess the reversibility of enzyme inhibition. When **BTA-29** was preincubated with AChE for various periods of time viz. 0, 15, 30 and 60 min; no time-dependent decrease in the rates of AChE catalyzed oxidation of ACTI by **BTA-29** was observed (**Figure 5.5.**), indicating that the inhibition is reversible for AChE at least for the time period of 60 min. Interestingly, an increase in the catalytic rates of AChE was observed with increase in the preincubation time of **BTA-29**.

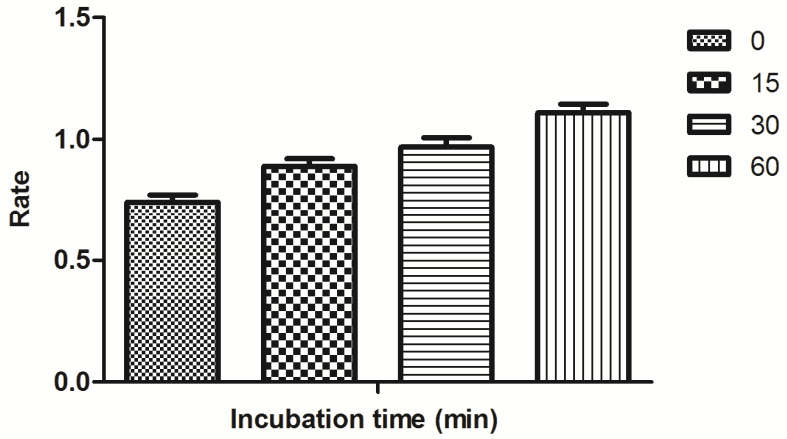

Figure 5.5. Time-dependant inhibition of AChE catalyzed oxidation of ACTI by **BTA-29**. Rate data are expressed as nmol product formed/min/mg protein.

5.1.3.2.4. Molecular modeling studies of AChE inhibitors

To further investigate the binding mode of the inhibitors, molecular docking study was carried out to this series of hydrazones against recombinant human AChE (rhAChE) using the automated docking program AutoDock 4.2 with a view to get information regarding the various molecular interactions of ligands within the active site gorge of AChE. The crystallographic structure of the recombinant human AChE (rhAChE) in complex with donepezil (PDB code: 4EY7) was retrieved from the Brookhaven Protein Data Bank (PDB). The conformers possessing the best score among the largest cluster were considered for further structural and binding interaction studies. The results of molecular docking studies for AChE stated in terms of estimated binding free energies (ΔG) and theoretical inhibition constants (K_i values) for each virtual rhAChE-inhibitor complex are listed in **Table 5.2.**

5.1.3.2.4.1. Analysis of AChE inhibitors

Inspection of the computationally docked binding poses of all compounds within the binding pocket of AChE resulted in the following consequences (observations/findings): All the test inhibitors were found to occupy the binding pocket of the gorge of AChE formed by catalytic anionic site (CAS) and peripheral anionic site (PAS) and were surrounded (enclosed) by the residues Asp74, Trp86, Gly121, Gly122, Tyr124, Gly126,

Tyr133, Ser203, Trp286, Phe295, Arg296, Phe297, Tyr337, Phe338, Tyr341 and His447 (**Figure 5.6.**). Almost in all the test inhibitors the 6-nitrobenzothiazole moiety binds to peripheral anionic site (PAS) while the arylidene or diarylmethylene or isatin residue present at the carbimino terminus of hydrazino scaffold is flipped towards the catalytic anionic site (**Figure 5.6. (A)**). This revealed that most of the test inhibitors exhibit the analogous orientation as the reference inhibitor, donepezil. However, a few exceptions are found with the inhibitors **BTA-2**, **BTA-3**, **BTA-4**, **BTA-8**, **BTA-10**, **BTA-11**, **BTA-12**, **BTA-16**, **BTA-19** and **BTA-20** for which the orientation is completely the reverse (**Figure 5.6. (B)**). Further, these inhibitors are stabilized by hydrogen bonding (H-bond) and hydrophobic interactions.

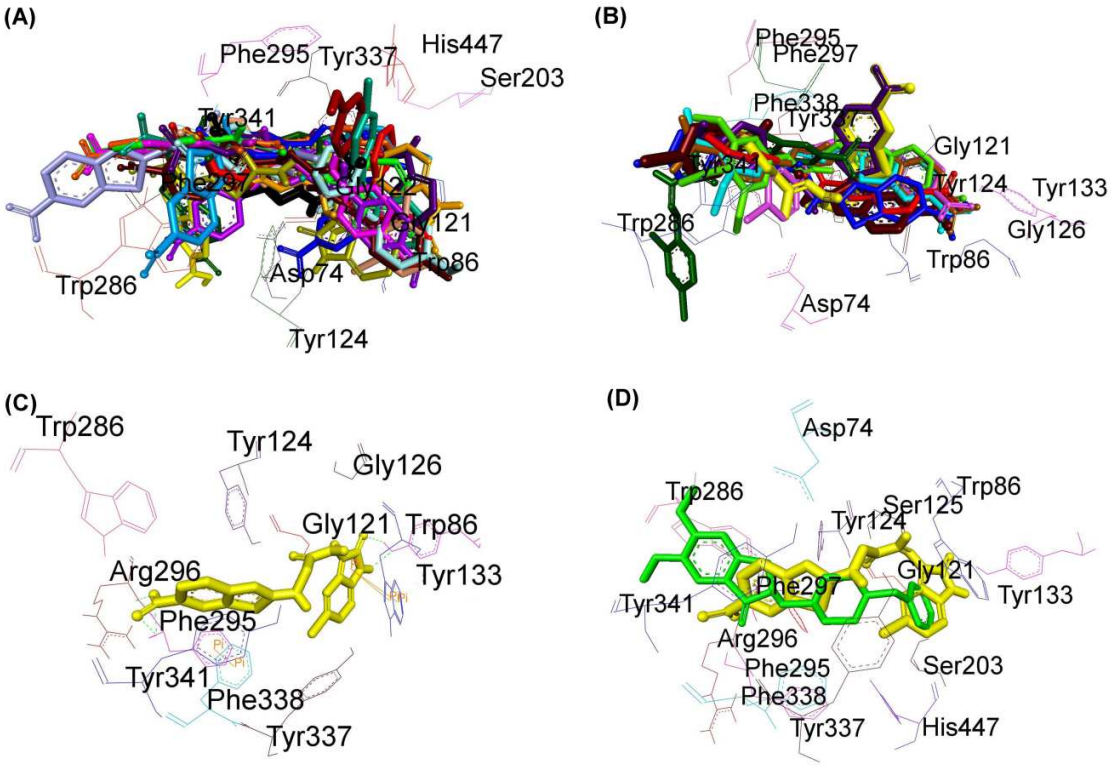

Figure 5.6. Structural screenshot of superimposed AChE inhibitors docked into the active site gorge of AChE. Selected amino acids are depicted in black. (A) **BTA-1**, **BTA-5**, **BTA-6**, **BTA-7**, **BTA-26**, **BTA-9**, **BTA-13**, **BTA-14**, **BTA-15**, **BTA-17**, **BTA-18**, **BTA-21**, **BTA-22**, **BTA-23**, **BTA-24**, **BTA-25**, **BTA-28**, **BTA-29** and **BTA-30** are displayed in black, dirty green, maroon, light violet, dark pink, orange, light blue, dark blue, fluorescent green, skin, gray, red, dark brown, light fluorescent blue, peacock green, dark violet, light orange, straw green and yellow color respectively. (B) **BTA-2**, **BTA-3**,

BTA-4, **BTA-8**, **BTA-10**, **BTA-11**, **BTA-12**, **BTA-16**, **BTA-19** and **BTA-20** are displayed in yellow, dark brown, dark blue, red, light pink, light brown, dark violet, dirty green, fluorescent blue and fluorescent green color respectively. (C) Binding orientation of **BTA-29** (yellow) within the active site gorge of AChE showing π – π (orange colored lines) and H-bond (green dashes) interactions. (D) Superimposed binding orientation of **BTA-29** (yellow) within the active site gorge of AChE originally docked with donepezil (fluorescent green).

All compounds showed one or more H-bond interactions. H-bond interaction with residue Thr75 is observed for **BTA-5** and **BTA-21**; likewise with Asp74 for **BTA-1**; with Gly120 for **BTA-24**; with Gly121, Gly122 and Ala204 for **BTA-2** and **BTA-12**; with Tyr124 for **BTA-7**, **BTA-12**, **BTA-14**, **BTA-23** and **BTA-30**; with Ser125 for **BTA-15**; with Tyr133 for **BTA-3**, **BTA-4**, **BTA-7**, **BTA-8**, **BTA-10**, **BTA-11**, **BTA-19**, **BTA-20**, **BTA-23**, **BTA-24**, **BTA-25**, **BTA-29** and **BTA-30**; with Trp286 for **BTA-12**, **BTA-19**, **BTA-20**, **BTA-22**, **BTA-25** and **BTA-28**; with Ser293 for **BTA-26**, **BTA-9** and **BTA-15**; with Phe295 for **BTA-1**, **BTA-5**, **BTA-6**, **BTA-26**, **BTA-14**, **BTA-15**, **BTA-17**, **BTA-18**, **BTA-21**, **BTA-22**, **BTA-23** and **BTA-29**; with Arg296 for **BTA-6**, **BTA-12**, **BTA-15**, **BTA-17**, **BTA-20**, **BTA-22**, **BTA-24**, **BTA-25**, **BTA-28** and **BTA-29**; with Ser298 for **BTA-13**; with Tyr337 for **BTA-28**; with Tyr341 for **BTA-3**, **BTA-5**, **BTA-6**, **BTA-16** and **BTA-21**; and with His447 for **BTA-9**, **BTA-10** and **BTA-14**. Moreover, all the compounds showed π – π interactions except **BTA-26**, **BTA-15**, **BTA-16**, **BTA-18**, **BTA-19** and **BTA-25**. π – π interaction with residue Tyr72 is observed for **BTA-21**; likewise with Trp86 for **BTA-3**, **BTA-8**, **BTA-10**, **BTA-14**, **BTA-21**, **BTA-24**, **BTA-28**, **BTA-29** and **BTA-30**; with Trp286 for **BTA-3**, **BTA-4**, **BTA-9** and **BTA-13**; with Tyr337 for **BTA-13**; with Phe338 for **BTA-5**; with Tyr341 for **BTA-1**, **BTA-6**, **BTA-7**, **BTA-10**, **BTA-11**, **BTA-17**, **BTA-20**, **BTA-23** and **BTA-24**; and with His447 for **BTA-2**. Moreover, π – cation interaction with His447 is found for **BTA-12**. Additionally, both the compounds **BTA-13** and **BTA-22** are stabilized by π – σ interaction with residues Trp86 and Phe297. Thus, in most of the potent compounds, preferably H-bond and π – π interactions have been found to be accountable for mediating inhibitory action against AChE. For our convenience, we focused our attention only on the binding mode of the most active inhibitors **BTA-29** and **BTA-22**.

5.1.3.2.4.2. Binding mode of lead AChE inhibitor BTA-29

Analysis of the optimal binding mode for **BTA-29** places the ligand within the active site cavity of rhAChE spanning both the cavities viz. PAS and CAS. Docking simulations showed a clear preference to accommodate the 6-nitrobenzothiazole moiety within the PAS while the binding pocket forming the CAS is embedded by the 5-chloroisatin moiety with the flexible hydrazino linker lying in the middle of the gorge between CAS and PAS. The main stabilizing factors that keep stable the enzyme-ligand complex were found to be the $\pi - \pi$ stacking and hydrogen bonding interactions. In the complex, the 5-membered ring of isatin moiety is stacked against both the aromatic rings of Trp86. In addition, the oxygen atom of C=O and H of NH of isatin is hydrogen bonded to H atom and oxygen atom respectively of OH of Tyr133; likewise similar interaction has been found between both the oxygen atoms of NO_2 of 6-nitrobenzothiazole scaffold and H of NH of Phe295. Further, an H-bond interaction between one of the oxygen atoms of NO_2 of 6-nitrobenzothiazole scaffold and H of NH of Arg296 is also observable (**Figure 5.6. (C)**). Besides, the higher potency of the molecule may be because of the addition of chlorine since it enhances the lipophilicity of the heteroaryl ring at the carbimino terminal of hydrazino template, these interactions may explain the observation that chlorine substitution enhances AChE inhibitory potency. These interactions as a whole resulted in the firmness of the ligand-enzyme complex. **Figure 5.6. (D)** illustrates the docked pose of **BTA-29** (yellow) within the active site gorge of AChE superimposed with the docked pose of donepezil (fluorescent green) pointing out to the fact that both contributes to the similarity in their binding mode.

5.1.3.3. Behavioural studies

5.1.3.3.1. Antidepressant activity (Forced swim test)

The synthesized compounds were evaluated for the antidepressant activity using Porsolt's forced swim test and the results are presented in **Figure 5.7.** Among the tested compounds, **BTA-3**, **BTA-15**, **BTA-17** and **BTA-29** were found to be more active than the reference drug citalopram, thereby indicating that these compounds produce no CNS depression. Rest of the compounds were found to emerge as CNS depressants as they increased the immobility time.

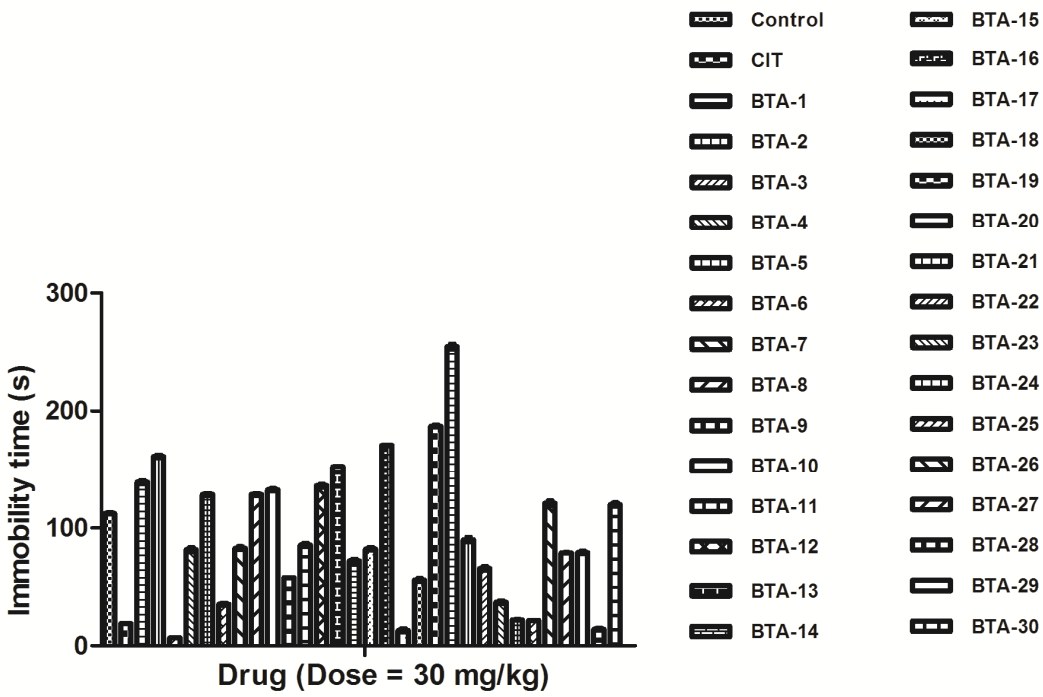

Figure 5.7. Antidepressant activity of 2-amino-6-nitrobenzothiazole derived extended hydrazones. The results are expressed as mean ± SEM (*n = 6*). The statistical significance was calculated by one-way ANOVA followed by Dunnett's test. CIT – Citalopram. *P < 0.001* when compared with the control group.

5.1.3.3.2. Anxiolytic activity (Elevated plus maze test)

All the compounds were subjected to anxiolytic activity using elevated plus maze apparatus and the results are presented in **Figure 5.8.** Compounds **BTA-3**, **BTA-26**, **BTA-22**, **BTA-23**, **BTA-24**, **BTA-28**, **BTA-29** and **BTA-30** possessed significantly greater anxiolytic potency than diazepam (DZM) while **BTA-12** and **BTA-14** expressed potency equivalent to diazepam. Rest of the compounds was found to be less active than diazepam.

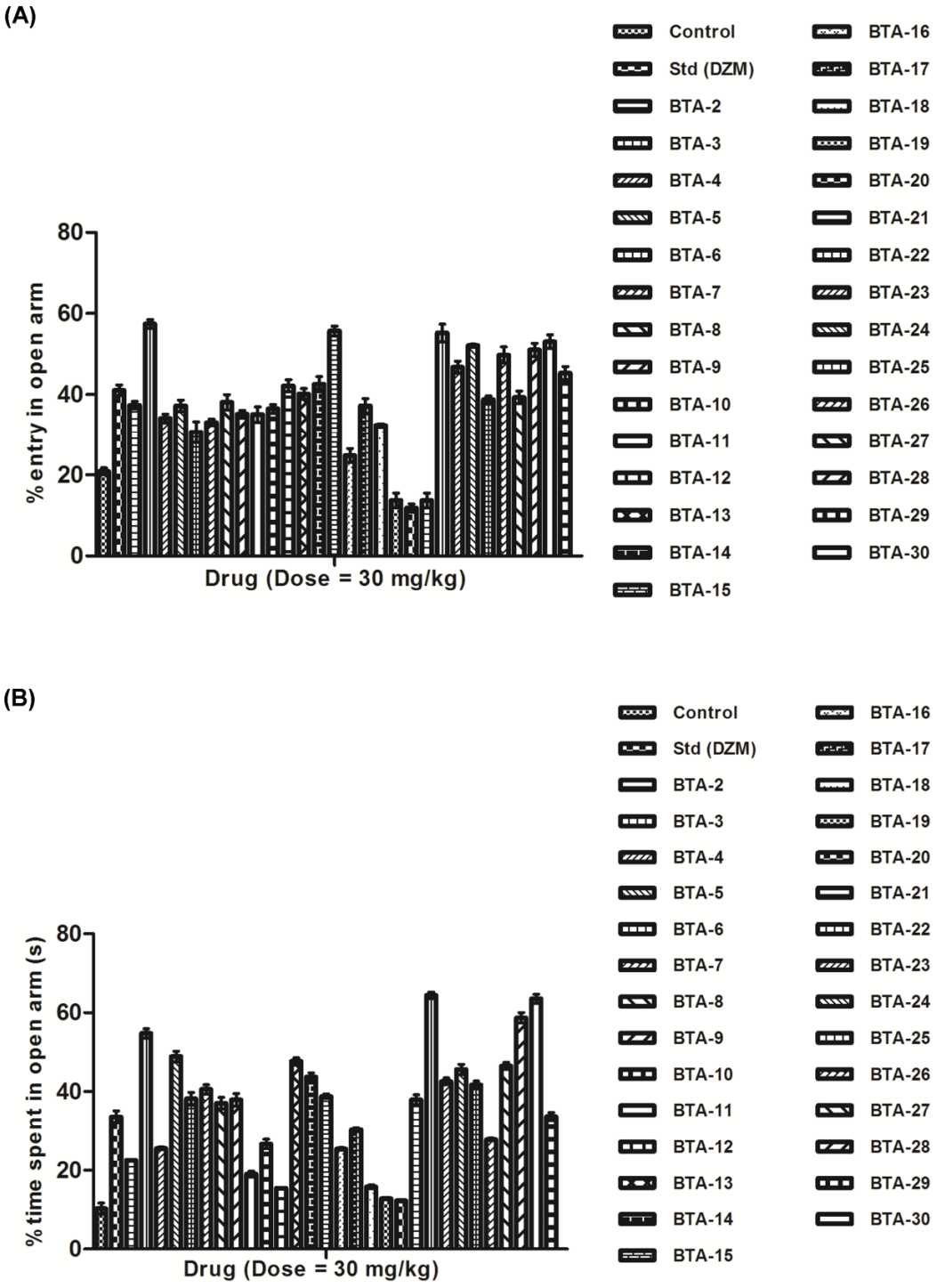

Figure 5.8. Anxiolytic activity of 2-amino-6-nitrobenzothiazole derived extended hydrazones. The results are expressed as mean ± SEM ($n = 6$). The statistical significance was calculated by one-way ANOVA followed by Dunnett's test. DZM – Diazepam. $P < 0.001$ when compared with control group.

5.1.3.3.3. Sedative-hypnotic activity (Pentobarbitone potentiation test)

All the synthesized compounds were evaluated in sedative and hypnotic test at a dose of 30 mg/kg and the results are presented in **Figure 5.9.** Most of the compounds showed significant variation from control. All the compounds resulted in elongation of mean sleeping time than control confirming that these compounds do not potentiate narcosis except **BTA-4**, **BTA-5**, **BTA-6**, **BTA-9**, **BTA-12**, **BTA-22** and **BTA-29**. Thus, the compounds **BTA-4**, **BTA-5**, **BTA-6**, **BTA-9**, **BTA-12**, **BTA-22** and **BTA-29** showed antagonistic properties to barbiturates indicating that they lack the sedative side effect. Rests of the compounds (except **BTA-4**, **BTA-5**, **BTA-6**, **BTA-9**, **BTA-12**, **BTA-22** and **BTA-29**) were found to potentiate narcosis.

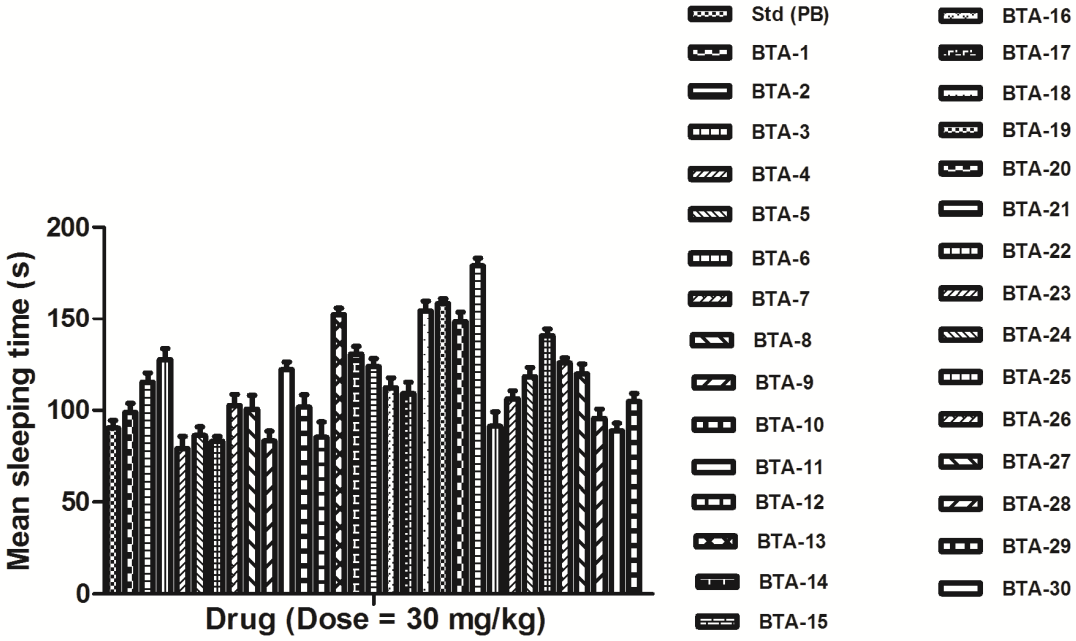

Figure 5.9. Sedative hypnotic activity of 2-amino-6-nitrobenzothiazole derived extended hydrazones. The results are expressed as mean ± SEM ($n = 6$). The statistical significance was calculated by one-way ANOVA followed by Dunnett's test. PB – Pentobarbitone. $P < 0.001$ when compared with control group.

5.1.3.4. Neurotoxicity screening (Rotarod test)

Selected compounds were screened for neurotoxicity by rotarod apparatus at a dose of 30 mg/kg at four time intervals viz. 0.5 h, 1 h, 2 h and 4 h. The results are presented in **Table 5.3.** Among the tested compounds, all compounds were found to be non-

neurotoxic except compounds **BTA-3, BTA-29** and **BTA-30** which were found to be mildly neurotoxic compared to standard drug phenytoin.

Table 5.3. Neurotoxicity screening results of selected compounds of **BTA** series

Code	Neurotoxicity (Time in h)*			
	0.5	**1**	**2**	**4**
BTA-3	2/4	0/4	0/4	1/4
BTA-5	0/4	0/4	0/4	0/4
BTA-6	0/4	0/4	0/4	0/4
BTA-16	0/4	0/4	0/4	0/4
BTA-17	0/4	0/4	0/4	0/4
BTA-22	0/4	0/4	0/4	0/4
BTA-23	0/4	0/4	0/4	0/4
BTA-24	0/4	0/4	0/4	0/4
BTA-25	0/4	0/4	0/4	0/4
BTA-28	0/4	0/4	0/4	0/4
BTA-29	1/4	0/4	0/4	0/4
BTA-30	0/4	1/4	2/4	0/4
PHT	0/4	0/4	0/4	0/2

* The figures indicate the number of animals exhibiting toxicity/total number of animals tested. Reference drug: PHT – Phenytoin

5.1.3.5. Antioxidant activity (DPPH radical scavenging assay)

The percentage antioxidant activity of some of the selected compounds is listed in **Table 5.4.** The DPPH· radical was scavenged by antioxidants *via* donation of hydrogen resulting in the formation of DPPH-H·. The colour of the DPPH is changed from purple to yellow after reduction, which was quantified by the decline of absorbance at a wavelength of 517 nm. From the experimental results, the enhancement in the antioxidant

activity is observed for all the tested compounds. Among the tested compounds, **BTA-3**, **BTA-10**, **BTA-26**, **BTA-28**, **BTA-29** and **BTA-30** showed more antioxidant activity (**Table 5.4.).**

Table 5.4. Antioxidant activity of selected compounds of **BTA** series

Code	% Inhibition	Code	% Inhibition
BTA-3	61.62	**BTA-22**	51.41
BTA-5	41.80	**BTA-23**	59.28
BTA-6	46.89	**BTA-24**	58.83
BTA-7	53.67	**BTA-25**	56.12
BTA-10	63.65	**BTA-26**	62.25
BTA-15	38.15	**BTA-28**	63.54
BTA-16	44.93	**BTA-29**	64.74
BTA-17	49.22	**BTA-30**	63.13
BTA-18	46.10	**Ascorbic acid**	61.24

The statistical significance was calculated by one-way ANOVA followed by Dunnett's test. $P < 0.05$ when compared with control.

5.1.3.6. Liver toxicity studies

Enzyme estimation and histopathological studies of the selected compounds were done to check the magnitude of liver toxicity.

5.1.3.6.1. Assessment of liver function

Table 5.5. shows the liver function tests with reference to most potent compound **BTA-29**. The estimation revealed that there was no significant increase in SGOT, SGPT, alkaline phosphatase and decrease in protein level in serum as compared to the control level (**Table 5.5.**). The results clearly indicated that **BTA-29** did not show any malfunctioning or toxicity of the liver as compared to control.

Table 5.5. Estimation of biochemical parameters of **BTA-29**

Code	SGOT[a] (U/L)	SGPT[b] (U/L)	ALP (U/L)[c]	Albumin (g/dl)	Globulin (mg/dl)	Total protein (g/dl)
Range	25.8-80.8	17.5-90	62-190	3.3-4.8	1.5-3.5	5.2-7.6
BTA-29	46.83 ±1.65	69.26±3.63	107.76±4.8	3.5±0.20	3.26±0.23	6.23±0.29
Control	38.56±1.62	51.73±2.17	151.56±2.75	3.9±0.12	1.86±0.14	6.8±0.17

Results are expressed as Mean ± SEM. The mean level was calculated using ANOVA followed by Dunnett's test; [a]Serum glutamate oxaloacetate transaminase (SGOT); [b]Serum glutamate pyruvate transaminase (SGPT); [c]Serum alkaline phosphatase (ALP)

5.1.3.6.2. Liver histopathological studies

The Lucas technique was used to access the livers of rat, which was administered with test compounds at the dose level of 30 mg/kg body weight for 15 days and a comparison was done with the control group. Liver samples from control group and **BTA-29** were within normal histopathological limits thus indicating that **BTA-29** was non-hepatotoxic (**Figure 5.10.**)

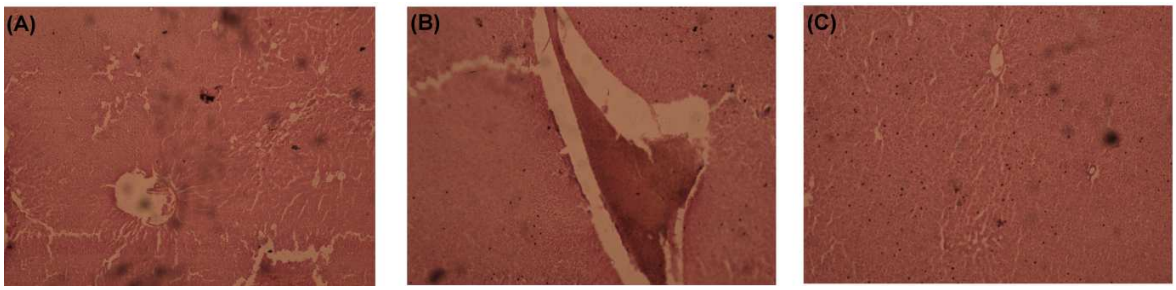

Figure 5.10. Microphotograph of the section of hematoxylin and eosin stained rat liver. Group: (A) Control (B) CCl_4-treated (C) **BTA-29**. Magnification: 10x.

5.1.4. *In-silico* molecular property analysis and ADMET prediction studies

In order to meet the criteria of synthesized compounds as possible drug candidates, *in-silico* molecular properties were calculated using Molinspiration online property calculation toolkit and are presented in **Table 5.6.** All the structures showed suitable MW values (MW < 500) necessary for a successful penetration to CNS with the exception of compounds **BTA-26** and **BTA-25**. All the compounds obeyed Lipinski's rule for

lipophilicity (expressed as MiLogP) except for compounds **BTA-21**, **BTA-23** and **BTA-25**; which violated the rule. The number of hydrogen bond acceptors (HBA) and donors (HBD) for all the compounds were in accordance with the Lipinski's rule of five with the exception of compounds **BTA-7**, **BTA-14**, **BTA-20** and **BTA-30** in which HBA exceeded the defined limit. Further, the topological polar surface area (TPSA) for all the compounds was observed to fall within the range except for compound **BTA-30**. Thus, apart from the compounds **BTA-7**, **BTA-26**, **BTA-14**, **BTA-20**, **BTA-21**, **BTA-23**, **BTA-24** and **BTA-30**; the predicted values for all other compounds fall into the appropriate range indicating good bioavailability of the ligand molecules. Thus it was predicted that most of the compounds are likely to be orally active.

Table 5.6. *In-silico* drug-likeness[a] prediction studies for **BTA-1** to **BTA-30**

Code	MW	MiLogP	HBA	HBD	$n_{violations}$	TPSA	Volume
Rule	<500	≤5	≤10	≤5	≤1	<160 $Å^2$	
BTA-1	307.33	2.06	8	2	0	112.20	254.90
BTA-2	369.41	3.27	8	2	0	112.20	309.75
BTA-3	448.30	4.08	8	2	0	112.20	327.63
BTA-4	403.85	3.95	8	2	0	112.20	323.28
BTA-5	387.40	3.44	8	2	0	112.20	314.68
BTA-6	385.40	2.80	9	3	0	132.43	317.76
BTA-7	414.40	3.23	11	2	1	158.03	333.08
BTA-8	355.38	3.36	8	2	0	112.20	293.18
BTA-9	371.38	3.30	9	3	0	132.43	301.20
BTA-10	434.27	4.17	8	2	0	112.20	311.07
BTA-11	398.45	3.46	9	2	0	115.44	339.09
BTA-12	371.38	2.88	9	3	0	132.43	301.20

BTA-13	385.40	3.42	9	2	0	121.44	318.73
BTA-14	400.38	3.32	11	2	1	158.03	316.52
BTA-15	424.27	4.62	8	2	0	112.20	320.25
BTA-16	424.27	4.64	8	2	0	112.20	320.25
BTA-17	424.27	4.62	8	2	0	112.20	320.25
BTA-18	415.43	3.40	10	2	0	130.67	344.27
BTA-19	415.43	3.40	10	2	0	130.67	344.27
BTA-20	445.46	2.99	11	2	1	139.91	369.82
BTA-21	495.95	5.69	9	2	1	121.44	403.92
BTA-22	431.48	4.49	8	2	0	112.20	364.59
BTA-23	465.92	5.17	8	2	1	112.20	378.13
BTA-24	447.48	4.01	9	3	0	132.43	372.61
BTA-25	500.37	5.85	8	2	2	112.20	391.66
BTA-26	527.20	4.45	8	2	1	112.20	345.76
BTA-27	347.40	3.22	8	2	0	112.20	294.94
BTA-28	396.39	2.60	10	3	0	145.07	313.73
BTA-29	430.83	3.25	10	3	0	145.07	327.26
BTA-30	441.38	2.43	13	3	1	190.89	337.06

[a]MW = Molecular weight, MiLogP = octanol-water partition coefficient, HBA = Number of hydrogen bond acceptor, HBD = Number of hydrogen bond donor, $n_{violations}$ = violations from Lipinski's rule, TPSA = Topological Polar Surface Area

Further, the results of ADMET (Absorption, Distribution, Metabolism, Excretion and Toxicity) properties calculated by PreADMET online server are listed in **Table 5.7.** and **Table 5.8.** respectively.

Human intestinal absorption (HIA) property is the determinant for those drugs that purport oral administration. All the compounds expressed greater than 70% HIA values

indicating good permeation across the membrane except compounds **BTA-7**, **BTA-14** and **BTA-30** which exhibited moderate permeation.

The *in-vitro* Caco-2 cell permeability is an important parameter to assess intestinal absorption of the drug since Caco-2 cells are derived from human colon adenocarcinoma, possessing transports *via* the intestinal epithelium. The results indicated that all compounds exhibited low permeation with the exception of compounds **BTA-3**, **BTA-26** and **BTA-10** which exhibited moderate permeation.

The *in-vitro* MDCK cell permeability test utilizes canine kidney cells for the analysis of permeability. All the compounds **BTA-1** to **BTA-30** showed permeation less than 25 nm/s indicating low permeability.

The skin permeability is an important factor for the delivery of drug *via* transdermal administration. All the compounds **BTA-1** to **BTA-30** exhibited negative permeability values, indicating that transdermal mode of administration is not the suitable means to administer these drugs.

The percent of drug bound with plasma proteins was estimated and almost all the compounds (except **BTA-1**) was predicted to possess > 90% plasma protein binding, indicating decreased excretion and increased half-life.

Table 5.7. *In-silico* ADME prediction data[a] of compounds **BTA-1** to **BTA-30**

Code	**Absorption**				**Distribution**	
	HIA (%)	***In-vitro* CP (nm/s)**	***In-vitro* MDCK (nm/s)**	***In-vitro* SP (log K_p, cm/h)**	***In-vitro* PPB (%)**	***In-vivo* BBB (C_{brain}/ C_{blood})**
Rule	0-20 (poor) 20-70 (moderate) 70-100 (well)	<4 (low) 4-70 (moderate) >70 (high)	<25 (low) 25-500 (moderate) >500 (high)		>90 (strongly bound) <90 (weakly bound)	>0.1 (CNS active) < 0.1 (CNS inactive)
BTA-1	77.69	0.39	4.14	-4.37	67.96	0.029
BTA-2	92.37	0.59	1.23	-3.58	100.00	0.033

BTA-3	96.35	12.97	0.03	-3.45	100.00	0.027
BTA-4	95.44	0.69	0.49	-3.52	100.00	0.027
BTA-5	92.44	0.59	0.62	-3.76	100.00	0.034
BTA-6	83.37	0.38	1.31	-4.09	100.00	0.021
BTA-7	65.78	0.36	0.98	-3.65	100.00	0.063
BTA-8	91.44	0.51	2.49	-3.66	100.00	0.029
BTA-9	81.47	0.38	3.41	-4.09	100.00	0.022
BTA-10	96.17	12.87	0.03	-3.52	100.00	0.025
BTA-11	93.19	1.83	0.83	-3.36	100.00	0.042
BTA-12	81.47	0.38	2.09	-4.12	100.00	0.019
BTA-13	89.59	0.75	1.79	-3.59	100.00	0.050
BTA-14	62.30	0.37	1.50	-3.70	100.00	0.062
BTA-15	96.42	1.80	0.25	-3.38	100.00	0.026
BTA-16	96.42	1.61	1.14	-3.39	100.00	0.028
BTA-17	96.42	2.12	2.19	-3.37	100.00	0.034
BTA-18	87.38	1.33	0.81	-3.54	100.00	0.065
BTA-19	87.38	1.33	0.45	-3.53	100.00	0.059
BTA-20	84.83	2.55	0.17	-3.55	100.00	0.063
BTA-21	96.85	1.24	0.94	-2.93	100.00	0.023
BTA-22	96.44	1.55	0.42	-2.89	100.00	0.049
BTA-23	96.43	0.82	0.63	-2.87	97.32	0.044
BTA-24	93.01	0.48	0.14	-3.26	100.00	0.028
BTA-25	96.06	1.02	0.96	-2.77	94.00	0.048
BTA-26	96.20	19.40	0.05	-3.23	97.35	0.024

BTA-27	84.54	0.43	6.54	-4.11	98.45	0.036
BTA-28	84.86	0.38	1.09	-4.64	100.00	0.049
BTA-29	90.96	1.62	0.13	-4.64	100.00	0.048
BTA-30	47.03	0.36	1.66	-4.53	100.00	0.046

[a]HIA – Human Intestinal Absorption, CP – Caco2 cell permeability, MDCK – MDCK cell permeability, SP – skin permeability, PPB – Plasma protein binding, BBB – Blood brain barrier.

The blood brain barrier (BBB), an important factor which connects the central nervous system (CNS) and peripheral tissues, is responsible for limiting and regulating the exchange of substances between the CNS and blood. All the compounds analyzed showed BBB penetration values less than 0.1 indicating that they are inactive in the CNS. Hence predicts that they are devoid of CNS side effects.

The Ames test assesses mutagenicity of the compounds. All the compounds were predicted as mutagen. Besides, carcinogenicity test was performed to identify the tumerogenic potential of compounds in animals (mouse and rat). When analyzing carcinogenicity in mice, all the compounds were predicted as negative except **BTA-9** and **BTA-14**. By analyzing rat carcinogenicity, compounds **BTA-3**, **BTA-26** and **BTA-10** were predicted positive while rest of the compounds presented negative predictions. Human ether-a-go-go-related gene (hERG) encodes potassium channels, which are responsible for normal repolarization of cardiac action potentials. Blockage or any other impairment of these channels in the heart can lead to fatal cardiac problems. Hence, drug-induced blockage of potassium channels has been a major concern. Compounds **BTA-1**, **BTA-8**, **BTA-9**, **BTA-14** and **BTA-27** presented low risk; **BTA-12** presented medium risk; compounds **BTA-3**, **BTA-4**, **BTA-5**, **BTA-6**, **BTA-26**, **BTA-10**, **BTA-11**, **BTA-13**, **BTA-15 to BTA-21**, **BTA-25** and **BTA-29** presented high risk; while compounds **BTA-2**, **BTA-7**, **BTA-22**, **BTA-23**, **BTA-24**, **BTA-28** and **BTA-30** presented ambiguous results against hERG inhibition.

Table 5.8. *In-silico* toxicity prediction data of compounds **BTA-1** to **BTA-30**

Code	Ames test	Carcinogenicity (Mouse)	Carcinogenicity (Rat)	hERG inhibition
BTA-1	Mutagen	Negative	Negative	Low risk
BTA-2	Mutagen	Negative	Negative	Ambiguous
BTA-3	Mutagen	Negative	Positive	High risk
BTA-4	Mutagen	Negative	Negative	High risk
BTA-5	Mutagen	Negative	Negative	High risk
BTA-6	Mutagen	Negative	Negative	High risk
BTA-7	Mutagen	Negative	Negative	Ambiguous
BTA-8	Mutagen	Negative	Negative	Low risk
BTA-9	Mutagen	Positive	Negative	Low risk
BTA-10	Mutagen	Negative	Positive	High risk
BTA-11	Mutagen	Negative	Negative	High risk
BTA-12	Mutagen	Negative	Negative	Medium risk
BTA-13	Mutagen	Negative	Negative	High risk
BTA-14	Mutagen	Positive	Negative	Low risk
BTA-15	Mutagen	Negative	Negative	High risk
BTA-16	Mutagen	Negative	Negative	High risk
BTA-17	Mutagen	Negative	Negative	High risk
BTA-18	Mutagen	Negative	Negative	High risk
BTA-19	Mutagen	Negative	Negative	High risk
BTA-20	Mutagen	Negative	Negative	High risk
BTA-21	Mutagen	Negative	Negative	High risk

BTA-22	Mutagen	Negative	Negative	Ambiguous
BTA-23	Mutagen	Negative	Negative	Ambiguous
BTA-24	Mutagen	Negative	Negative	Ambiguous
BTA-25	Mutagen	Negative	Negative	High risk
BTA-26	Mutagen	Negative	Positive	High risk
BTA-27	Mutagen	Negative	Negative	Low risk
BTA-28	Mutagen	Negative	Negative	Ambiguous
BTA-29	Mutagen	Negative	Negative	High risk
BTA-30	Mutagen	Negative	Negative	Ambiguous

To sum up, despite other compounds exhibiting good brain penetration profiles, it can be concluded that compound **BTA-29** presents the best drug-like characteristics and however, ADMET property analysis indicated the high risk of **BTA-29** against hERG inhibition among all the compounds of the series.

5.2. 2-AMINO-5-NITROTHIAZOLE DERIVED SEMICARBAZONES [NTA-1 to NTA-18]

5.2.1. Synthesis

2-Amino-5-nitrothiazole derived semicarbazones (**NTA-1** to **NTA-18**) were obtained by refluxing semicarbazide (**NTS**) with appropriate aldehyde or ketone according to the reaction scheme depicted in **Scheme 4.5.**, by optimizing the various reaction variables, viz. solvents, catalyst, temperature, stirring time, etc. The final compounds were recrystallized using ethanol as a solvent.

All the final products were stable to open air environment. The intermediates (**NTU** and **NTS**) and final products were obtained in good yield (50 to 80%) except compounds **NTA-4** (25.61%), **NTA-6** (38.23%), **NTA-8** (49.56%), **NTA-11** (33.27%), **NTA-14** (48.86%) and **NTA-15** (29.75%).

All the products (**NTA-1** to **NTA-18**) were obtained as solid. Some of the compounds were obtained as amorphous powder (**NTA-4**, **NTA-8**, **NTA-12** and **NTA-15**) while the rest (**NTA-1** to **NTA-3**, **NTA-5** to **NTA-7**, **NTA-9** to **NTA-11**, **NTA-13**, **NTA-14** and **NTA-16** to **NTA-18**) were obtained as crystals. The final compounds were of maroon (**NTA-1**, **NTA-6** and **NTA-7**), brown (**NTA-2** to **NTA-5** and **NTA-8** to **NTA-16**) or dark brown (**NTA-17** and **NTA-18**) colour.

5.2.2. Characterization

5.2.2.1. Physicochemical characterization

5.2.2.1.1. Melting point

Melting points were determined in one end open capillary tubes on Sonar melting point apparatus and were uncorrected. All the synthesized compounds displayed a phase change from solid to liquid state and thus exhibited melting range between 2 to 5 °C indicating the purity of compounds except **NTA-13** which charred at 286 °C. The observed melting point ranges for the synthesized compounds **NTA-1** to **NTA-18** are presented in the **Table 4.6.**

5.2.2.1.2. Solubility

The solubility of all the synthesized compounds was determined in number of solvents at room temperature. All intermediates (**NTU** and **NTS**) and final compounds (**NTA-1** to **NTA-18**) were insoluble in water and chloroform and partially soluble in methanol but

soluble in ethanol (a few required slight warming), DMSO and DMF. The observed solubility data are listed in **Table 4.6.**

5.2.2.1.3. Thin layer chromatography

For each reaction, single distinct spot of product and absence of reactant spot in TLC analysis indicated the completion of reaction and the purity of synthesized compounds. TLC was also performed for the final compounds (**NTA-1** to **NTA-18**) after purification to determine their R_f values. The observed R_f values are presented in the **Table 4.6.** Depending upon the polarity of compounds, the composition of eluents used for TLC analysis were (i) Chloroform: Methanol: Toluene (8:2:1); (B) Chloroform: Methanol: Toluene (8:1:2); (C) Benzene: Acetone (8:2); (D) Benzene: Acetone (9:1).

5.2.2.1.4. Determination of partition coefficient (LogP)

The synthesized compounds were found to exhibit experimental LogP values in the range 1.2 – 3.9 (shake flask method) indicating that they possess adequate lipophilicity necessary for their solubility in the lipid phase. The experimental (determined through shake flask method) and calculated LogP (software calculated) values are listed in **Table 4.6.**

5.2.2.2. Spectral characterization and elemental analysis

5.2.2.2.1. Ultraviolet (UV) spectroscopy

All the compounds showed prominent absorption with respect to the chromophore. The compounds of **NTA** series exhibited absorption bands due to C=N and C=O chromophores at λ_{max} 250-300 nm and 290-330 nm respectively owing to $n \rightarrow \pi^*$ transition.

5.2.2.2.2. Infrared (IR) spectroscopy

The semicarbazones showed characteristic absorption in the functional group region at 3150-3500 cm^{-1} and 1600-1700 cm^{-1} which confirmed the presence of NH (str) and C=O (str) of the amide respectively. Further, the formation of semicarbazones was confirmed by the presence of stretching at 1520-1640 cm^{-1} due to imine (C=N) group. The characteristic absorption in the range 1300-1460 cm^{-1} and 1500-1560 cm^{-1} confirmed the presence of $-NO_2$ (str) while that at 1116.82 cm^{-1} (**NTA-12**) confirmed the presence of $O-CH_3$ (str). The characteristic absorption in the range 3200-3600 cm^{-1} (**NTA-4**, **NTA-8** and **NTA-15**) confirmed the presence of OH (str) respectively. The presence of C=O (str)

group of indole ring of isatin was confirmed by the characteristic absorption in the range 1680-1700 cm^{-1} (**NTA-17** and **NTA-18**). The presence of characteristic absorptions around 2890-3100 cm^{-1} confirmed the presence of aryl C-H (str) while the presence of C-N (str) was confirmed by the strong peaks in the range 1100-1300 cm^{-1}. The presence of halogens was confirmed by the peaks in the range 450-850 cm^{-1} for C-Br (**NTA-1**, **NTA-6**, **NTA-7** and **NTA-18**) and C-Cl (**NTA-2**, **NTA-9**, **NTA-10**, **NTA-11**, **NTA-14** and **NTA-16**) and 950-1100 cm^{-1} for C-F (**NTA-3**) groups.

5.2.2.2.3. Nuclear magnetic resonance (NMR) spectroscopy

^1H NMR spectra of all the 2-amino-5-nitrothiazole derived semicarbazones showed a characteristic singlet peak at δ 8.98-9.90 ppm and δ 9.75-10.86 ppm indicating –NH– and –CONH– protons, respectively. The appearance of multiplets at δ 6.85-8.28 ppm confirmed the presence of aromatic protons. The singlet at δ 8.09-8.36 ppm (**NTA-8** to **NTA-12**), δ 1.03-2.22 ppm (**NTA-1** to **NTA-5**) and δ 8.13-8.89 ppm (**NTA-1** to **NTA-18**) indicated the C-H, C-CH_3 and thiazole protons respectively. In ^1H NMR spectra of semicarbazones having indolyl group, a singlet was observed at δ 9.77-8.36 ppm (**NTA-17** and **NTA-18**) due to >NH of indole ring. The singlet at δ 3.36 ppm (**NTA-12**), δ 4.92-4.99 ppm (**NTA-4**, **NTA-8** and **NTA-15**) and δ 3.56 ppm (**NTA-6**) indicated the presence of OCH_3, OH and CH_2 protons respectively. The disappearance of signals of amino NH and carbimino NH indicated the presence of exchangeable protons (**NTA-16**; **Figure 4.44.**)

In ^{13}C NMR spectra the appearance of signals in the range of δ 154.45-159.93 ppm confirmed the presence of carbonyl group of semicarbazone linker. Moreover, ^{13}C NMR spectra showed signals in the range of δ 144.66-171.72 ppm (**NTA-1** to **NTA-18**) which was due to C=N carbon. The signals at δ 111.73-148.53 ppm corresponded to the presence of thiazole carbons. The presence of OCH_3 groups was also confirmed by the signal at δ 59.93 ppm (**NTA-12**). Clustered signals in the range of δ 107.63-167.88 ppm corresponded to the presence of aryl carbons. Characteristic signals at δ 19.03-19.31 ppm (**NTA-1** to **NTA-5**), δ 74.77 (**NTA-6**) and δ 168.96-171.74 ppm (**NTA-17** and **NTA-18**) corresponded to CH_3, CH_2 and oxindole C=O respectively.

5.2.2.2.4. Mass spectrometry

Compounds **NTA-5**, **NTA-10** and **NTA-17** were subjected to mass analysis. **NTA-5** (Mol. wt. = 350.31) showed an $[M+1]^+$ peak at 351.39 (**Figure 4.37.)**, **NTA-10** (Mol. wt.

= 360.18) showed an $[M+1]^+$ peak at 361.14 (**Figure 4.41.)** and **NTA-17** (Mol. wt. = 332.29) showed an $[M+1]^+$ peak at 333.10 (**Figure 4.49.)** respectively, thereby confirming the structure of the compounds.

5.2.2.2.5. Elemental analysis

All the compounds **NTA-1** to **NTA-18** were subjected to elemental analysis and the observed values were within ± 0.4% of the calculated values.

5.2.2.2.6. Powder X-ray diffraction analysis

Compound **NTA-5** was subjected to the powder X-ray diffraction analysis to confirm the crystallinity of the compound. The diffraction pattern of **NTA-5** comprised of sharp peaks (**Figure 4.37.**) indicating the crystalline nature of the compound.

5.2.3. Biological evaluation

5.2.3.1. MAO enzyme inhibition studies

5.2.3.1.1. *In-vitro* MAO inhibition assay

To achieve a better understanding of the structural requirements for both inhibition and selectivity towards the two MAO isoforms, all the synthesized semicarbazones **NTA-1** to **NTA-18** were assessed for their ability to inhibit both the MAO isozymes. **Table 5.9.** lists the *in-vitro* rat brain MAO-A/B inhibitory activity data of final compounds **NTA-1** to **NTA-18** as well as the reference compounds clorgyline (for MAO-A) and selegiline (for MAO-B).

Table 5.9. *In-vitro* and computational MAO inhibition data for **NTA-1** to **NTA-18**

Code	MAO-A			MAO-B			SI[a]
	In-vitro	Computational		*In-vitro*	Computational		
	IC_{50} (µM) ± SEM	ΔG*	K_i (µM)	IC_{50} (µM) ± SEM	ΔG*	K_i (µM)	
NTA-1	70.19 ± 0.045	-5.93	44.63	0.212 ± 0.004	-6.63	13.84	331.08
NTA-2	4761 ± 10.83	-5.64	73.85	0.601 ± 0.015	-6.43	19.46	7921.79
NTA-3	46066 ± 16.72	-5.29	131.54	19.89 ± 0.032	-5.45	100.78	2316.04
NTA-4	5899 ± 9.84	-5.49	94.27	14.75 ± 0.018	-5.67	70.06	399.93
NTA-5	2743 ± 3.65	-6.28	25.09	23.88 ± 0.022	-5.55	84.89	114.86

NTA-6	314 ± 1.89	-5.85	51.78	0.313 ± 0.007	-6.56	15.49	1003.19
NTA-7	5153 ± 8.82	-5.51	90.88	5.451 ± 0.009	-7.8	1.92	945.33
NTA-8	11342 ± 11.65	-5.28	134.91	241.5 ± 2.31	-6.75	11.19	46.96
NTA-9	3369 ± 6.43	-5.74	62.48	8.512 ± 0.132	-7.32	4.3	395.79
NTA-10	10465 ± 13.92	-5.49	94.68	3.487 ± 0.098	-6.53	16.22	3001.15
NTA-11	13915 ± 19.68	-5.24	144.64	16.94 ± 0.37	-5.31	127.39	821.43
NTA-12	55048 ± 24.77	-4.99	220.79	11.13 ± 0.19	-5.85	51.52	4945.91
NTA-13	89.29 ± 1.26	-6.5	17.11	28.29 ± 0.45	-5.41	109.05	3.15
NTA-14	4872 ± 5.81	-5.63	74.36	28.52 ± 0.079	-5.5	93.15	170.83
NTA-15	34305 ± 17.38	-5.25	141.62	157.9 ± 3.71	-5.06	194.35	217.26
NTA-16	50716 ± 21.75	-5.06	195.81	1.476 ± 0.063	-6.56	15.63	34360.43
NTA-17	2250 ± 12.81	-5.89	47.83	4.507 ± 0.086	-5.95	43.86	499.22
NTA-18	57.21 ± 1.36	-5.91	46.69	0.734 ± 0.006	-6.26	25.6	77.94
CLG	0.0044 ± 0.462	-	-	-	-	-	-
SEL	67.25 ± 1.02	-	-	0.020 ± 0.0008	-	-	-
HRM	3.00	-5.3	130.82	7000	-	-	-
SAF	-	-	-	0.100	-5.93	45.23	-

*ΔG is expressed in kcal mol^{-1}; [a]SI – The selectivity index is the selectivity for the MAO-B isoform and is given as the ratio of experimental IC_{50}(MAO-A)/IC_{50}(MAO-B); Reference inhibitors: CLG – Clorgyline, SEL – Selegiline, HRM – Harmine, SAF – Safinamide

NOTE: Each IC_{50} value is the mean ± SEM. It refers to the assay concentration of test compound which leads to 50% inhibition of enzyme activity. Level of statistical significance: $P < 0.05$ versus the corresponding IC_{50} values obtained against MAO-A and MAO-B, as determined by ANOVA/Dunnett's.

The inhibitory activities against MAO-A and MAO-B isozymes were examined by measuring the effects of each derivative on the production of 5-hydroxyindole acetic acid from serotonin (5-HT) for MAO-A and benzaldehdye from benzylamine for MAO-B, using the UV based spectrophotometric MAO enzyme inhibition assay method by using crude rat brain mitochondrial suspension.

The MAO inhibition data are expressed as IC_{50} values. Based on the MAO screening data (**Table 5.9.**), it was observed that most of the synthesized compounds exhibited improved inhibitory potential towards MAO-B than MAO-A with the IC_{50} values in the micromolar to sub-micromolar range. The MAO-B selectivity ratios are presented in **Table 5.9.** The IC_{50} values towards MAO-A range from 57.21 ± 1.36 µM (compound **NTA-18**) to 55048 ± 24.77 µM (compound **NTA-12**) while for MAO-B range from 0.212 ± 0.004 µM (compound **NTA-1**) to 157.9 ± 3.71 µM (compound **NTA-15**).

Among the synthesized compounds, 1-(5-bromo-2-oxoindolin-3-ylidene)-4-(5-nitrothiazol-2-yl)semicarbazide (**NTA-18**) was found to be most active MAO-A inhibitor with IC_{50} value of 57.21 ± 1.36 µM, whereas the most active MAO-B inhibitor, 4-(5-nitrothiazol-2-yl)-1-(1-phenylethylidene)semicarbazide (**NTA-1**) was found to exhibit an IC_{50} value of 0.212 ± 0.004 µM with the selectivity index of 331.08 against MAO-B in the study. Interestingly, **NTA-16** showed excellent selectivity (SI = 34360.43) towards MAO-B with an IC_{50} value of 1.476 ± 0.063 µM.

With a view to illuminate the SARs, focused structural variations were endeavored at the carbimino terminal of the semicarbazone template resulting in the alterations in the activity. Indeed, increase in the lipophilicity caused by the incorporation of monoaryl (**NTA-1** to **NTA-12**) or diaryl rings (**NTA-13** to **NTA-16**) or an isatin residue (**NTA-17** and **NTA-18**) at the carbimino terminal resulted in increased inhibition and selectivity towards MAO-B compared to MAO-A.

Very poor MAO-A inhibitory activity was obtained for **NTA-3**, **NTA-8**, **NTA-10**, **NTA-11**, **NTA-12**, **NTA-15** and **NTA-16**. **NTA-12** was observed to be the least active MAO-A inhibitor among all the synthesized semicarbazones. Hence, we have focused on the MAO-B inhibition activity exhibited by the compounds of this series for structure-activity relationship studies.

SAR for MAO-B inhibition

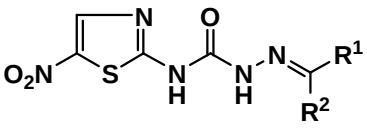

NTA-1 to NTA-16

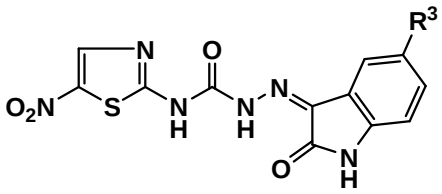

NTA-17 and NTA-18

- Introduction of bromo group on the phenyl ring at the carbimino terminal increased the activity towards MAO-B (**NTA-1**, **NTA-6**, **NTA-7** and **NTA-18**).
- Reduction in the MAO-B inhibition activity to an extent was observed with chloro substitution on the phenyl ring at the carbimino terminal (**NTA-2**, **NTA-9**, **NTA-10**, **NTA-11**, **NTA-14** and **NTA-16**).
- Monochloro substituted derivative (**NTA-2**) expressed better MAO-B activity than the dichloro substituted derivatives (**NTA-9**, **NTA-10** and **NTA-11**).
- Substitution with F group (**NTA-3**) also lead to less active compound.
- Introduction of bulky groups like $–NO_2$ (**NTA-5**) and dimethoxy (**NTA-12**) on the phenyl ring at the carbimino terminal also resulted in the decrease in the activity towards MAO-B.
- Remarkable reduction in the MAO-B inhibition activity was observed on substitution of hydroxyl group (**NTA-4**, **NTA-8** and **NTA-15**) at para position of the phenyl ring on the carbimino terminal.
- Among the diaryl analogues, the dichloro substituted derivative was found to be most active (**NTA-16**) while the –OH substituted derivative was found to be least active (**NTA-15**) against MAO-B.
- Among the isatin-3-substituted semicarbazones, 5-Br substituted derivative (**NTA-18**) was found to be more potent for MAO-B than the unsubstituted one (**NTA-17**).

These results evidenced the influence of the steric groups with electronic substituents at the carbimino terminal of semicarbazone scaffold on the MAO-B inhibitory profile.

5.2.3.1.2. Kinetic studies of lead MAO inhibitors

Sets of Lineweaver-Burk plots were constructed to further examine the modes of inhibition of MAO-A enzyme by **NTA-18** and MAO-B by **NTA-1**, the selected representative lead MAO-A and MAO-B inhibitor respectively (**Figure 5.11.**). Assessment of Lineweaver-Burk plots indicated that the plot of **NTA-18** was linear and intersected at the X-axis (K_m remains unaffected while V_{max} decreases) while that for **NTA-1** was linear and intersected at the Y-axis (K_m increases while V_{max} remains unaffected). Thus, the pattern indicated that **NTA-18** inhibited MAO-A non-

competitively while **NTA-1** inhibited MAO-B competitively, and these results further proved that they were reversible MAO-A and MAO-B inhibitors.

5.2.3.1.2.1. Determination of K_i for lead MAO inhibitors

The dissociation constant (K_i) was determined for the lead MAO-A and MAO-B inhibitors for each type of inhibition using GraphPad Prism software, revealing the strength of interactions between the enzyme and the inhibitor. K_i value for non-competitive MAO-A inhibitor **NTA-18** was estimated to be 17.30 ± 1.79 µM while the competitive MAO-B inhibitor **NTA-1** exhibited K_i value of 11.69 ± 0.58 µM against MAO-B.

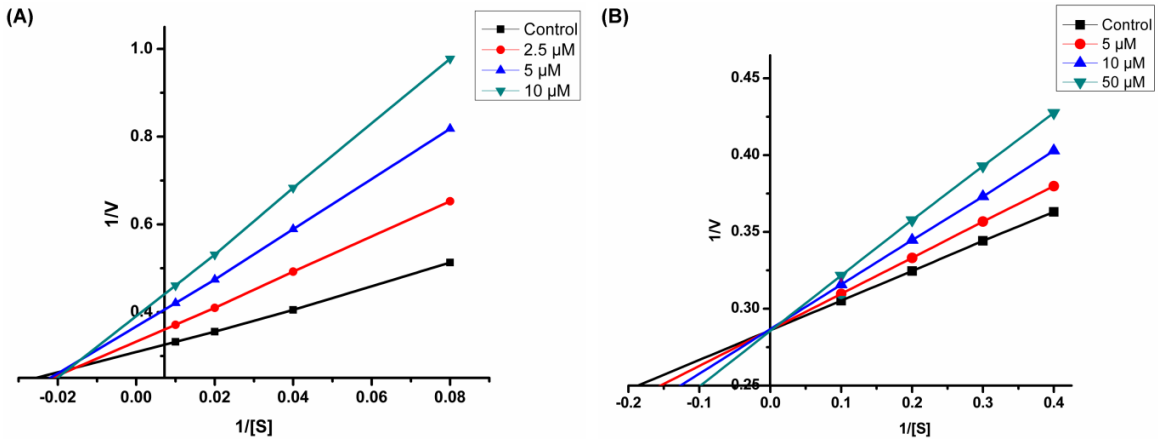

Figure 5.11. Kinetics of rat brain MAO-A inhibition by **NTA-18** and MAO-B inhibition by **NTA-1**. (A) Lineweaver-Burk plot of the rat brain MAO-A catalyzed oxidation of serotonin in the absence (control) and presence of various concentrations of **NTA-18** (2.5 µM, 5 µM, 10 µM). (B) Lineweave-Burk plot of the rat brain MAO-B catalyzed oxidation of benzylamine in the absence (control) and presence of various concentrations of **NTA-1** (5 µM, 10 µM, 50 µM). The rates (V) are expressed as nmol product formed/min/mg protein.

5.2.3.1.3. Reversibility studies for lead MAO inhibitors

Time-dependent inhibition studies were performed on the most active MAO-A and MAO-B inhibitors, **NTA-18** and **NTA-1** respectively to inspect whether the observed enzyme inhibition is reversible or irreversible. Time-dependent inhibition was determined using the slightly modified method described by Legoabe *et al*. No time-dependent reduction in the rates of MAO-A catalyzed oxidation of serotonin and MAO-B catalyzed oxidation of benzylamine respectively was observed when **NTA-18** and **NTA-1** were

preincubated with the MAO-A and MAO-B enzymes respectively for various periods of time (0, 15, 30, and 60 min). Thus, the above findings speculated that the inhibition of both MAO-A and MAO-B was reversible, at least for the above time period (60 min). Fascinatingly, an enhancement of catalytic rates of MAO-A and MAO-B was noticed with increased preincubation time of **NTA-18** and **NTA-1** with the respective enzymes (**Figure 5.12.**).

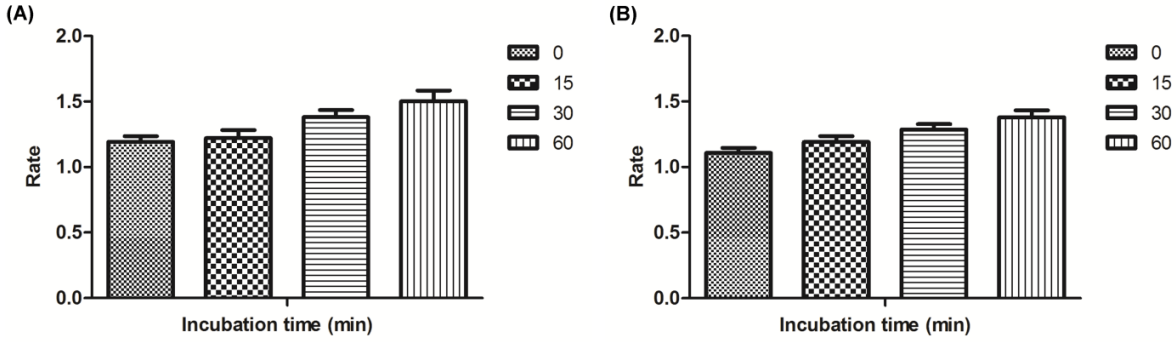

Figure 5.12. Time-dependant inhibition of (A) MAO-A catalyzed oxidation of serotonin by **NTA-18** (B) MAO-B catalyzed oxidation of benzylamine by **NTA-1**. Rate data are expressed as nmol product formed/min/mg protein.

5.2.3.1.2. Molecular docking studies of MAO inhibitors

In order to explore the nature of ligand-receptor interactions, virtual molecular docking experiments were performed within the active site of MAO-A and MAO-B isoforms using an automated docking program AutoDock 4.2. The co-crystallized structures of hMAO-A (PDB Code: 2Z5X) and hMAO-B (PDB Code: 2V5Z) were used to dock the synthesized compounds. The conformers acquiring the top score among the largest cluster were considered for further structural and binding interaction studies.

A satisfactory correlation was observed between the experimental and computational MAO-B inhibition data. However, MAO-A inhibition results were found to vary dramatically and exhibited poor correlation. The outcomes of the docking studies were theoretically stated in terms of inhibition constants (K_i values) and free binding energies (ΔG) for each of the virtual ligand-receptor complex and the results are presented in **Table 5.9.**

5.2.3.1.2.1. Pose analysis of MAO-A inhibitors

Assessment of the virtual ligand-receptor complexes of all compounds within the catalytic site of MAO-A resulted in the below mentioned interpretations: On the whole, all the test compounds occupied the active site of MAO-A and were framed within the binding pocket constituted by the residues Ile180, Asn181, Tyr197, Phe208, Val210, Gln215, Cys323, Ile 325, Ile335, Phe352, Tyr407, Tyr444 and FAD which was analogous to the reference MAO-A inhibitor, harmine (**Figure 5.13. (A)** and **(B)**). Compounds **NTA-1**, **NTA-2**, **NTA-3**, **NTA-5**, **NTA-6**, **NTA-7**, **NTA-9**, **NTA-10** and **NTA-12** (**Figure 5.13. (A)**); and **NTA-4**, **NTA-8**, **NTA-11**, **NTA-13**, **NTA-14**, **NTA-15**, **NTA-16**, **NTA-17** and **NTA-18** (**Figure 5.13. (B)**) shared a common binding orientation within the active site of MAO-A.

In all the compounds of **Figure 5.13. (A)**, the 5-nitrothiazole nucleus occupied the centre of the cavity towards FAD while the carbimino terminal of the semicarbazino linker is situated towards the opening of the cavity. Whereas in all the compounds of **Figure 5.13. (B)**, the case was exactly the reverse i.e. the carbimino terminal is located towards the FAD and the 5-nitrothiazole moiety extends towards the opening of the cavity space. Residues Tyr407, Tyr444 and FAD formed the bottom of the aromatic cage which accounted to the binding orientation of the compounds and consequently their activity, binding affinity, selectivity and stability.

All compounds showed one or more H-bond interactions excluding compounds **NTA-3**, **NTA-12**, **NTA-14**, **NTA-15** and **NTA-16**. H-bond interactions were observed with residue Tyr197 for compounds **NTA-1**, **NTA-4**, **NTA-6**, **NTA-7**, **NTA-8**, **NTA-9**, **NTA-10** and **NTA-12**; likewise with Val210 for compounds **NTA-2**, **NTA-5** and **NTA-8**; with Asn181 for compound **NTA-4**, **NTA-8** and **NTA-11**; with Thr336 for compound **NTA-5**; with Tyr407 for compound **NTA-7**; with Gln215 for compounds **NTA-6**, **NTA-8** and **NTA-11**; with Cys323 for compounds **NTA-11** and **NTA-18**; with Tyr444 for compound **NTA-13**; and with FAD for compounds **NTA-2**, **NTA-5**, **NTA-17** and **NTA-18**. Additionally, all the compounds showed $\pi - \pi$ interactions apart from **NTA-8** and **NTA-11**. $\pi - \pi$ interaction with residue Tyr407 was observed for compounds **NTA-1**, **NTA-3**, **NTA-4**, **NTA-6**, **NTA-7**, **NTA-9**, **NTA-10**, **NTA-15**, **NTA-17** and **NTA-18**; likewise with Tyr444 for compounds **NTA-1**, **NTA-3**, **NTA-4**, **NTA-6**, **NTA-7**, **NTA-9**, **NTA-10**, **NTA-12** and **NTA-15**; with Phe208 for compounds **NTA-5**, **NTA-7** and **NTA-12**; with

Phe352 for compounds **NTA-13** and **NTA-16**; and with FAD for compounds **NTA-14** and **NTA-16**. Furthermore, compound **NTA-1** was stabilized by π – σ interaction with FAD; likewise compounds **NTA-2** and **NTA-18** with Phe352. Thus, in the active compounds *viz.* **NTA-1**, **NTA-13** and **NTA-18** (IC_{50} < 100 µM), preferably H-bond and π – π interactions were found to be accountable for mediating inhibition against MAO-A.

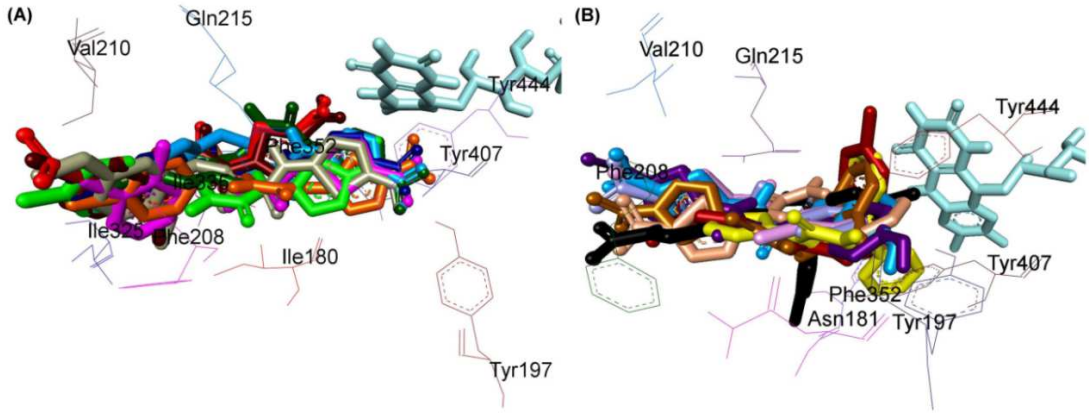

Figure 5.13. Structural screenshot of superimposed MAO-A inhibitors docked into the binding pocket of MAO-A. FAD is displayed in cyanin. Selected amino acids are depicted in black. (A) Shared binding orientation of **NTA-1**, **NTA-2**, **NTA-3**, **NTA-5**, **NTA-6**, **NTA-7**, **NTA-9**, **NTA-10** and **NTA-12** are displayed in dark blue, dark brown, fluorescent green, red, dark orange, sky blue, dark pink, dark green and gray color respectively. (B) Shared binding orientation of **NTA-4**, **NTA-8**, **NTA-11**, **NTA-13**, **NTA-14**, **NTA-15**, **NTA-16**, **NTA-17** and **NTA-18** are displayed in dark violet, sky blue, light brown, yellow, maroon, skin, black, light violet and light pink color respectively.

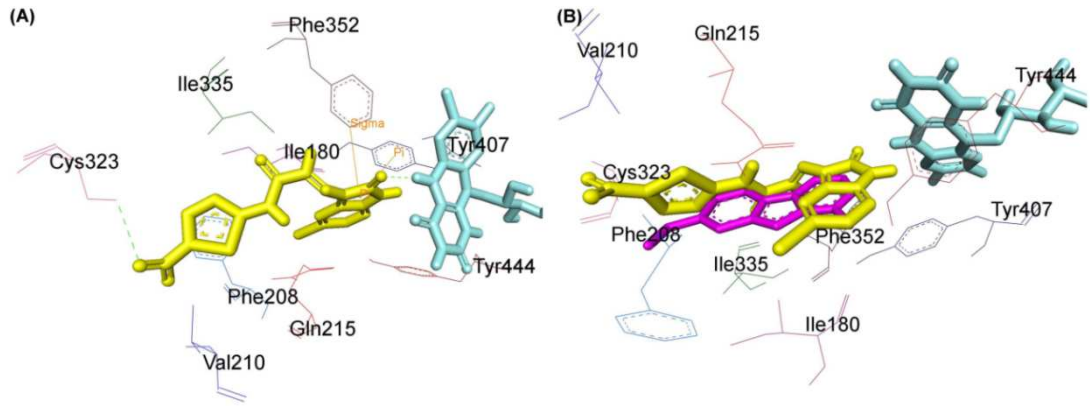

Figure 5.14. Structural screenshot of superimposed MAO-A inhibitors docked into the binding pocket of MAO-A. FAD is displayed in cyanin. Selected amino acids are depicted in black. (A) Binding orientation of **NTA-18** (yellow) within the MAO-A binding pocket showing π – π (orange colored lines) and H-bond (green dashes)

interactions. (B) Superimposed binding orientation of **NTA-18** (yellow) within the MAO-A binding pocket originally docked with harmine (dark pink).

5.2.3.1.2.2. Binding mode of lead MAO-A inhibitor NTA-18

Assessment of one of the best-ranked docking solutions of lead MAO-A inhibitor **NTA-18** (**Figure 5.14. (A)**) (ΔG = -5.91 kcal mol^{-1}; K_i = 46.69 µM) revealed that semicarbazone linker occupied the centre of the cavity with the 5-bromoisatin moiety facing towards FAD while the 5-nitrothiazole moiety was positioned towards the opening of the MAO-A receptor. The 5-membered ring of isatin was involved in $\pi - \pi$ interaction with Tyr407 at an inter-plane distance of approximately 4.64 Å. In addition, the molecule was also stabilized by H-bond interactions between (i) O of NO_2 of 5-nitrothiazole and H of SH of Cys323 and (ii) O of C=O of isatin and H5 of FAD. **Figure 5.14. (B)** illustrated the docked pose of compound **NTA-18** (yellow) within the MAO-A binding pocket superimposed with the docked pose of harmine (dark pink) which indicated the similarity in their binding orientation further supporting our results.

5.2.3.1.2.3. Pose analysis of MAO-B inhibitors

All the inhibitors were located within the catalytic binding pocket of MAO-B. The binding mode of all the test compounds within MAO-B traversed both the binding pockets, entrance cavity lined by the residues Leu171, Phe168, Ile198, Ile199 and Tyr326; and substrate cavity bordered by the residues Tyr60, Cys172, Gln206, Tyr398 and Tyr435 which was almost analogous to the binding sites of safinamide, the reference MAO-B inhibitor (**Figure 5.15. (A)** and **Figure 5.15. (B)**). Compounds **NTA-1**, **NTA-2**, **NTA-3**, **NTA-6**, **NTA-7**, **NTA-10, NTA-13** and **NTA-15** (**Figure 5.15. (A)**); and **NTA-4**, **NTA-5**, **NTA-8**, **NTA-9**, **NTA-11**, **NTA-12**, **NTA-14**, **NTA-16**, **NTA-17** and **NTA-18** (**Figure 5.15. (B)**) shared a common binding orientation within the active site of MAO-B. In all the compounds of **Figure 5.15. (A)**, the 5-nitrothiazole nucleus was located in the substrate cavity while the carbimino side chain extended towards the entrance cavity of MAO-B. Whereas in all the compounds of **Figure 5.15. (B)**, the case was exactly the reverse i.e. the carbimino terminal bearing aromatic/heteroaromatic ring occupied the cavity situated towards the FAD and the 5-nitrothiazole moiety flipped towards the entrance cavity space of MAO-B.

All the compounds showed H-bond interactions except **NTA-9** and **NTA-10**. H-bond interactions with Leu171 was observed for compound **NTA-12**; likewise with Cys172 for compounds **NTA-15**, **NTA-15** and **NTA-17**; with Tyr188 for compound **NTA-8**; with Ile198 for compounds **NTA-1**, **NTA-2**, **NTA-3**, **NTA-5**, **NTA-6**, **NTA-7** and **NTA-17**; with Thr201 for compounds **NTA-8** and **NTA-16**; with Gln206 for compounds **NTA-4**, **NTA-11**, **NTA-16** and **NTA-18**; with residue Tyr326 were observed with compounds **NTA-5** and **NTA-14**; with Tyr398 for compounds **NTA-13** and **NTA-15**; with Tyr435 for compounds **NTA-1**, **NTA-2**, **NTA-3**, **NTA-6** and **NTA-7**; and with FAD for compounds **NTA-4**, **NTA-5**, **NTA-16** and **NTA-18**. Also, all compounds showed $\pi - \pi$ interactions except compound **NTA-3**, **NTA-5**, **NTA-13**, **NTA-14** and **NTA-15**. $\pi - \pi$ interactions were observed with Tyr326 for compounds **NTA-1**, **NTA-2** and **NTA-10**; likewise with Tyr398 for compounds **NTA-1**, **NTA-4**, **NTA-8**, **NTA-9**, **NTA-10**, **NTA-12** and **NTA-16**; with Tyr435 for compounds **NTA-1**, **NTA-2**, **NTA-6**, **NTA-7**, **NTA-8**, **NTA-9**, **NTA-10**, **NTA-11**, **NTA-12** and **NTA-16**. Additionally, $\pi - \sigma$ interaction has been observed with Gln206 for compound **NTA-11**; with Phe208 for compound **NTA-17**; with Tyr435 for compound **NTA-18**; and with FAD for compounds **NTA-4** and **NTA-18**. Thus, in most of the MAO-B active compounds (**NTA-1**, **NTA-2**, **NTA-6** and **NTA-18**), preferably $\pi - \pi$ and H-bond interactions were found to be responsible for mediating inhibition against MAO-B.

5.2.3.1.2.4. Binding mode of lead MAO-B inhibitor NTA-1

Visual inspection of one of the best-ranked docking solution of lead MAO-B inhibitor **NTA-1** revealed that the entire molecule was stabilized within both the cavities with the rigid hydrophobic 5-nitrothiazole moiety caged into the substrate cavity, while the arylidine ring present at the carbimino terminal extended towards the entrance cavity of the MAO-B. The compound was found to be stabilized by H-bond and $\pi - \pi$ interactions. H-bond interactions have been observed between oxygen of carbimino C=O and H of OH of Tyr435; and H of NH in carbimino linker and oxygen of Ile198. In addition, $\pi - \pi$ interactions between the thiazole ring and the phenyl ring of Tyr398 and Tyr435; and phenyl ring at carbimino terminal with phenyl ring of Tyr326 (**Figure 5.16. (A)**). These interactions, overall, resulted in the firmness of the ligand within the MAO-B catalytic site and hence confirmed the stability of the ligand-receptor complex. **Figure 5.16. (B)**

demonstrated the docked pose of **NTA-1** (yellow) within the catalytic site of MAO-B superimposed with the docked pose of safinamide (dark green). **NTA-1** was found to occupy the active site of the MAO-B enzyme but not in exactly similar mode to that of the reference inhibitor, safinamide (dark green)

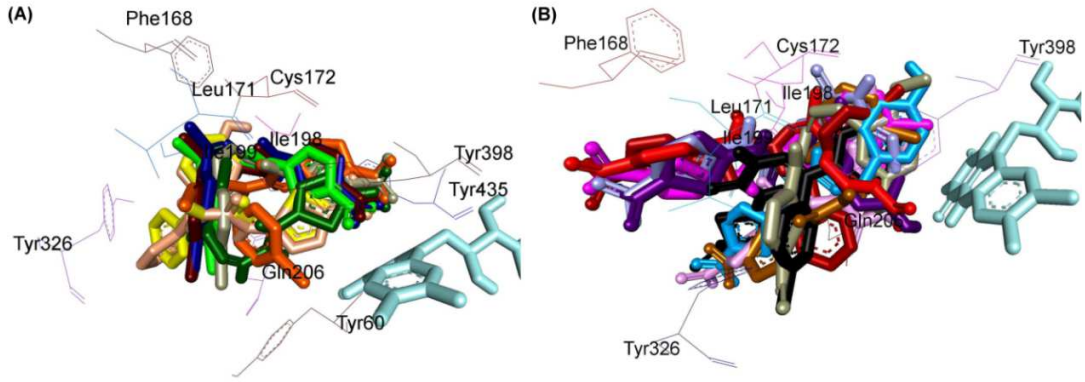

Figure 5.15. Structural screenshot of superimposed MAO-B inhibitors docked into the binding pocket of MAO-B. FAD is displayed in cyanin. Selected amino acids are depicted in black. (A) Shared binding orientation of **NTA-1**, **NTA-2**, **NTA-3**, **NTA-6**, **NTA-7**, **NTA-10,** **NTA-13** and **NTA-15** are displayed in dark blue, dark brown, fluorescent green, dark orange, gray, dark green, yellow and skin color respectively. (B) Shared binding orientation of **NTA-4**, **NTA-5**, **NTA-8**, **NTA-9**, **NTA-11**, **NTA-12**, **NTA-14**, **NTA-16**, **NTA-17** and **NTA-18** are displayed in dark violet, red, sky blue, dark pink, light brown, gray, maroon, black, light violet and light pink color respectively.

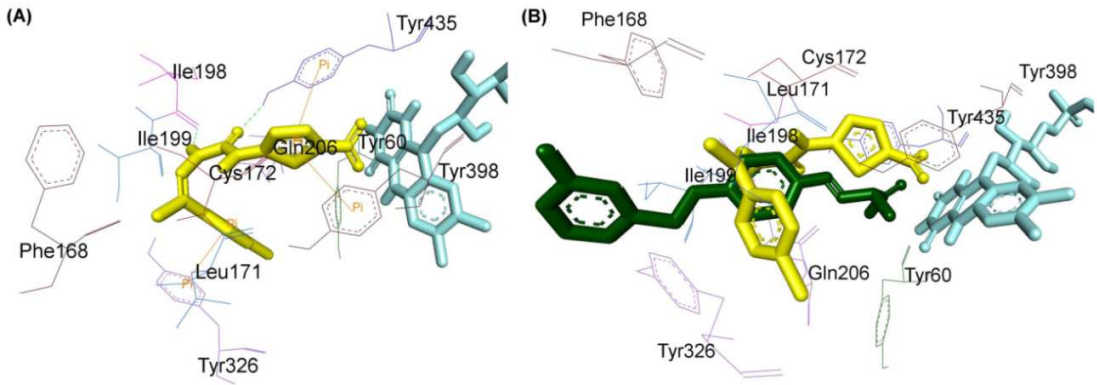

Figure 5.16. Structural screenshot of superimposed MAO-B inhibitors docked into the binding pocket of MAO-B. FAD is displayed in cyanin. Selected amino acids are depicted in black. (A) Binding orientation of **NTA-1** (yellow) within the MAO-B binding pocket showing $\pi - \pi$ (orange colored lines) and H-bond (green dashes) interactions. (B)

Superimposed binding orientation of **NTA-1** (yellow) within the MAO-B binding pocket originally docked with safinamide (dark green).

5.2.3.2. AChE enzyme inhibition studies

5.2.3.2.1. *In-vitro* AChE inhibition assay

All the synthesized compounds were subjected to Ellman's test in order to evaluate their potency to inhibit the rat AChE by the colorimetric method but with minor modifications. Donepezil and tacrine were used as reference standards. The data are displayed in terms of IC_{50} values in **Table 5.10.**

Table 5.10. *In-vitro* and computational AChE inhibition data for **NTA-1 to NTA-18**

Code	AChE		
	In-vitro	**Computational**	
	IC_{50} (µM) ± SEM	**ΔG (kcal mol^{-1})**	**K_i (µM)**
NTA-1	0.340 ± 0.007	-6.29	24.54
NTA-2	356.1 ± 4.73	-5.29	132.58
NTA-3	467.9 ± 4.98	-5.05	197.98
NTA-4	12.69 ± 0.62	-6.16	30.68
NTA-5	45.53 ± 1.36	-6.21	28.08
NTA-6	3.926 ± 0.014	-6.51	16.96
NTA-7	96.37 ± 2.81	-5.6	78.3
NTA-8	584.4 ± 7.92	-5.03	205.05
NTA-9	101.2 ± 1.58	-5.63	74.59
NTA-10	140.7 ± 3.11	-5.46	99.58
NTA-11	10.67 ± 0.56	-6.08	34.85
NTA-12	872.0 ± 4.38	-5.4	109.84
NTA-13	4.864 ± 0.81	-6.68	12.76
NTA-14	11.54 ± 0.35	-6.38	21.08
NTA-15	2.662 ± 0.084	-7.3	4.46
NTA-16	1.450 ± 0.047	-7.05	6.8

NTA-17	54.85 ± 0.92	-5.77	58.85
NTA-18	0.2645 ± 0.009	-6.71	11.97
DPZ	0.021 ± 0.005	-6.01	39.45
TAC	0.225 ± 0.04	-	-

Reference inhibitors: DPZ – Donepezil, TAC – Tacrine

NOTE: Each IC_{50} value is the mean ± SEM. Level of statistical significance: $P < 0.05$ versus the corresponding IC_{50} values obtained against AChE, as determined by ANOVA/Dunnett's.

All the synthesized compounds **NTA-1** to **NTA-18** were found to show activity against AChE displaying inhibition in micromolar to submicromolar range. Among them, **NTA-18**, 1-(5-bromo-2-oxoindolin-3-ylidene)-4-(5-nitrothiazol-2-yl)semicarbazide (IC_{50} = 0.264 ± 0.009 µM) emerged as the most active inhibitor in the study, followed by **NTA-1**, (1-(1-(4-bromophenyl)ethylidene)-4-(5-nitrothiazol-2-yl)semicarbazide, IC_{50} = 0.340 ± 0.007 µM). The activity of **NTA-18** was observed to be almost equivalent to the reference inhibitor tacrine. It was noted that both these compounds possessed bromo substituent at the carbimino terminal of the semicarbazone template.

A thorough examination of the statistics presented in **Table 5.10.** guided us to eventual structure-activity relationships (SAR).

Structure-activity relationship

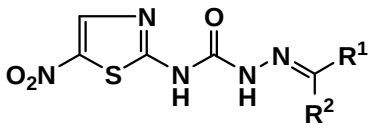

NTA-1 to NTA-16

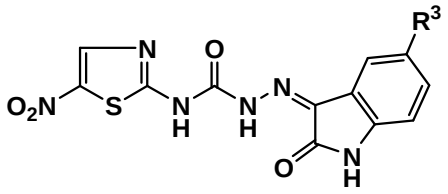

NTA-17 and NTA-18

- In general, improvement in AChE inhibitory activity was observed by substituting the H atom with a methyl group at R^1 (compare **NTA-1**, **NTA-4**, **NTA-5**, **NTA-6** with **NTA-7**, **NTA-8**, **NTA-9**, **NTA-10**, **NTA-12**; exception – **NTA-2**, **NTA-3** and **NTA-11**).
- Substitution of the distal phenyl ring at the carbimino terminal with –Br group (**NTA-1** and **NTA-6**) increased the activity, while –Cl (**NTA-2**, **NTA-9**, **NTA-10**, **NTA-11** and **NTA-14**) and –F substitution (**NTA-3**) decreased the activity.

- Introduction of –OH group at para position of the phenyl ring at R^2 along with the methyl group at R^1 (**NTA-4**) increased the activity.
- In contrast, bulky groups like -NO_2 (**NTA-5**) and methoxy substitutions (**NTA-12**) excessively reduced the activity.
- Among the diaryl substituted analogs (**NTA-13** to **NTA-16**), chloro substitution at para position of both the phenyl rings at the carbimino terminal lead to most active derivative (**NTA-16**) followed by the monohydroxyl substituted (**NTA-15**) and unsubstituted derivative (**NTA-13**) while monochloro substituted derivative (**NTA-14**) was found to be least potent.
- Among the isatin-3-subsituted semicarbazones, 5-Br derivative (**NTA-18**) was found to be more potent than by the unsubstituted derivative (**NTA-17**).

Thus, the presence of bulkier substituents such as methoxy or nitro groups lead to reduction in the activity, whereas the compounds bearing bromo substituent on the carbimino terminal aryl ring/isatin ring displayed better potency against AChE likely demonstrating the role of electronegative bromo substituent in the stabilization of the hydrophobic ring into the active site gorge of AChE.

5.2.3.2.2. Kinetic study of lead AChE inhibitor NTA-18

In order to enlighten the mechanism of action of this family of compounds on AChE, a kinetic study was performed with the most promising compound of the series, **NTA-18**, using rat AChE. Graphical analysis of the reciprocal Lineweaver-Burk plots (**Figure 5.17.**) demonstrated increased slopes (decreased V_{max}) and intercepts (higher K_m) at increasing concentration of the inhibitor signifying a mixed-type inhibition and consequently supported the dual site binding of this compound.

5.2.3.2.3. Reversibility studies of lead AChE inhibitor NTA-18

Time-dependent inhibition study of the most active AChE inhibitor, compound **NTA-18**, was done to explore whether the observed enzyme inhibition was reversible or irreversible. No time-dependent reduction in the rates of AChE catalyzed oxidation of ACTI was observed when compound **NTA-18** was preincubated with the AChE for various periods of time i.e. 0, 15, 30, and 60 min (**Figure 5.18.**). From this result it may be deduced that the inhibition of AChE was reversible, at least for the time period (60

min). An increase of AChE catalytic rates was observed with the increase in the preincubation time of **NTA-18** with the enzyme (**Figure 5.18.**).

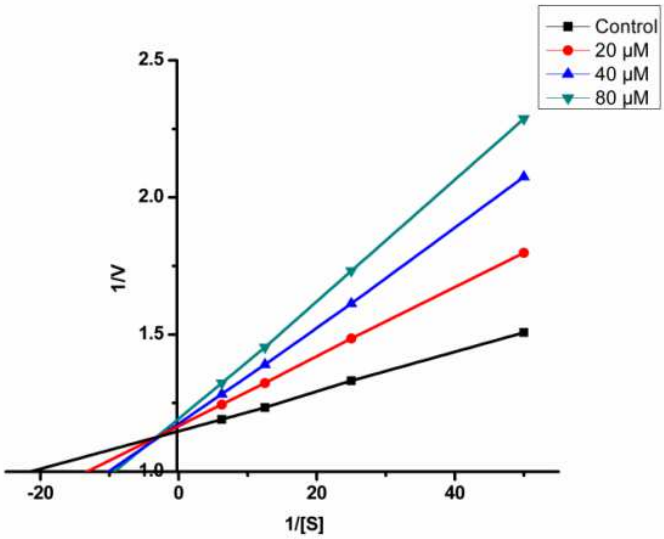

Figure 5.17. Kinetics of rat brain AChE inhibition by **NTA-18**. Lineweaver-Burk plot of the rat brain AChE catalyzed oxidation of ATCI in the absence (control) and presence of various concentrations of **NTA-18** (20 µM, 40 µM, 80 µM). Rate data are expressed as nmol product formed/min/mg protein.

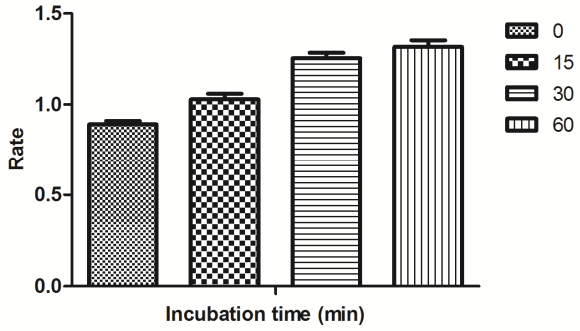

Figure 5.18. Time-dependant inhibition of AChE catalyzed oxidation of ACTI by **NTA-18**. Rate data are expressed as nmol product formed/min/mg protein.

5.2.3.2.4. Molecular docking studies of AChE inhibitors

To better understand the molecular mechanism of recombinant human AChE (rhAChE) inhibition, docking simulations were performed for all the test compounds. The test compounds were docked into the binding pocket of rhAChE in order to estimate the ligand binding affinity by means of AutoDock 4.2 using X-ray model of the rhAChE with

the PDB code 4EY7 co-crystallized with donepezil obtained from the Protein Data Bank. For each compound the corresponding theoretical inhibition constants (K_i values) and estimated binding energies (ΔG) for each virtual enzyme-ligand complex has been considered, and in accordance to the biological data, confirmed the better accommodation into the active site of rhAChE (**Table 5.10.**).

5.2.3.2.4.1. Pose analysis of AChE inhibitors

Investigation of the computationally docked binding poses of all compounds within the rhAChE active site gorge resulted in the subsequent findings: All the test compounds were found to fit into the gorge of rhAChE formed by catalytic anionic site (CAS) and peripheral anionic site (PAS) and were surrounded by the residues Tyr72, Asp74, Trp86, Gly121, Gly122, Tyr124, Ser125, Ser203, Tyr133, Ser203, Trp286, Phe295, Arg296, Phe297, Tyr337, Phe338, Tyr341, His447 (**Figure 5.19. (A)** and **(B)**) revealing a similarity in the orientation as the reference drug donepezil.

All compounds showed one or more H-bond interactions. H-bond interactions with residue Asp74 and Trp86 was observed for compound **NTA-17**; likewise with Gly121 and Gly122 for compounds **NTA-4**, **NTA-5** and **NTA-15**; with Tyr124 for compounds **NTA-1**, **NTA-4**, **NTA-5**, **NTA-8**, **NTA-13**, **NTA-14**, **NTA-15**, **NTA-16** and **NTA-18**; with Ser125 for compounds **NTA-12** and **NTA-18**; with Ser203 for compounds **NTA-4** and **NTA-8**; with Ala204 for compounds **NTA-5** and **NTA-15**; with Trp286 for compound **NTA-2**; with Phe295 for compounds **NTA-1**, **NTA-2**, **NTA-3**, **NTA-5**, **NTA-6**, **NTA-7**, **NTA-10**, **NTA-11**, **NTA-12**, **NTA-13**, **NTA-14**, **NTA-16**, **NTA-17** and **NTA-18**; with Arg296 for compounds **NTA-4**, **NTA-6**, **NTA-8**, **NTA-9**, **NTA-10**, **NTA-14**, **NTA-15** and **NTA-16**; with Tyr337 for compounds **NTA-3** and **NTA-7**; and with Tyr341 for compound **NTA-5**.

In addition, all the compounds showed π – π interactions except compound **NTA-1**, **NTA-3**, **NTA-4, NTA-6 and NTA-8**. π – π interaction with residue Phe297 was observed for compounds **NTA-2** and **NTA-5**; with Tyr341 for compounds **NTA-2**, **NTA-5**, **NTA-13** and **NTA-15**; with Trp86 for compounds **NTA-7**, **NTA-10**, **NTA-11**, **NTA-12**, **NTA-13**, **NTA-17** and **NTA-18**.

Moreover, π – cation interaction was observed with His447 for compounds **NTA-9** and **NTA-15**. Also, π – σ interaction with Trp86 was observed for compound **NTA-13**; with Phe297 for compound **NTA-14**; and with His447 for compound **NTA-15**.

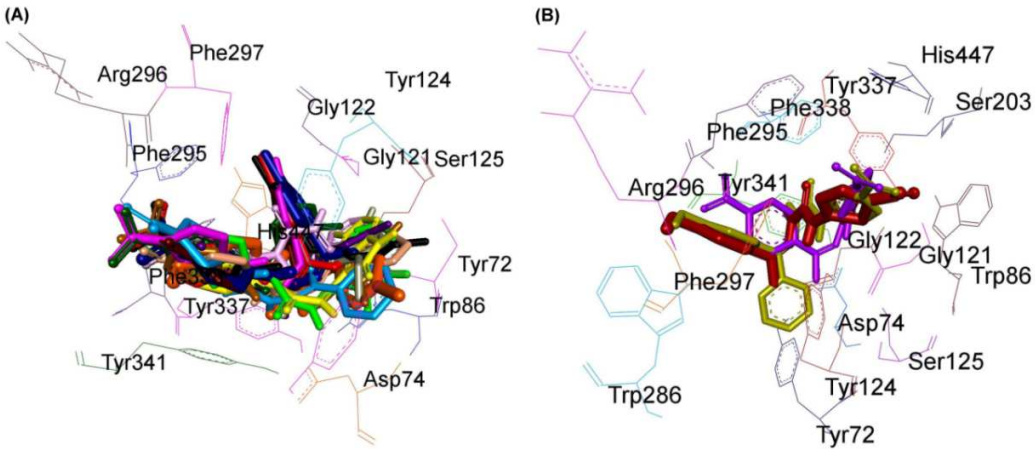

Figure 5.19. Structural screenshot of superimposed AChE inhibitors docked into the binding pocket of AChE. Selected amino acids are displayed in black. (A) Shared binding orientation of **NTA-1**, **NTA-2**, **NTA-3**, **NTA-6**, **NTA-7**, **NTA-8**, **NTA-9**, **NTA-10**, **NTA-11**, **NTA-12**, **NTA-13**, **NTA-14**, **NTA-16**, **NTA-17** and **NTA-18** are displayed in dark blue, dark brown, dark violet, red, orange, dark pink, dark green, light brown, light pink, gray, skin, sky blue, black, fluorescent green, and yellow color respectively. (B) Shared binding orientation of **NTA-4**, **NTA-5** and **NTA-15** are displayed in maroon, violet and straw green color respectively.

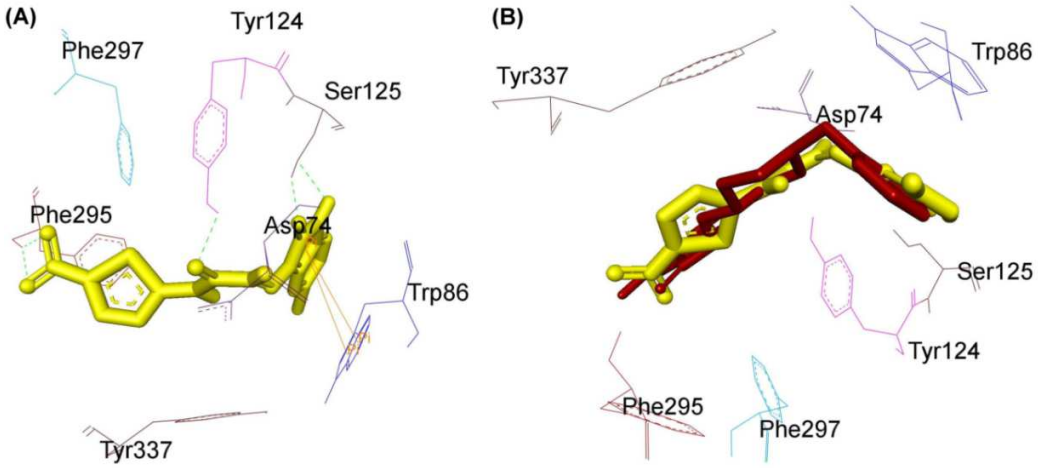

Figure 5.20. Structural screenshot of superimposed AChE inhibitors docked into the binding pocket of AChE. Selected amino acids are displayed in black. (A) Binding orientation of **NTA-18** (yellow) within the AChE binding pocket showing H-bond (green dashes) and π – π (orange colored lines) interactions. (B) Superimposed binding

orientation of **NTA-18** (yellow) within the AChE binding pocket originally docked with donepezil (maroon).

5.2.3.2.4.2. Binding mode of lead AChE inhibitor NTA-18

Evaluation of the virtual complex between the lead AChE inhibitor **NTA-18** and AChE (**Figure 5.20. (A)**) revealed that the thiazole moiety was bound to the gorge forming the PAS while the 5-bromoisatin moiety occupied the CAS, whereas the linker lies in the middle of the gorge between CAS and PAS. The binding was further stabilized by H-bond interactions between oxygen of carbimino C=O and H of OH of Tyr124; oxygen of C=O of isatin and H of OH of Ser125; oxygen of NO_2 of thiazole and H of NH of Phe295; and H of NH of isatin and oxygen of OH of Ser125. Further, 5-membered ring of isatin was involved in $\pi - \pi$ interaction with benzene and 5-membered ring of Trp86 at an inter-plane distance of approximately 5.38 Å and 4.86 Å respectively. Superimposition of rhAChE: **NTA-18** complex with the rhAChE: donepezil complex suggested that compound **NTA-18** mimicked the binding mode of donepezil (**Figure 5.20. (B)**).

5.2.3.3. Behavioural studies

5.2.3.3.1. Antidepressant activity (Porsolt's forced swim test)

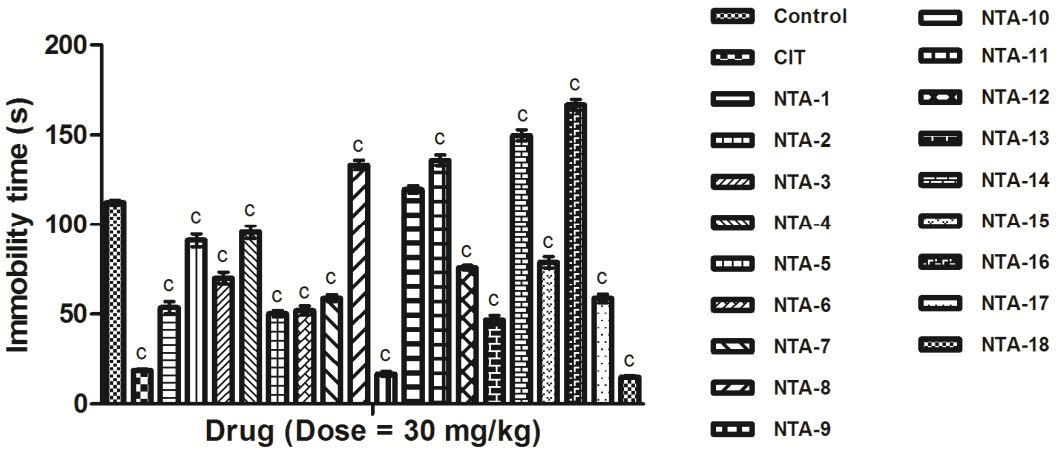

Figure 5.21. Antidepressant activity of 2-amino-5-nitrothiazole derived semicarbazones. The results are expressed as mean ± SEM ($n = 6$). The statistical significance was calculated by one-way ANOVA followed by Dunnett's test. CIT – Citalopram. $^{c}P < 0.001$ when compared with the control group.

The synthesized compounds were evaluated for their antidepressant activity using Porsolt's forced swim test and the results are illustrated in **Figure 5.21**. The compounds **NTA-9** and **NTA-18** were found to be more active than the reference drug citalopram, thereby indicating that these compounds produce no CNS depression. Rest of the compounds was found to emerge as CNS depressants as they increased the immobility time.

5.2.3.3.2. Anxiolytic activity (Elevated plus maze test)

All the compounds were subjected to anxiolytic activity screening using elevated plus maze apparatus and the results are illustrated in **Figure 5.22.**

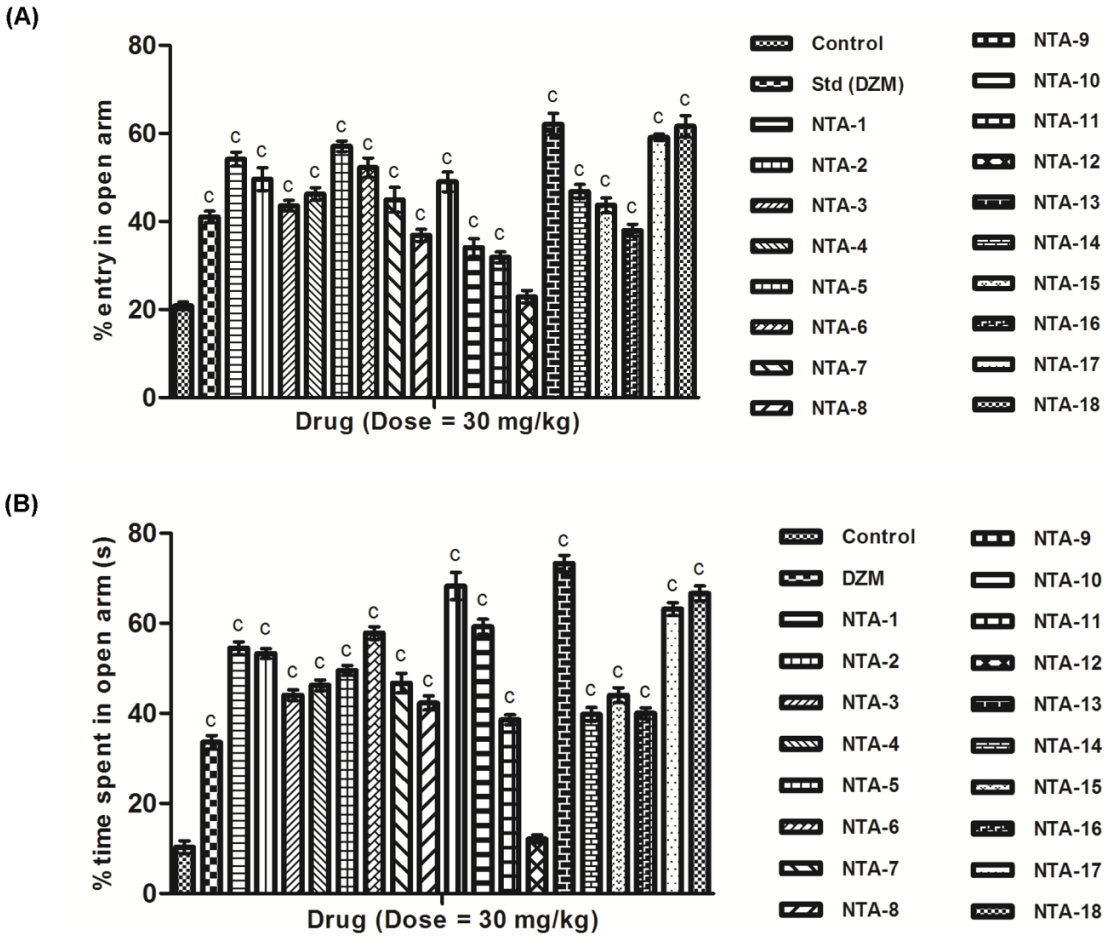

Figure 5.22. Anxiolytic activity of 2-amino-5-nitrothiazole derived semicarbazones. The results are expressed as mean ± SEM ($n = 6$). The statistical significance was calculated by one-way ANOVA followed by Dunnett's test. DZM – Diazepam. $^{c}P < 0.001$ when compared with control group.

Compounds **NTA-1**, **NTA-2**, **NTA-3**, **NTA-4**, **NTA-5**, **NTA-6**, **NTA-7**, **NTA-9**, **NTA-13**, **NTA-14**, **NTA-15**, **NTA-17** and **NTA-18** possessed significantly greater anxiolytic activity than diazepam (DZM). Rest of the compounds (**NTA-8**, **NTA-10**, **NTA-11**, **NTA-12** and **NTA-16**) was found to be less active than diazepam.

5.2.3.3.3. Sedative-hypnotic activity (Pentobarbitone potentiation test)

All the synthesized compounds were evaluated in sedative and hypnotic test at a dose of 30 mg/kg and the results are illustrated in **Figure 5.23.** Most of the compounds showed significant variation from control. None of the compounds resulted in elongation of mean sleeping time than control confirming that these compounds do not potentiate narcosis except **NTA-1**, **NTA-5** to **NTA-7**, **NTA-16** and **NTA-18**. Instead, the compounds showed antagonistic properties to barbiturates indicating that they lack the sedative side effect. However, **NTA-1**, **NTA-5** to **NTA-7**, **NTA-16** and **NTA-18** were found to potentiate narcosis.

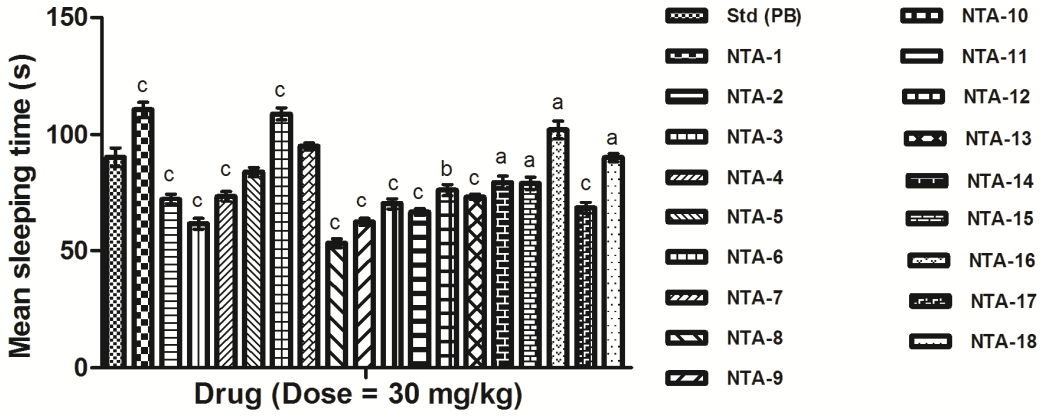

Figure 5.23. Sedative hypnotic activity of 2-amino-5-nitrothiazole derived semicarbazones. The results are expressed as mean ± SEM (*n = 6*). The statistical significance was calculated by one-way ANOVA followed by Dunnett's test. PB – Pentobarbitone. $^{a}P < 0.05$, $^{b}P < 0.01$, $^{c}P < 0.001$ when compared with control group.

5.2.3.4. Neurotoxicity screening (Rotarod test)

Selected compounds were screened for neurotoxicity by rotarod apparatus at a dose of 30 mg/kg at four time intervals viz. 0.5 h, 1 h, 2 h and 4 h. The results are presented in **Table 5.11**. All the tested compounds were found to be non-neurotoxic except **NTA-6**

and **NTA-18**. **NTA-6** was found to be moderately neurotoxic while **NTA-18** was mildly neurotoxic respectively compared to standard drug phenytoin.

Table 5.11. Neurotoxicity screening results of selected compounds of **NTA** series

Code	Neurotoxicity (Time in h)*			
	0.5	**1**	**2**	**4**
NTA-1	0/4	0/4	0/4	0/4
NTA-2	0/4	0/4	0/4	0/4
NTA-4	0/4	0/4	0/4	0/4
NTA-6	2/4	1/4	0/4	0/4
NTA-9	0/4	0/4	0/4	0/4
NTA-10	0/4	0/4	0/4	0/4
NTA-13	0/4	0/4	0/4	0/4
NTA-15	0/4	0/4	0/4	0/4
NTA-16	0/4	0/4	0/4	0/4
NTA-17	0/4	0/4	0/4	0/4
NTA-18	1/4	0/4	0/4	0/4
PHT	0/4	0/4	0/4	0/2

* The figures indicate the number of animals exhibiting toxicity/total number of animals tested. Reference drug: PHT – Phenytoin

5.2.3.5. Antioxidant activity (DPPH radical scavenging assay)

The antioxidant activity data of the selected test compounds is listed in **Table 5.12.** The DPPH· radical was scavenged by antioxidants *via* donation of hydrogen resulting in the formation of DPPH-H·. The colour of the DPPH is changed from purple to yellow after reduction, which was quantified by the decline of absorbance at a wavelength of 517 nm.

Table 5.12. Antioxidant activity of selected compounds of **NTA** series

Code	% inhibition	Code	% inhibition
NTA-1	58.68	**NTA-11**	55.29
NTA-2	51.83	**NTA-12**	10.58

NTA-3	30.43	**NTA-15**	10.77
NTA-5	11.60	**NTA-16**	24.03
NTA-6	35.89	**NTA-17**	47.16
NTA-9	42.56	**NTA-18**	65.65
NTA-10	39.39	**Ascorbic acid**	61.24

The statistical significance was calculated by one-way ANOVA followed by Dunnett's test. $P < 0.05$ when compared with control.

From the experimental results, the enhancement in the antioxidant activity was observed with most of the tested compounds. Among the tested compounds, **NTA-18** showed better antioxidant activity than ascorbic acid (**Table 5.12.**).

5.2.3.6. Liver toxicity studies

Enzyme estimation and histopathological studies of the lead MAO-A and MAO-B inhibitors (**NTA-1** and **NTA-18**) were done to check the magnitude of liver toxicity.

5.2.3.6.1. Assessment of liver function

Table 5.13. shows the liver function tests with reference to most potent compounds **NTA-1** and **NTA-18**. The estimation revealed that there was no significant increase in SGOT, SGPT, alkaline phosphatase and decrease in protein level in serum as compared to the control level (**Table 5.13.**). The results clearly indicated that **NTA-18** showed malfunctioning or toxicity of the liver whereas **NTA-1** was found to be non-toxic to liver as compared to control.

Table 5.13. Estimation of biochemical parameters **NTA-1** and **NTA-18**

Code	SGOT[a] (U/L)	SGPT[b] (U/L)	ALP (U/L)	Albumin (g/dl)	Globulin (mg/dl)	Total protein (g/dl)
Range	25.8-80.8	17.5-90	62-190	3.3-4.8	1.5-3.5	5.2-7.6
NTA-1	31.07±2.33	48.47±1.72	157.93±2.95	3.87±0.23	3.3±0.26	6.1±0.18
NTA-18	49.27±3.14	29.67±2.62	208.9±4.17	4.17±0.26	3.31±0.15	7.83±0.23
Control	38.56±1.62	51.73±2.17	151.56±2.75	3.9±0.12	1.86±0.14	6.8±0.17

Results are expressed as Mean ± SEM. The mean level was calculated using ANOVA followed by Dunnett's test; [a]Denotes serum glutamate oxaloacetate transaminase (SGOT); [b]Denotes serum glutamate pyruvate transaminase (SGPT); [c]Denotes serum alkaline phosphatase (ALP)

5.2.3.6.2. Liver histopathological studies

The Lucas technique was used to access the livers of rat, which was administered with test compounds at the dose level of 30 mg/kg body weight for 15 days and a comparison was made with the control group. Liver samples from **NTA-1** treated rat were within normal histopathological limits while the samples from **NTA-18** treated rat were found to be hepatotoxic; though less than that of CCl_4-treated samples. (**Figure 5.24.**)

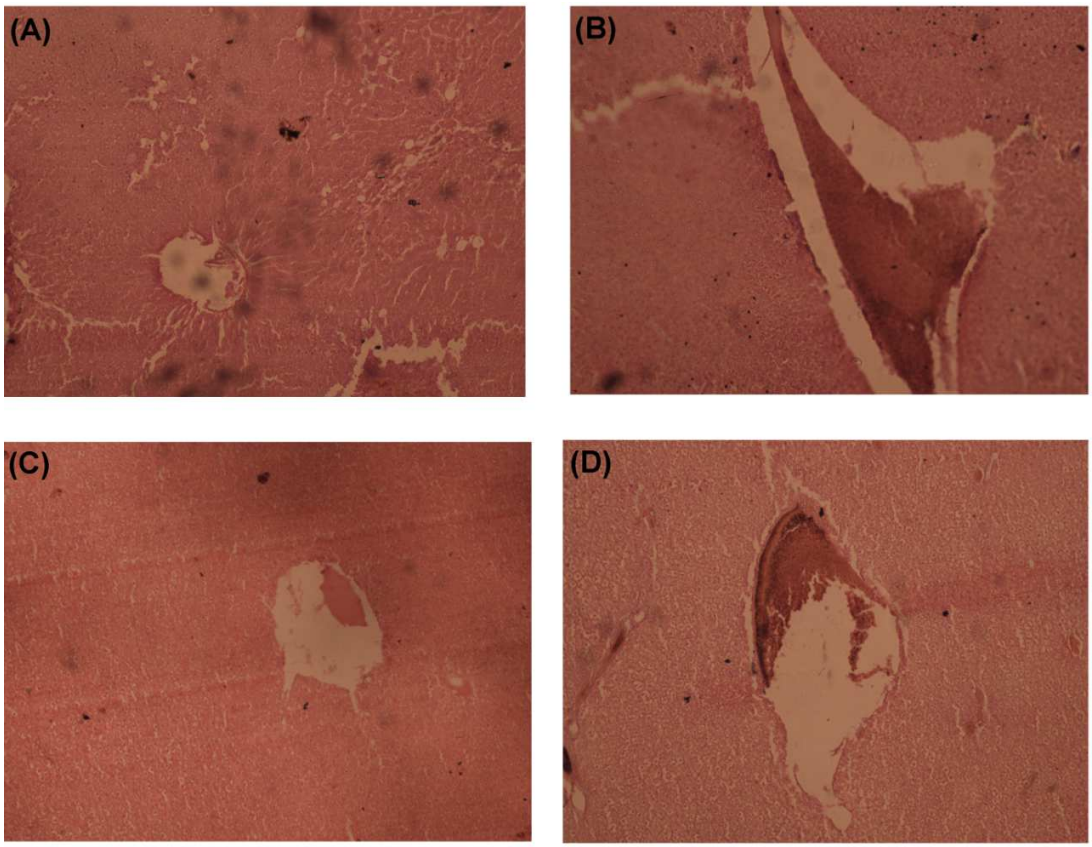

Figure 5.24. Microphotograph of the section of hematoxylin and eosin stained rat liver. Group: (A) Control (B) CCl_4-treated (C) **NTA-1** (D) **NTA-18**. Magnification: 10x.

5.2.4. *In-silico* molecular property analysis and ADMET prediction studies

In order to meet the criteria of synthesized compounds as possible drug candidates, *in-silico* molecular properties were calculated using Molinspiration online property calculation toolkit and are presented in **Table 5.14.** The molecular properties included

molecular weight (MW), lipophilicity (MiLogP), number of hydrogen bond acceptors (HBA) and number of hydrogen bond donors (HBD) of Lipinski's rule of five (reference), topological polar surface area (TPSA) and molecular volume.

The lipophilicity (expressed as MiLogP) predicted for all the compounds were found to be well the traditionally cut-off value of 5 used in drug design with the exception of compound **NTA-16**, which violated the Lipinski's rules. All the structures reported herein show suitable MW values (MW < 500) necessary for a successful penetration to CNS. The topological polar surface area (TPSA) for all the compounds was observed to be in the range 112.20-158.03 $Å^2$ which is well below the limit of 160 $Å^2$. Thus, the predicted values for all compounds **NTA-1** to **NTA-18** fall into the appropriate range indicating good bioavailability of the drug molecule. With the exception of compound **NTA-5** in which HBA was calculated to be 11, all other compounds were predicted to possess the number of hydrogen bond acceptors (HBA) and donors (HBD) within the Lipinski's limit. Thus it was predicted that almost all compounds are likely to be orally active.

Table 5.14. *In-silico* drug-likeness[a] prediction studies for **NTA-1** to **NTA-18**

Code	MW	MiLogP	HBA	HBD	$n_{violations}$	TPSA	Volume
Rule	<500	≤5	≤10	≤5	≤1	<160 $Å^2$	-
NTA-1	384.21	3.27	8	2	0	112.20	266.84
NTA-2	339.76	2.14	8	2	0	112.20	262.49
NTA-3	323.31	2.63	8	2	0	112.20	253.88
NTA-4	321.32	1.99	9	3	0	132.43	256.97
NTA-5	350.32	2.42	11	2	1	158.03	272.29
NTA-6	463.11	3.63	8	2	0	112.20	284.96
NTA-7	370.19	3.36	8	2	0	112.20	250.28
NTA-8	307.29	2.07	9	3	0	132.43	240.41
NTA-9	360.18	3.81	8	2	0	112.20	259.46
NTA-10	360.18	3.83	8	2	0	112.20	259.46
NTA-11	360.18	3.81	8	2	0	112.20	259.46
NTA-12	351.34	2.59	10	2	0	130.67	283.48
NTA-13	367.39	3.68	8	2	0	112.20	303.80

NTA-14	401.83	4.36	8	2	0	112.20	317.33
NTA-15	383.39	3.20	9	3	0	132.43	311.82
NTA-16	436.28	5.04	8	2	1	112.20	330.87
NTA-17	332.30	1.78	10	3	0	145.07	252.93
NTA-18	411.20	2.57	10	3	0	145.07	270.82

[a]MW = Molecular weight, MiLogP = octanol-water partition coefficient, HBA = Number of hydrogen bond acceptor, HBD = Number of hydrogen bond donor, $n_{violations}$ = violations from Lipinski's rule, TPSA = Topological Polar Surface Area

Furthermore, the synthesized compounds were subjected to *in-silico* ADMET (Absorption, Distribution, Metabolism, Excretion and Toxicity) property calculation using online PreADMET server. The results are presented in **Table 5.15.** and **Table 5.16.** respectively.

All the compounds expressed greater than 70% human intestinal absorption (HIA) values indicating good permeation across the membrane indicating that the compounds purport to oral administration with the exception of compounds **NTA-4**, **NTA-5**, **NTA-8**, **NTA-12** and **NTA-17**.

The *in-vitro* Caco-2 cell permeability is an important parameter to assess intestinal absorption of the drug since Caco-2 cells are derived from human colon adenocarcinoma, possessing transports *via* the intestinal epithelium. The results indicated that compounds **NTA-1**, **NTA-6**, **NTA-7** and **NTA-18** exhibited moderate permeation while rest of the compounds indicated low permeation.

The *in-vitro* MDCK cell permeability test utilizes canine kidney cells for the analysis of permeability. All the compounds showed permeation less than 25 nm/s indicating low permeability except compound **NTA-5** exhibiting moderate permeation.

All the compounds **NTA-1** to **NTA-18** exhibited negative permeability values, indicating that transdermal mode of administration is not the suitable means to administer these drugs.

The percent of drug bound with plasma proteins was estimated and almost all the compounds (except **NTA-14** and **NTA-16**) were predicted to bind weakly to plasma proteins, thereby, indicating that the compounds will be available for diffusion or transport across cell membranes and hence finally interact with the target.

The blood-brain barrier (BBB) is a separation of circulating blood and cerebrospinal fluid in the CNS, and is responsible for limiting and regulating the exchange of substances between the CNS and blood. Predicting BBB penetration means predicting whether compounds pass across the blood-brain barrier. According to the computed values, all the compounds were predicted to be inactive to CNS.

Table 5.15. *In-silico* ADME prediction data[a] of compounds **NTA-1** to **NTA-18**

Code	Absorption				Distribution	
	HIA (%)	***In-vitro* CP (nm/s)**	***In-vitro* MDCK (nm/s)**	***In-vitro* SP (log K_p, cm/h)**	***In-vitro* PPB (%)**	***In-vivo* BBB (C_{brain}/ C_{blood})**
Rule	0-20 (poor) 20-70 (moderate) 70-100 (well)	<4 (low) 4-70 (moderate) >70 (high)	<25 (low) 25-500 (moderate) >500 (high)		>90 (strongly bound) <90 (weakly bound)	> 0.1 (CNS active) < 0.1 (CNS inactive)
NTA-1	89.55	9.56	0.05	-3.96	79.01	0.014
NTA-2	84.25	0.52	1.27	-4.05	75.95	0.014
NTA-3	72.05	0.39	8.91	-4.28	67.73	0.016
NTA-4	48.97	0.36	19.36	-4.45	57.88	0.014
NTA-5	25.18	0.35	27.08	-4.11	76.11	0.054
NTA-6	95.59	19.71	0.07	-3.66	86.94	0.011
NTA-7	88.25	7.59	0.04	-4.03	81.17	0.018
NTA-8	45.17	0.34	21.61	-4.46	58.90	0.017
NTA-9	90.17	0.58	0.24	-3.89	85.96	0.058
NTA-10	90.17	0.50	0.13	-3.90	85.76	0.037
NTA-11	90.17	0.50	0.18	-3.88	87.35	0.099
NTA-12	57.71	0.50	17.91	-3.99	61.53	0.069
NTA-13	90.31	0.49	0.08	-3.34	87.52	0.011

NTA-14	94.39	0.49	0.05	-3.28	90.06	0.012
NTA-15	79.15	0.37	0.07	-3.78	88.51	0.012
NTA-16	96.12	0.54	0.05	-3.12	93.30	0.014
NTA-17	53.32	0.42	19.89	-4.87	62.08	0.016
NTA-18	79.87	15.97	0.08	-4.82	79.93	0.016

[a]HIA – Human Intestinal Absorption, CP – Caco2 cell permeability, MDCK – MDCK cell permeability, SP – skin permeability, PPB – Plasma protein binding, BBB – Blood brain barrier.

The Ames test assesses mutagenicity of the compounds. All the compounds were predicted as mutagen. Besides, carcinogenicity test was performed to identify the tumerogenic potential of compounds in animals (mouse and rat). When analyzing carcinogenicity in mice, all the compounds were predicted as negative. By analyzing rat carcinogenicity, all the compounds were predicted positive except compounds **NTA-5**, **NTA-15**, **NTA-16** and **NTA-17** which presented negative predictions. Human ether-a-go-go-related gene (hERG) encodes potassium channels, which are responsible for normal repolarization of cardiac action potentials. Blockage or any other impairment of these channels in the heart can lead to fatal cardiac problems. Hence, drug-induced blockage of potassium channels has been a major concern. All the compounds presented medium risk except compound **NTA-5**, **NTA-13**, **NTA-15**, **NTA-17** and **NTA-18** which presented low risk while compound **NTA-16** presented high risk and compound **NTA-14** presented ambiguous results against hERG inhibition.

Table 5.16. *In-silico* toxicity prediction data of compounds **NTA-1** to **NTA-18**

Code	Ames test	Carcinogenicity (Mouse)	Carcinogenicity (Rat)	hERG inhibition
NTA-1	Mutagen	Negative	Positive	Medium risk
NTA-2	Mutagen	Negative	Positive	Medium risk
NTA-3	Mutagen	Negative	Positive	Medium risk
NTA-4	Mutagen	Negative	Positive	Medium risk

NTA-5	Mutagen	Negative	Negative	Low risk
NTA-6	Mutagen	Negative	Positive	Medium risk
NTA-7	Mutagen	Negative	Positive	Medium risk
NTA-8	Mutagen	Negative	Positive	Medium risk
NTA-9	Mutagen	Negative	Positive	Medium risk
NTA-10	Mutagen	Negative	Positive	Medium risk
NTA-11	Mutagen	Negative	Positive	Medium risk
NTA-12	Mutagen	Negative	Positive	Medium risk
NTA-13	Mutagen	Negative	Positive	Low risk
NTA-14	Mutagen	Negative	Positive	Ambiguous
NTA-15	Mutagen	Negative	Negative	Low risk
NTA-16	Mutagen	Negative	Negative	High risk
NTA-17	Mutagen	Negative	Negative	Low risk
NTA-18	Mutagen	Negative	Positive	Low risk

Thus, it can be concluded that compounds **NTA-1** and **NTA-18** presents the good drug-like characteristics and ADMET properties among others.

5.3. 3,4-(METHYLENEDIOXY)ANILINE DERIVED SEMICARBAZONES [MDA-1 to MDA-14]

5.3.1. Synthesis

3,4-(Methylenedioxy)aniline derived semicarbazones (**MDA-1** to **MDA-14**) were obtained by refluxing semicarbazide with appropriate aldehydes or ketones according to the reaction scheme depicted in **Scheme 4.6.**, by optimizing the various reaction variables, *viz*. solvents, catalyst, temperature, stirring time, etc. The final compounds were recrystallized using methanol as a solvent.

All the final products were stable to open air environment. The intermediates (**MDU** and **MDA**) and final products were obtained in moderate yield (40 to 60%) except **MDA-4** (39.31%).

The products (**MDA-1** to **MDA-14**) were obtained as crystalline solids (**MDA-2** to **MDA-7** and **MDA-9** to **MDA-14**) or amorphous powder (**MDA-1** and **MDA-8**). The final compounds were of black (**MDA-1** to **MDA-11**) or reddish black (**MDA-12** to **MDA-14**) colour.

5.3.2. Characterization

5.3.2.1. Physicochemical characterization

5.3.2.1.1. Melting point

Melting points were determined in one end open capillary tubes on Sonar melting point apparatus and were uncorrected. All the synthesized compounds displayed a phase change from solid to liquid state and thus exhibited melting range of 2 to 5 °C indicating the purity of compounds except **MDA-1** which charred at 180 °C. The observed melting point ranges for the synthesized compounds **MDA-1** to **MDA-14** are presented in the **Table 4.8.**

5.3.2.1.2. Solubility

The solubility of all the synthesized compounds was determined in various solvents at room temperature. All intermediates (**MDU** and **MDS**) and final compounds (**MDA-1** to **MDA-14**) were insoluble or partially soluble in water but soluble in chloroform, methanol, ethanol, dichloromethane, DMSO and DMF. The observed solubility data are listed in **Table 4.8.**

5.3.2.1.3. Thin layer chromatography

Thin layer chromatography (TLC) was performed during the synthesis to monitor the progress of the reaction. . For each reaction, single distinct spot of product and absence of reactant spot in TLC analysis indicated the completion of reaction and the purity of synthesized compounds. TLC was also performed for the final compounds (**MDA-1** to **MDA-14**) after purification to determine their R_f values. The observed R_f values are presented in the **Table 4.8.** Depending upon the polarity of compounds, the composition of eluents used for TLC analysis was (i) Dichloromethane: Methanol (9.8:0.2).

5.3.2.1.4. Determination of partition coefficient (LogP)

The synthesized compounds were found to exhibit experimental LogP values in the range 0.9 – 3.5 (shake flask method) indicating that they possess adequate lipophilicity necessary for their solubility in the lipid phase. The experimental (determined through Shake flask method) and calculated LogP (software calculated) values are listed in **Table 4.8.**

5.3.2.2. Spectral characterization and elemental analysis

5.3.2.2.1. Ultraviolet (UV) spectroscopy

All the compounds exhibited prominent absorption bands with respect to the chromophore. The compounds of **MDA** series exhibited absorption bands due to C=N and C=O chromophores at λ_{max} 248-270 nm and 290-320 nm respectively owing to $n \rightarrow \pi^*$ transition.

5.3.2.2.2. Infrared (IR) spectroscopy

The semicarbazones showed characteristic absorption in the functional group region at 3200-3500 cm^{-1} and 1600-1680 cm^{-1} which confirmed the presence of NH (str) and C=O (str) of the amide respectively. Further, the formation of semicarbazones were confirmed by the presence of -C=N (str.) at 1520-1640 cm^{-1}. The characteristic absorption in the range 1300-1350 cm^{-1} and 1450-1475 cm^{-1} (**MDA-14**) confirmed the presence of Ar-NO_2 (str) while that in the range 1000-1300 cm^{-1} confirmed the presence of C-O-C (str). The presence of C=O (str) group of indole ring of isatin was confirmed by the characteristic absorption in the range 1680-1740 cm^{-1} (**MDA-12** to **MDA-14**). The presence of characteristic absorptions around 2890-3000 cm^{-1} confirmed the presence of CH_2 stretching while the presence of C=C (str) in the aromatic ring was confirmed by the

characteristic absorptions in the range 1400-1600 cm^{-1}. The presence of halogens was confirmed by the absorptions in the range 500-850 cm^{-1} for C-Cl (**MDA-2**, **MDA-5** to **MDA-7**, **MDA-10** to **MDA-11** and **MDA-13**) and 950-1100 cm^{-1} for C-F groups (**MDA-3**) while the presence of OH str was confirmed by the absorption at 3478.26 cm^{-1} (**MDA-4**).

5.3.2.2.3. Nuclear magnetic resonance (NMR) spectroscopy

^{1}H NMR spectra of all the 3,4-(methylenedioxy)aniline derived semicarbazones showed a characteristic singlet peak at δ 3.32-3.62 ppm, δ 5.84-6.05 ppm and δ 9.63-9.98 ppm indicating $–CH_2–$, –NH– and –CONH– protons, respectively. The appearance of multiplets at δ 6.28-8.71 ppm confirmed the presence of aromatic protons. The singlet at δ 7.55-8.80 ppm (**MDA-5** to **MDA-8**) and δ 1.96-1.98 ppm (**MDA-1** to **MDA-4**) indicated the C-H, and $C\text{-}CH_3$ groups respectively. In ^{1}H NMR spectra of semicarbazones having indolyl group, a singlet was observed at δ 8.19-8.28 ppm (**MDA-12** to **MDA-14**) due to >NH of indole ring which was supported by the N–H str. The singlet at δ 3.29 ppm (**MDA-8**) and δ 4.91 ppm (**MDA-4**) indicated the presence of OCH_3 and OH protons respectively. The disappearance of signals of amino NH and carbimino NH indicated the presence of exchangeable protons (**MDA-12**; **Figure 4.73.**)

In ^{13}C NMR spectra, the appearance of signals in the range of δ 156.28-168.53 ppm confirmed the presence of carbonyl group of semicarbazone linker. Moreover, ^{13}C NMR spectra showed signals in the range of δ 133.13-167.90 ppm which was due to C=N carbon. The presence of OCH_3 group was also confirmed by the signal at δ 57.51 ppm (**MDA-8**). Clustered signals in the range of δ 101.22-151.25 ppm corresponded to the presence of aryl carbons. Characteristic signals at δ 23.82-23.84 ppm (**MDA-1** to **MDA-4**) and δ 179.01-179.62 ppm (**MDA-12** to **MDA-14**) corresponded to CH_3 and oxindole C=O respectively.

5.3.2.2.4. Mass spectrometry

Compounds **MDA-3** and **MDA-8** were subjected to mass analysis. **MDA-3** (Mol. wt. = 315.3) showed an $[M+1]^+$ peak of 316.58 (**Figure 4.60.)** and **MDA-8** (Mol. wt. = 443.33) showed an $[M+1]^+$ peak of 344.98 (**Figure 4.67.)** thereby confirming the structure of the compounds.

5.3.2.2.5. Elemental analysis

All the compounds **MDA-1** to **MDA-14** were subjected to elemental analysis and the observed values were within ± 0.4% of the calculated values.

5.3.2.2.5. Powder X-ray diffraction analysis

Compound **MDA-2** was subjected to the powder X-ray diffraction analysis to confirm the crystallinity of the compound. The diffraction pattern of **MDA-2** (**Figure 4.56.**) comprised of sharp peaks thereby indicating the crystalline nature of the compound.

5.3.3. Biological evaluation

5.3.3.1. Monoamine oxidase (MAO) enzyme inhibition studies

5.3.3.1.1. *In-vitro* MAO inhibition assay

The inhibitory activities against MAO-A and MAO-B isozymes were investigated by measuring the effects of each compound on the production of 5-hydroxyindole acetic acid from serotonin (5-HT) for MAO-A and benzaldehdye from benzylamine for MAO-B, using the UV based spectrophotometric MAO enzyme inhibition assay. Clorgyline and selegiline were used as reference inhibitors for MAO-A and MAO-B respectively. The corresponding IC_{50} values and MAO-B selectivity ratios are presented in **Table 5.17.**

Table 5.17. *In-vitro* and computational MAO inhibition data for **MDA-1** to **MDA-14**

Code	MAO-A			MAO-B			SI[a]
	In-vitro	Computational		*In-vitro*	Computational		
	IC_{50} (µM) ± SEM	ΔG*	K_i (µM)	IC_{50} (µM) ± SEM	ΔG*	K_i (µM)	
MDA-1	52.46 ± 2.36	-6.35	22.3	22.89 ± 1.21	-7.16	5.66	2.29
MDA-2	32.83 ± 1.43	-6.55	15.81	1.107 ± 0.004	-7.42	3.67	29.66
MDA-3	47.81 ± 3.21	-6.29	24.49	128.2 ± 2.73	-6.62	13.93	0.37
MDA-4	NT	-6.4	20.27	NT	-6.75	11.2	-
MDA-5	2.25 ± 0.016	-7.01	7.26	0.54 ± 0.008	-7.46	3.41	4.17
MDA-6	1.99 ± 0.010	-6.77	10.82	31.46 ± 1.77	-6.56	15.49	0.06

MDA-7	4.52 ± 0.032	-6.82	9.98	0.059 ± 0.002	-7.8	1.92	76.61
MDA-8	225.0 ± 5.82	-5.82	54.1	89.85 ± 3.19	-6.75	11.19	2.50
MDA-9	0.24 ± 0.003	-7.17	5.53	2.552 ± 0.034	-7.32	4.3	0.09
MDA-10	82.82 ± 4.53	-6.02	38.61	54.29 ± 1.12	-6.53	16.22	1.53
MDA-11	NT[b]	-5.28	135.3	NT[b]	-5.82	54.37	-
MDA-12	3.26 ± 0.031	-6.82	10.1	13.40 ± 0.015	-7.0	7.34	0.24
MDA-13	16.40 ± 0.011	-6.64	13.62	7.253 ± 0.002	-7.17	5.57	5.04
MDA-14	32.17 ± 0.064	-6.33	22.8	14.95 ± 0.011	-7.26	4.77	2.15
CLG	0.0044 ± 0.462	-	-	-	-	-	-
SEL	67.25 ± 1.02	-	-	0.020 ± 0.0008	-	-	-
HRM	3.00	-5.3	130.82	7000	-	-	-
SAF	-	-	-	0.100	-5.93	45.23	-

*ΔG is expressed in $kcalmol^{-1}$; [a]SI – The selectivity index is the selectivity for the MAO-B isoform and is given as the ratio of experimental IC_{50}(MAO-A)/IC_{50}(MAO-B); NT – not tested; Reference inhibitors: CLG – Clorgyline, SEL – Selegiline, HRM – Harmine, SAF – Safinamide.

Note: Each IC_{50} value is the mean ± SEM. It refers to the assay concentration of test compound which leads to 50% inhibition of enzyme activity. Level of statistical significance: $P < 0.05$ versus the corresponding IC_{50} values obtained against MAO-A and MAO-B; as determined by ANOVA/Dunnett's.

Based on the screening data (**Table 5.17.**), it could be seen that most of the tested compounds displayed better inhibitory potential against MAO-B than MAO-A with the IC_{50} values in the micromolar to nanomolar range. The IC_{50} values towards MAO-A range from 0.24 ± 0.003 µM (**MDA-9**) to 225.0 ± 5.82 µM (**MDA-8**) while for MAO-B range from 0.059 ± 0.002 µM (**MDA-7**) to 128.2 ± 2.73 µM (**MDA-3**).

Among the synthesized compounds, 4-(benzo[1,3]dioxol-5-yl)-1-(diphenylmethylene)-semicarbazide (**MDA-9**) delivered highest potency against MAO-A with IC_{50} value of 0.24 ± 0.003 µM, whereas the most active MAO-B inhibitor, 1-(2,6-dichlorobenzylidene)-4-(benzo[1,3]dioxol-5-yl)semicarbazide (**MDA-7**) was found to

exhibit an IC_{50} value of 0.059 ± 0.002 µM with the highest selectivity index of 76.61 against MAO-B in the study.

To shed some light into the SARs, focused structural modifications were attempted at the carbimino terminal of the semicarbazone resulting in the variations in the activity. Particularly, increase in the lipophilicity caused by the incorporation of halogen-substituted (-Cl) aryl systems or diaryl or isatin residues preferably with halogen substituents (-Cl) at the carbimino terminal resulted in increased inhibition against MAO-B compared to MAO-A.

Structure-activity relationship (SAR)

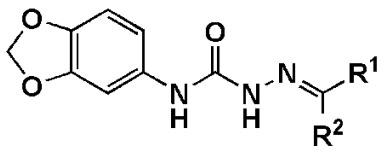

MDA-1 to MDA-11

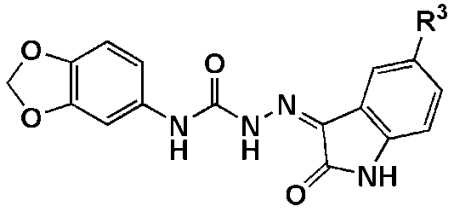

MDA-12 to MDA-14

- Introduction of chloro groups on the phenyl ring at the carbimino terminal (R^2) increased the activity towards both the isozymes with more potency and selectivity towards MAO-B (**MDA-7**, **MDA-5** and **MDA-2**) rather than MAO-A (**MDA-6**).
- Dichloro substituted compounds (**MDA-7** and **MDA-5**) exhibited more MAO-B inhibition activity than the monochloro substituted derivative (**MDA-2**).
- Fluoro substitution on the phenyl ring at the carbimino terminal (R^2) (**MDA-3**) resulted in a remarkable reduction in the activity towards MAO-B.
- Dimethoxy substitution on the phenyl ring at the carbimino terminal (R^2) caused an excessive decrease in the activity towards both the enzymes (**MDA-8**).
- The unsubstituted benzophenone derivative (**MDA-9**) expressed better MAO-A activity than the monochloro substituted derivative (**MDA-10**).
- Among the isatin-3-substituted semicarbazones (**MDA-12** to **MDA-14**), 5-Cl substituted derivative (**MDA-13**) was found to be more potent for MAO-B followed by unsubstituted (**MDA-12**) and $–NO_2$ substituted derivative (**MDA-14**). Whereas, the unsubstituted derivative (**MDA-14**) was found to be more potent

against MAO-A. 5-Cl substitution (**MDA-13**) resulted in decrease in the activity towards MAO-A while $–NO_2$ substitution (**MDA-14**) further reduced the activity.

These results guided us towards the influence of the steric groups and electronegative substituent(s) on the MAO inhibitory profile.

5.3.3.1.2. Kinetic studies of lead MAO inhibitors (MDA-9 and MDA-7)

To further examine the modes of MAO-A and MAO-B inhibition, sets of Lineweaver-Burk plots were constructed for the inhibition of MAO-A enzyme by **MDA-9** and MAO-B by **MDA-7**, the representative lead MAO-A and MAO-B inhibitor respectively (**Figure 5.25.**). Inspection of Lineweaver-Burk plots suggested that the plots of **MDA-9** (**Figure 5.25. (A)**) and **MDA-7** (**Figure 5.25. (B)**) were linear and intersected at the Y-axis. The pattern indicated that **MDA-9** and **MDA-7** respectively inhibited MAO-A and MAO-B competitively, and these results further proved that they were reversible MAO-A and MAO-B inhibitors.

5.3.3.1.2.1. Determination of K_i for lead MAO inhibitors (MDA-9 and MDA-7)

For each type of mode of inhibition, the dissociation constant (K_i) can be calculated for the inhibitor that reflects the strength of interactions between the enzyme and the inhibitor. K_i for the lead inhibitors (**MDA-9** and **MDA-7**) was calculated using the GraphPad Prism resulting in the K_i value of 12.504 ± 0.004 nM for **MDA-9** against MAO-A and 8.862 ± 0.003 nM for **MDA-7** against MAO-B. On comparing the IC_{50} values with the K_i values, a 19-fold difference was observed for **MDA-9** and a 6-fold difference was observed for **MDA-7** which reflects tight binding of these inhibitors to the enzyme.

5.3.3.1.3. Reversibility and irreversibility experiments for lead MAO inhibitors

Further the lead MAO-A and MAO-B inhibitors (**MDA-9** and **MDA-7)** were subjected to time-dependent inhibition studies to investigate whether the observed enzyme inhibition is reversible or irreversible. Reversibility test was performed using the slightly modified method described by Legoabe *et al*. There is no time-dependent reduction in the rates of MAO-A catalyzed oxidation of serotonin (**Figure 5.26. (A)**) and MAO-B catalyzed oxidation of benzylamine (**Figure 5.26. (B)**) respectively when **MDA-9** and **MDA-7** was

preincubated with the MAO-A and MAO-B enzymes respectively for various periods of time i.e. 0, 15, 30, and 60 min. From this result, it can be concluded that the inhibition of both MAO-A and MAO-B by **MDA-9** and **MDA-7** respectively is reversible, at least for the time period (60 min). Interestingly, an increase of MAO-A and MAO-B catalytic rates with increased preincubation time of **MDA-9** and **MDA-7** with the enzyme was observed.

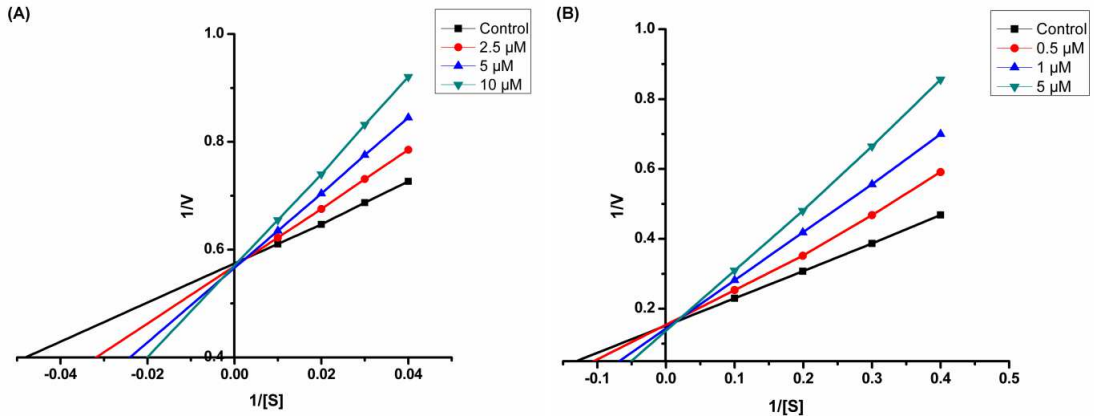

Figure 5.25. Kinetics of rat brain MAO-A inhibition by **MDA-9** and MAO-B inhibition by **MDA-7**. (A) Lineweaver-Burk plot of the rat brain MAO-A catalyzed oxidation of serotonin in the absence (control) and presence of various concentrations of **MDA-9** (2.5 µM, 5 µM, 10 µM). (B) Lineweave-Burk plot of the rat brain MAO-B catalyzed oxidation of benzylamine in the absence (control) and presence of various concentrations of **MDA-7** (0.5 µM, 1 µM, 5 µM). Rates (V) are expressed as nmol product formed/min/mg protein.

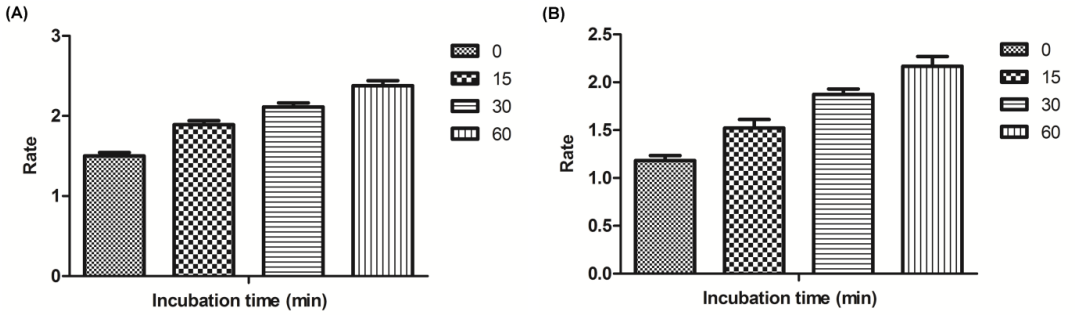

Figure 5.26. Time-dependent inhibition of (A) MAO-A catalyzed oxidation of serotonin by **MDA-9**. (B) MAO-B catalyzed oxidation of benzylamine by **MDA-7**. Rates (V) are expressed as nmol product formed/min/mg protein.

5.3.3.1.4. Molecular docking studies of MAO inhibitors

In order to explore the peculiar binding modes and interactions of these semicarbazones with MAO-A and MAO-B and to gain insights into the affinity, a structure based molecular modeling study was carried out using hMAO-A and hMAO-B cocrystals obtained from PDB. The crystallographic structure of MAO-A (PDB: 2Z5X) and MAO-B (PDB: 2V5Z) was used to dock the derivatives under study. The molecular docking study was performed using automated docking program AutoDock 4.2. The conformers possessing the best score from the largest cluster were considered for further structural and binding orientation and feasible enzyme-inhibitor interaction studies. The results of molecular modeling studies for both MAO-A and MAO-B expressed in terms of theoretical inhibition constants (K_i values) and estimated free energies of binding (ΔG) for each virtual enzyme-inhibitor complex are presented in **Table 5.17.**

5.3.3.1.4.1. Pose analysis of MAO-A inhibitors

Visual inspection of the computationally docked binding poses of all compounds within the MAO-A active site resulted in the following observations: Overall, all the test inhibitors occupied the active centre cavity of the MAO-A enzyme and were surrounded by the residues Tyr69, Ile 180, Asn181, Phe208, Val210, Gln215, Cys323, Ile 325, Ile335, Phe352, Tyr407, Tyr444 and FAD (**Figure 5.27. (A)** and **(B)**) which was analogous to the binding site of the harmine, a reference MAO-A inhibitor. Almost in all the test inhibitors the (methyelenedioxy)phenyl moiety occupies the cavity extending towards FAD while the arylidene or diarylmethylene or isatin residue is located towards the opening of the cavity (**Figure 5.27. (A)**). A few exceptions are found with **MDA-10**, **MDA-12**, **MDA-13** and **MDA-14**; for which the binding orientation is completely the reverse (**Figure 5.27. (B)**). Further, these inhibitors are stabilized by hydrogen bonding (H-bond) and hydrophobic ($\pi - \pi$ stacking) interactions.

All compounds showed one or more H-bond interactions except **MDA-1** and **MDA-3**. H-bond interaction with residue Tyr197 is observed with **MDA-2**, **MDA-4**, **MDA-5**, **MDA-6**, **MDA-7**, **MDA-8**, **MDA-9**, **MDA-11** and **MDA-14**; likewise with Ala111 in **MDA-4**; with Asn181 in **MDA-10** and **MDA-12**; with Cys323 in **MDA-14**; with Tyr407 in **MDA-7** and **MDA-11**; with Tyr444 in **MDA-14**; and with FAD in **MDA-10**, **MDA-12** and **MDA-13**. In addition, all the compounds showed $\pi - \pi$ interactions. $\pi - \pi$ interactions

with residue Tyr407 is observed with **MDA-1**, **MDA-2**, **MDA-3**, **MDA-4**, **MDA-5**, **MDA-6**, **MDA-7**, **MDA-8**, **MDA-9**, **MDA-11**, **MDA-12**, **MDA-13** and **MDA-14**; likewise with Tyr444 in **MDA-1**, **MDA-2**, **MDA-3**, **MDA-4**, **MDA-5**, **MDA-6**, **MDA-7**, **MDA-9**, **MDA-11** and **MDA-12**; and with Phe352 in **MDA-10** and **MDA-11**. Besides, **MDA-11** is stabilized by π – σ interaction with Met350; and **MDA-12** with FAD respectively. Thus, in most of the potent compounds, preferably π – π and H-bond interactions have been found to be responsible for mediating the inhibitory activity against MAO-A.

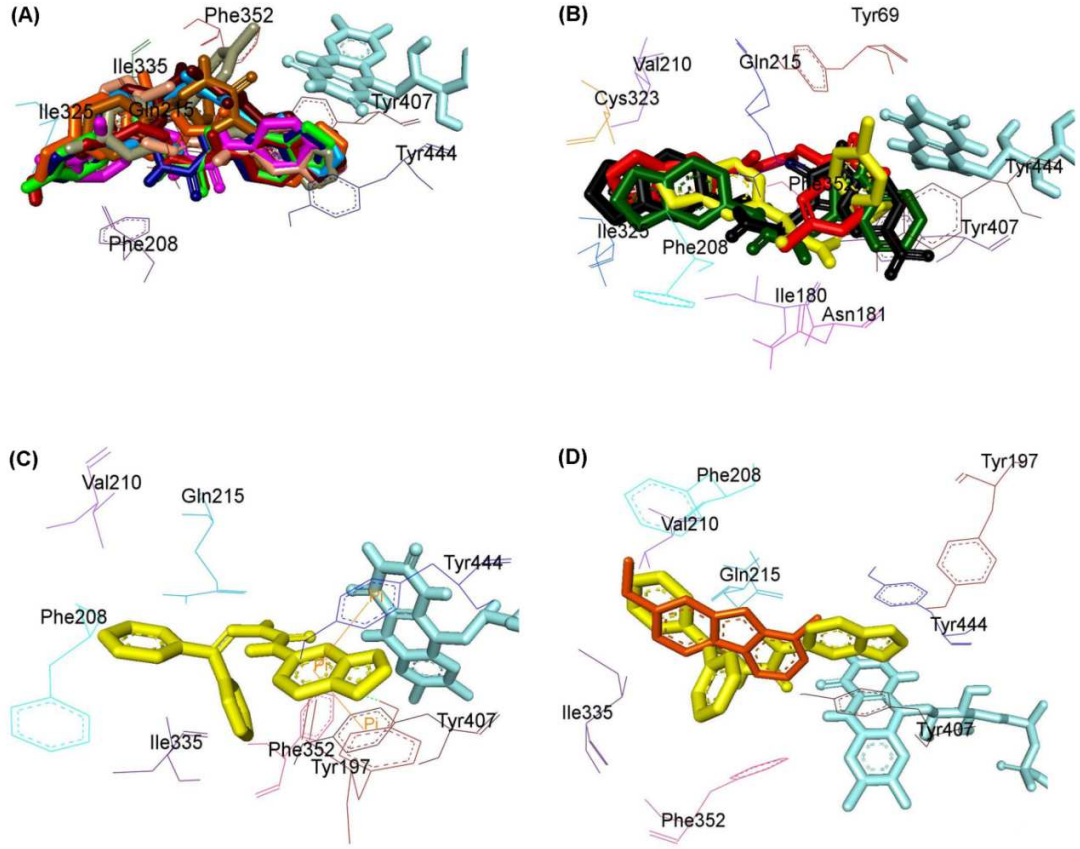

Figure 5.27. Structural screenshot of superimposed MAO-A inhibitors docked into the active site of MAO-A. FAD is displayed in cyanin. Selected amino acids are depicted in black. (A) Shared binding modes of **MDA-1**, **MDA-2, MDA-3, MDA-4, MDA-5, MDA-6**, **MDA-7**, **MDA-8**, **MDA-9** and **MDA-11** displayed in dark blue, dark brown, fluorescent green, maroon, dark pink, sky blue, skin, dark orange, light brown and gray color respectively. (B) Shared binding modes of **MDA-10**, **MDA-12**, **MDA-13** and **MDA-14** displayed in yellow, maroon, dark green and dark pink color respectively. (C) Binding orientation of **MDA-9** (yellow) within MAO-A active site showing π – π (orange

colored lines) and H-bond (green dashes) interactions. (D) Superimposed binding mode of **MDA-9** (yellow) within MAO-A originally docked with harmine (orange).

5.3.3.1.4.2. Binding mode of lead MAO-A inhibitor MDA-9

Inspection of the virtual complex of the lead MAO-A inhibitor **MDA-9** and MAO-A (**Figure 5.27. (C)**) reveals that semicarbazone linker is situated in the centre of the cavity with the (methylendioxy)phenyl moiety located towards FAD while the diarylmethylene moiety is situated towards the opening of the MAO-A receptor. The benzene ring of the (methylendioxy)phenyl moiety is involved in $\pi - \pi$ interaction with Tyr407 and Tyr444 at an inter-plane distance of approximately 3.71 Å and 4.74 Å respectively. Besides this, the molecule is also stabilized by H-bond interaction between O of dioxole ring and H of OH of Tyr197 at an inter-plane distance of approximately 2.14 Å. **Figure 5.27. (D)** shows the docked pose of **MDA-9** (yellow) within the MAO-A active site superimposed with the docked pose of harmine (orange) which indicates that both share a similar binding orientation further strengthening our finding.

5.3.3.1.4.3. Pose analysis of MAO-B inhibitors

All the inhibitors are located within the active site cavity of MAO-B. The binding orientation of all the test inhibitors within MAO-B traverses both the entrance cavity surrounded by the residues Leu171, Phe168, Ile198, Ile199 and Tyr326; and substrate cavity surrounded by the residues Tyr60, Cys172, Gln206, Phe343, Tyr398 and Tyr435 which is almost similar to the binding orientation of the reference MAO-B inhibitor, safinamide. Almost in all the test inhibitors the (methylenedioxy)phenyl moiety occupies the cavity extending towards FAD while the arylidene or diarylmethylene or isatin residue is located towards the opening of the cavity (**Figure 5.28. (A)**). A few exceptions are found with the **MDA-6**, **MDA-11** and **MDA-13** for which the binding orientation is completely the reverse (**Figure 5.28. (B)**). Additionally, the inhibitors are stabilized by H-bond and/or $\pi - \pi$ stacking interactions.

All the compounds showed H-bond interactions except **MDA-1**, **MDA-3**, **MDA-8**, **MDA-9**, **MDA-10** and **MDA-12**. H-bond interactions with residue Phe168 is observed in **MDA-14**; likewise with Cys172 in **MDA-13** and **MDA-14**; with Ile198 in **MDA-2**, **MDA-4**, **MDA-5**, **MDA-6**, **MDA-7**, and **MDA-14**; with Gln206 in **MDA-11**; with Tyr326 in **MDA-11** and **MDA-14**; with Tyr398 in **MDA-4**; with Tyr435 in **MDA-2**,

MDA-4, **MDA-5**, **MDA-7**, and **MDA-14**; and with FAD in **MDA-6**. Besides, π – π interactions is observed with Tyr398 in **MDA-1**, **MDA-2**, **MDA-3**, **MDA-4**, **MDA-5**, **MDA-6**, **MDA-7**, **MDA-8**, **MDA-10**, **MDA-11**, **MDA-12** and **MDA-14**; likewise with Tyr326 in **MDA-1** and **MDA-7**; with Tyr435 in **MDA-2**, **MDA-4**, **MDA-5**, **MDA-7**, **MDA-9**, **MDA-12** and **MDA-13**. Additionally, π – σ interaction is observed with Ile199 in **MDA-13**. Thus, in most of the potent inhibitors, preferably π – π and H-bond interactions have been found to be responsible for mediating inhibition against MAO-B.

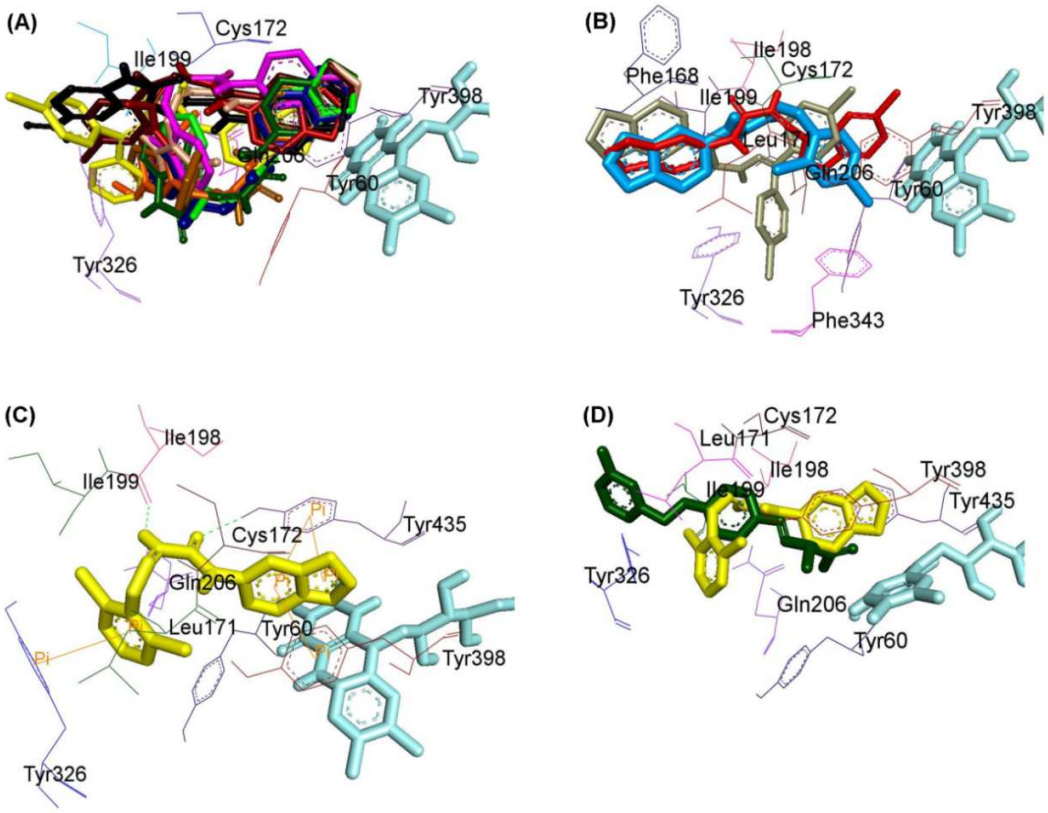

Figure 5.28. Structural screenshot of superimposed MAO-B inhibitors docked into the active site of MAO-B. FAD is displayed in cyanin. Selected amino acids are displayed in black. (A) Shared binding modes of **MDA-1**, **MDA-2**, **MDA-3**, **MDA-4**, **MDA-5**, **MDA-7**, **MDA-8**, **MDA-9**, **MDA-10**, **MDA-12** and **MDA-14** are displayed in dark blue, dark brown, fluorescent green, maroon, dark pink, skin, dark orange, light brown, yellow, dark green and black color respectively. (B) Shared binding modes of **MDA-6**, **MDA-11** and **MDA-13** are displayed in sky blue, gray and red color respectively. (C) Binding orientation of **MDA-7** (yellow) within MAO-B active site showing π – π (orange colored lines) and H-bond (green dashes) interactions. (D) Superimposed binding mode of **MDA-7** (yellow) within MAO-B originally docked with safinamide (dark green).

5.3.3.1.4.4. Binding mode of lead MAO-B inhibitor MDA-7

Examination of one of the best-ranked docking solution of lead MAO-B inhibitor **MDA-7** reveals that the entire molecule is stabilized in both the cavities with the rigid hydrophobic (methylenedioxy)phenyl moiety caged into the substrate cavity, while the arylidene ring is extended towards the entrance cavity of MAO-B. The compound is found to exhibit $\pi - \pi$ interactions between the phenyl ring present at the carbimino terminal of the semicarbazone scaffold and the phenyl ring of Tyr326 at an inter-plane distance of approximately 4.16 Å; and the benzene ring of (methylenedioxy)phenyl moiety with Tyr398 and Tyr435 at an inter-plane distance of approximately 4.19 Å and 4.18 Å respectively. In addition, H-bond interactions have been observed between oxygen of C=O in carbimino linker and H of OH of Tyr435; and H of NH in carbimino linker and oxygen of Ile198 at an inter-plane distance of 2.12 Å and 2.86 Å respectively (**Figure 5.28. (C)**). These interactions, as a whole, resulted in the firmness of the ligand within the MAO-B and hence confirm the stability of the complex. **Figure 5.28. (D)** shows the docked pose of **MDA-7** (yellow) within the active site of MAO-B superimposed with the docked pose of safinamide (orange) indicating that both share a similar binding orientation.

5.3.3.2. Acetylcholinesterase (AChE) enzyme inhibition studies

5.3.3.2.1. *In-vitro* AChE inhibition assay

Inhibitory activities of the target compounds against rat AChE was tested by the spectrophotometric method of Ellman *et al.* but with minor modifications using donepezil and tacrine as reference standards. The IC_{50} values for AChE inhibition are summarized in **Table 5.18.**

Table 5.18. *In-vitro* and computational AChE inhibition data for compounds **MDA-1** to **MDA-14**

Code	*In-vitro*	Computational	
	IC_{50} (µM) ± SEM	**ΔG (kcal mol^{-1})**	**K_i (µM)**
MDA-1	1176 ± 7.41	-6.38	21.06
MDA-2	14.0 ± 0.83	-6.35	22.09

MDA-3	70.06 ± 2.90	-5.77	59.21
MDA-4	114.5 ± 3.28	-5.62	76.28
MDA-5	0.037 ± 0.004	-7.46	3.39
MDA-6	26.51 ± 0.86	-6.23	27.32
MDA-7	0.0087 ± 0.0002	-6.56	15.47
MDA-8	2010 ± 6.57	-5.19	156.77
MDA-9	0.388 ± 0.002	-7.01	7.24
MDA-10	0.071 ± 0.001	-7.3	4.43
MDA-11	2.578 ± 0.061	-7.65	2.48
MDA-12	3.26 ± 0.087	-6.51	16.97
MDA-13	0.307 ± 0.003	-6.95	8.06
MDA-14	569.4 ± 3.92	-5.51	92.16
DNP	0.021 ± 0.005	-6.01	39.45
TRN	0.225 ± 0.04	-	-

Reference inhibitors: DNP – Donepezil, TRN – Tacrine.

Note: Each IC_{50} value is the mean ± SEM. It refers to the assay concentration of test compound which leads to 50% inhibition of enzyme activity. Level of statistical significance: $P < 0.05$ versus the corresponding IC_{50} values obtained against AChE; as determined by ANOVA/Dunnett's.

All the synthesized compounds (**MDA-1** to **MDA-14**) were found to show activity against AChE displaying inhibition abilities in nanomolar to micromolar range. Among them, **MDA-7** was obtained as the lead candidate showing highest inhibition with IC_{50} value of 0.0087 ± 0.0002 µM, which is ~2.4-fold more potent as compared to donepezil and ~26-fold more potent in comparison to tacrine; followed by **MDA-5** and **MDA-10** respectively with IC_{50} values of 0.037 ± 0.004 µM and 0.071 ± 0.001 µM exhibiting about ~6.1 fold and ~3.2 fold potency compared to tacrine. All these compounds (**MDA-5**, **MDA-7** and **MDA-10**) possessed one or more chloro substituent on the phenyl ring at the carbimino terminal of the semicarbazone template.

A careful insight and analysis of the data listed in **Table 5.18.** led to several eventual structure-activity relationships (SAR).

Structure-activity relationship (SAR)

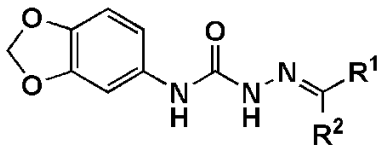

MDA-1 to MDA-11

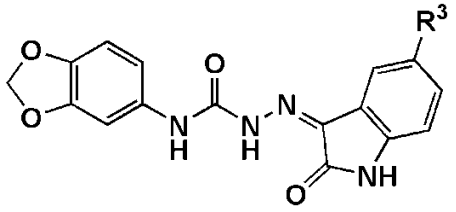

MDA-12 to MDA-14

- Substitution of the distal phenyl ring with –Cl group (**MDA-7**, **MDA-5**, **MDA-10**, **MDA-2** and **MDA-6**) increased the activity, while –F substitution decreased the activity (**MDA-3**).
- Substitution with –OH group further led to reduction in the activity (**MDA-4**).
- Substitution of carbimino terminal phenyl ring with bulky group like $–OCH_3$ group abolished the activity (**MDA-8**).
- Presence of diaryl substituents (**MDA-9**, **MDA-10** and **MDA-11**) at the carbimino terminal favored AChE activity. Interestingly, the activity increased 5.46 times due to the inclusion of chloro group (**MDA-10**); whereas the activity decreased 6.64 times due to dichloro substitution (**MDA-11**). This clearly indicates the requirement of "hydrophobic aryl binding moiety" with an optimum electronegativity (one –Cl substitution) at the carbimino terminal for effective AChE inhibition. This is also evidenced by the poor activity displayed by **MDA-1** and **MDA-2**.
- Among the compounds **MDA-12 to MDA-14**, 5-Cl substituted derivative (**MDA-13**) was found to be most potent followed by the unsubstituted derivative (**MDA-12**) while substitution with $–NO_2$ group reduced the activity (**MDA-14**).

5.3.3.2.2. Kinetic study of lead AChE inhibitor MDA-7

To gain further insight into the mechanism of action of this family of compounds on AChE, kinetic studies were carried out with the most promising compound **MDA-7**, using rat brain AChE. Graphical analysis of the reciprocal Lineweaver-Burk plots

(**Figure 5.29. (A)**) showed both increased slopes (decreased V_{max}) and intercepts (higher K_m) at increasing concentration of the inhibitor. This pattern indicates a mixed-type inhibition and therefore supports the dual site binding nature of this compound.

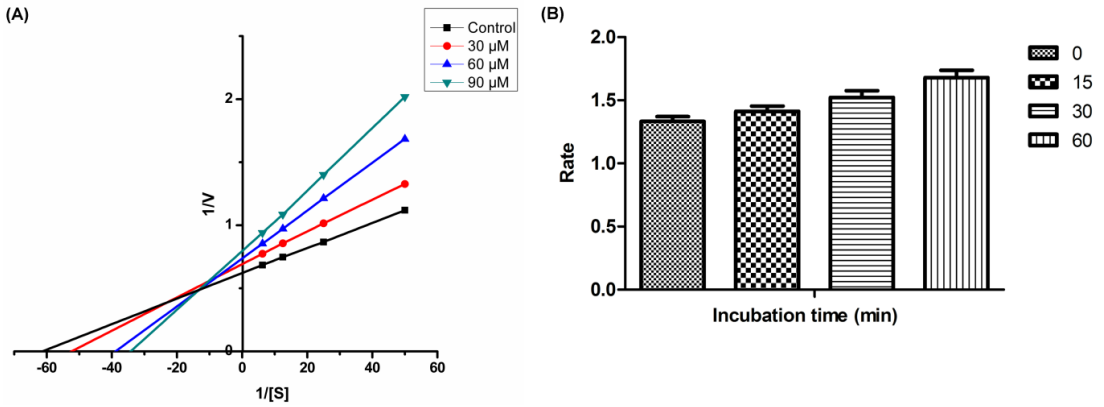

Figure 5.29. (A) Kinetics of rat brain AChE inhibition by compound **MDA-7**. Lineweaver-Burk plot of the rat brain AChE catalyzed oxidation of ATCI in the absence (control) and presence of various concentrations of compound **MDA-7** (30 µM, 60 µM, 90 µM). (B) Time-dependant inhibition of AChE catalyzed oxidation of ACTI by compound **MDA-7**. Rate data are expressed as nmol product formed/min/mg protein.

5.3.3.2.3. Reversibility experiment for lead AChE inhibitor MDA-7

Further, the most active AChE inhibitor, **MDA-7**, was subjected to time-dependent inhibition studies to investigate whether the observed enzyme inhibition is reversible or irreversible. As shown in **Figure 5.29. (B)**, there is no time-dependent reduction in the rates of AChE catalyzed oxidation of acetylthiocholine iodide (ACTI) when **MDA-7** was preincubated with the AChE for various periods of time i.e. 0, 15, 30, and 60 min (**Figure 5.28. (B)**). From this result it may be concluded that the inhibition of AChE is reversible, at least for the time period (60 min). An increase of AChE catalytic rates with increased preincubation time of **MDA-7** with the enzyme was observed.

5.3.3.2.4. Molecular docking studies of AChE inhibitors

To further investigate the binding orientation of inhibitors, molecular docking study was performed using AutoDock 4.2. The X-ray crystal structure of the recombinant human AChE (rhAChE) in complex with donepezil (PDB code: 4EY7) was obtained from the Protein Data Bank. The results of molecular docking studies for AChE is expressed in

terms of theoretical inhibition constants (K_i values) and estimated free energies of binding (ΔG) for each virtual enzyme-inhibitor complex and are shown in **Table 5.18.**

5.3.3.2.1.1. Pose analysis of AChE inhibitors

Examination of the computationally docked binding poses of all compounds within the AChE active site resulted in the following observations: All the test inhibitors were found to fit into the gorge of AChE formed by catalytic anionic site (CAS) and peripheral anionic site (PAS) and were enclosed by the residues Asp74, Trp86, Gly121, Gly122, Tyr124, Ser125, Gly126, Tyr133, Glu202, Ser203, Ala204, Trp236, Trp286, Phe295, Arg296, Phe297, Tyr337, Phe338, Tyr341, His447 (**Figure 5.30.**). Almost in all the test inhibitors the (methylenedioxy)phenyl moiety binds to peripheral anionic site (PAS) while the arylidene or diarylmethylene or isatin residue is flipped towards the catalytic anionic site (**Figure 5.30. (A)**). This reveals almost all the test inhibitors exhibit a similar binding orientation as the reference drug donepezil. However, a few exceptions are found with the **MDA-4**, **MDA-5**, **MDA-11** and **MDA-12** for which the orientation is completely the reverse (**Figure 5.30. (B)**). Further, these inhibitors are stabilized by hydrogen bonding (H-bond) and hydrophobic (π – π stacking) interactions.

All compounds showed one or more H-bond interactions. H-bond interaction with residue Asp74 is observed with **MDA-3**, **MDA-11**, **MDA-12** and **MDA-13**; likewise with Gly121, Gly122 and Ala204 in **MDA-5**; with Gly122 in **MDA-14**; with Tyr124 in **MDA-1**, **MDA-5**, **MDA-6**, **MDA-8**, **MDA-9**, **MDA-12** and **MDA-13**; with Ser125 in **MDA-13**; with Tyr133 in **MDA-12**; with Glu202 and Ser203 in **MDA-4**; with Trp286 in **MDA-10** and **MDA-14**; with Phe295 in **MDA-1**, **MDA-2**, **MDA-4**, **MDA-6**, **MDA-8**, **MDA-8**, **MDA-13** and **MDA-14**; with Arg296 in **MDA-1** and **MDA-7**; and with Tyr341 in **MDA-3**.

In addition, all the compounds showed π – π interactions except **MDA-10**. π – π interaction with residue Trp86 is observed with **MDA-2**, **MDA-3**, **MDA-4**, **MDA-6**, **MDA-11** and **MDA-13**; likewise with Trp286 in **MDA-9**; with Phe337 in **MDA-3** and **MDA-7**; with Phe338 in **MDA-11**; with Tyr341 in **MDA-1**, **MDA-2**, **MDA-5**, **MDA-6**, **MDA-12** and **MDA-13**; and with His447 in **MDA-4**. Moreover, π – cation interaction with His447 is found in **MDA-4**.

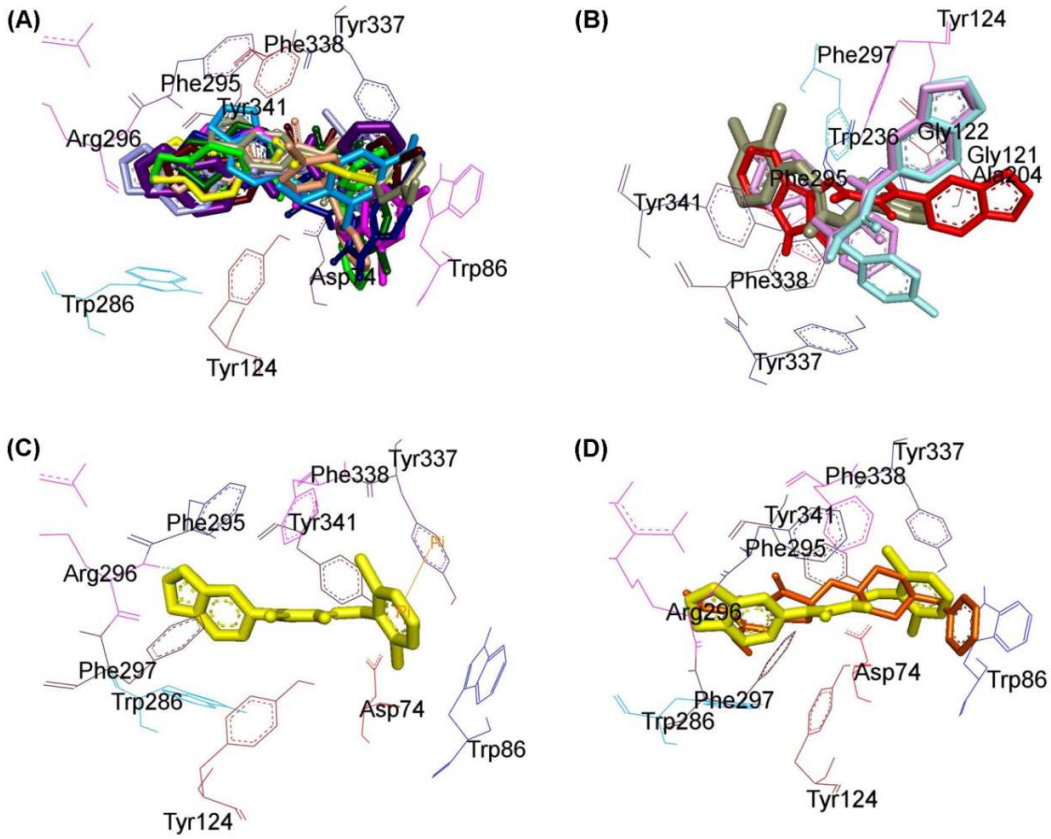

Figure 5.30. Structural screenshot of superimposed AChE inhibitors docked into the active site of AChE. Selected amino acids are displayed in black. (A) Shared binding mode of **MDA-1**, **MDA-2**, **MDA-3**, **MDA-6**, **MDA-7**, **MDA-8**, **MDA-9**, **MDA-10**, **MDA-13** and **MDA-14** displayed in dark violet, dark brown, dark green, dark pink, light violet, sky blue, fluorescent green, skin, dark blue and yellow color respectively. (B) Shared binding mode of **MDA-4**, **MDA-5**, **MDA-11** and **MDA-12** are displayed in light blue, gray, light pink and red color respectively. (C) Binding orientation of **MDA-7** (yellow) within AChE active site showing π – π (orange colored lines) and H-bond (green dashes) interactions. (D) Superimposed binding mode of **MDA-7** (yellow) in AChE originally docked with donepezil (orange).

5.3.3.2.1.2. Binding mode of lead AChE inhibitor MDA-7

Assessment of the virtual complex of the lead AChE inhibitor **MDA-7** and AChE (**Figure 5.30. (C)**) reveals that the (methylenedioxy)phenyl moiety was bound to the gorge forming the PAS while the arylidene ring occupies the CAS, whereas the linker was situated in the middle of the gorge between CAS and PAS. The phenyl ring at the carbimino terminal is involved in π – π interaction with Tyr337 at an inter-plane distance of approximately 3.91 Å. Besides this, the O atom of dioxole ring is bridged to H of NH_2

of Arg296 *via* H-bonding (**Figure 5.30. (C)**). Superimposition of rhAChE: **MDA-7** complex with the rhAChE:donepezil complex suggests that **MDA-7** mimics the binding mode of donepezil (**Figure 5.30. (D)**).

Comparison of the experimental and computational results indicated almost a good to better correlation between the *in-vitro* and computational data for MAO-A, MAO-B and AChE inhibition as observed from the above results.

5.3.3.3. Behavioural studies

5.3.3.3.1. Antidepressant activity (Forced swim test)

The synthesized compounds were evaluated for their antidepressant activity using Porsolt's forced swim test and the results are illustrated in **Figure 5.31.** The compounds **MDA-7** and **MDA-9** were found to be more active than the reference drug citalopram (CIT), thereby indicating that these compounds produce no CNS depression. Rest of the compounds was found to emerge as CNS depressants as they increased the immobility time.

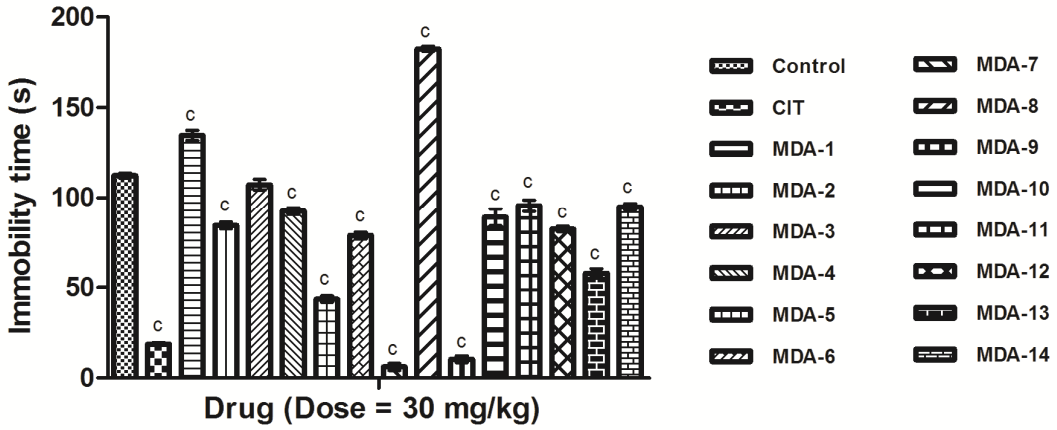

Figure 5.31. Antidepressant activity of 3,4-(methylenedioxy)aniline derived semicarbazones. The results are expressed as mean ± SEM (*n = 6*). The statistical significance was calculated by one-way ANOVA followed by Dunnett's test. CIT – Citalopram. $^{c}P < 0.001$ when compared with the control group.

5.3.3.3.2. Anxiolytic activity (Elevated plus maze test)

All the compounds were subjected to anxiolytic activity screening using elevated plus maze apparatus and the results are illustrated in **Figure 5.32.** Compounds **MDA-9,**

MDA-5, MDA-7, MDA-2, MDA-6 and MDA-13 possessed significantly greater anxiolytic activity than diazepam (DZM). Rest of the compounds was found to be less active than diazepam.

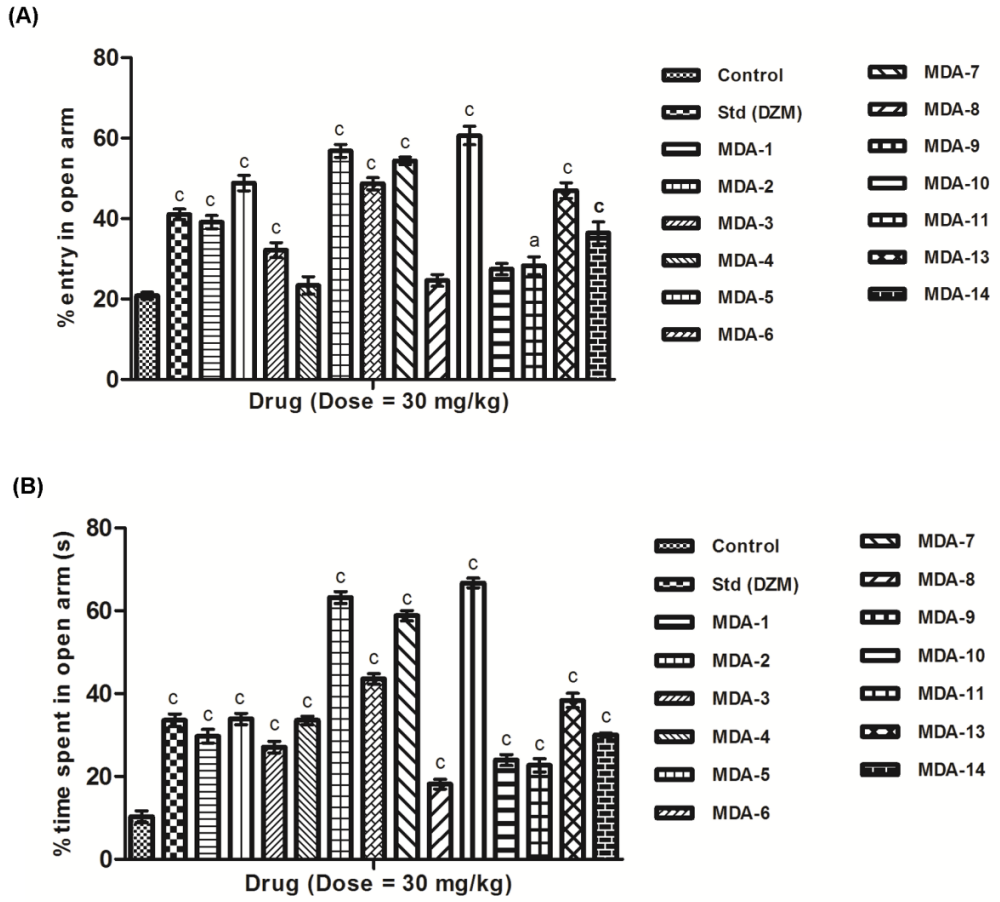

Figure 5.32. Anxiolytic activity of 3,4-(methylenedioxy)aniline derived semicarbazones. The results are expressed as mean ± SEM (*n = 6*). The statistical significance was calculated by one-way ANOVA followed by Dunnett's test. DZM – Diazepam. $^{c}P < 0.001$ when compared with control group.

5.3.3.3.3. Sedative-hypnotic activity (Pentobarbitone potentiation test)

All the synthesized compounds were evaluated in sedative and hypnotic test at a dose of 30 mg/kg and the results are illustrated in **Figure 5.33.** Most of the compounds showed significant variation from control. None of the compounds resulted in elongation of mean sleeping time than control confirming that these compounds do not potentiate narcosis. Instead, the compounds showed antagonistic properties to barbiturates indicating that they lack the sedative side effect.

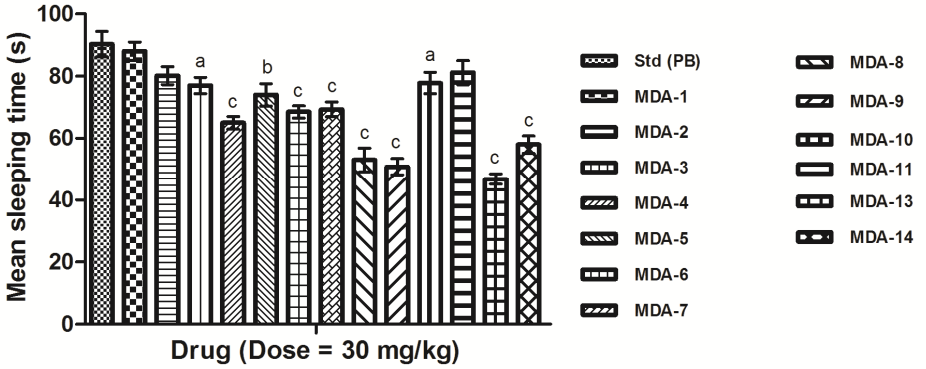

Figure 5.33. Sedative hypnotic activity of 3,4-(methylenedioxy)aniline derived semicarbazones. The results are expressed as mean ± SEM (*n = 6*). The statistical significance was calculated by one-way ANOVA followed by Dunnett's test. PB – Pentobarbitone, NT – Not tested. $^{a}P < 0.05$, $^{b}P < 0.01$, $^{c}P < 0.001$ when compared with control group.

5.3.3.4. Neurotoxicity screening (Rotarod test)

Selected compounds were screened for neurotoxicity by rotarod apparatus at a dose of 30 mg/kg at four time intervals viz. 0.5 h, 1 h, 2 h and 4 h. The results are presented in **Table 5.19.** All test compounds were found to be non-neurotoxic except compounds **MDA-12** and **MDA-14**. **MDA-12** was found to be moderately neurotoxic while compound **MDA-14** was found to be mildly neurotoxic compared to standard drug phenytoin.

Table 5.19. Neurotoxicity screening results of selected compounds of MDA series

Code	Neurotoxicity (Time in h)*			
	0.5	**1**	**2**	**4**
MDA-2	0/4	0/4	0/4	0/4
MDA-5	0/4	0/4	0/4	0/4
MDA-6	0/4	0/4	0/4	0/4
MDA-7	0/4	0/4	0/4	0/4
MDA-9	0/4	0/4	0/4	0/4

MDA-10	0/4	0/4	0/4	0/4
MDA-12	0/4	1/4	2/4	2/4
MDA-13	0/4	0/4	0/4	0/4
MDA-14	0/4	1/4	1/4	2/4
PHT	0/4	0/4	0/4	0/2

* The figures indicate the number of animals exhibiting toxicity/total number of animals tested. Reference drug: PHT – Phenytoin

5.3.3.5. Antioxidant activity (DPPH radical scavenging assay)

The antioxidant activity data of the selected test compounds is listed in **Table 5.20.** The DPPH· radical was scavenged by antioxidants *via* donation of hydrogen resulting in the formation of DPPH-H·. The colour of the DPPH changed from purple to yellow after reduction, which was quantified by the decline of absorbance at a wavelength of 517 nm. From the experimental results, the enhancement in the antioxidant activity was observed with most of the tested compounds. Among them, **MDA-5**, **MDA-6**, **MDA-7** and **MDA-9** showed better antioxidant activity than ascorbic acid (**Table 5.19.**).

Table 5.20. Antioxidant activity data of selected compounds of MDA series

Code	% Inhibition	Code	% Inhibition
MDA-2	47.72	**MDA-10**	60.60
MDA-5	62.59	**MDA-12**	52.39
MDA-6	63.27	**MDA-13**	58.09
MDA-7	65.98	**MDA-14**	32.99
MDA-9	64.37	**Ascorbic acid**	61.24

The statistical significance was calculated by one-way ANOVA followed by Dunnett's test. $P < 0.05$ when compared with control.

5.3.3.6. Liver toxicity studies

Enzyme estimation and histopathological studies of lead inhibitors **MDA-7** and **MDA-9** were done to check the magnitude of liver toxicity.

5.3.3.6.1. Assessment of liver function

Table 5.21. shows the liver function results with reference to most potent compounds **MDA-7** and **MDA-9**. The estimation revealed that there was no significant increase in SGOT, SGPT, alkaline phosphatase and decrease in protein level in serum as compared to the control level (**Table 5.21.**). The results clearly indicated that **MDA-7** and **MDA-9** showed no malfunctioning or toxicity of the liver as compared to control.

Table 5.21. Estimation of biochemical parameters of **MDA-7** and **MDA-9**

Code	SGOT[a] (U/L)	SGPT[b] (U/L)	ALP (U/L)	Albumin (g/dl)	Globulin (mg/dl)	Total protein (g/dl)
Range	25.8-80.8	17.5-90	62-190	3.3-4.8	1.5-3.5	5.2-7.6
MDA-7	49.23±3.58	85.53±3.24	128.1±2.95	3.83±0.18	3.26±0.23	7.2±0.21
MDA-9	59.83±2.44	76.27±4.51	108.73±4.18	3.83±0.22	3.17±0.26	5.86±0.46
Control	38.56±1.62	51.73±2.17	151.56±2.75	3.9±0.12	1.86±0.14	6.8±0.17

Results are expressed as Mean ± SEM. The mean level was calculated using ANOVA followed by Dunnett's test; [a]Serum glutamate oxaloacetate transaminase (SGOT); [b]Serum glutamate pyruvate transaminase (SGPT); [c]Serum alkaline phosphatase (ALP)

5.3.3.6.2. Liver histopathological studies

The Lucas technique was used to access the livers of rat, which was administered with test compounds at the dose level of 30 mg/kg body weight for 15 days and a comparison was done with the control group. Liver samples from control group and all the experimental groups **MDA-7** and **MDA-9** were within normal histopathological limits (**Figure 5.34.**).

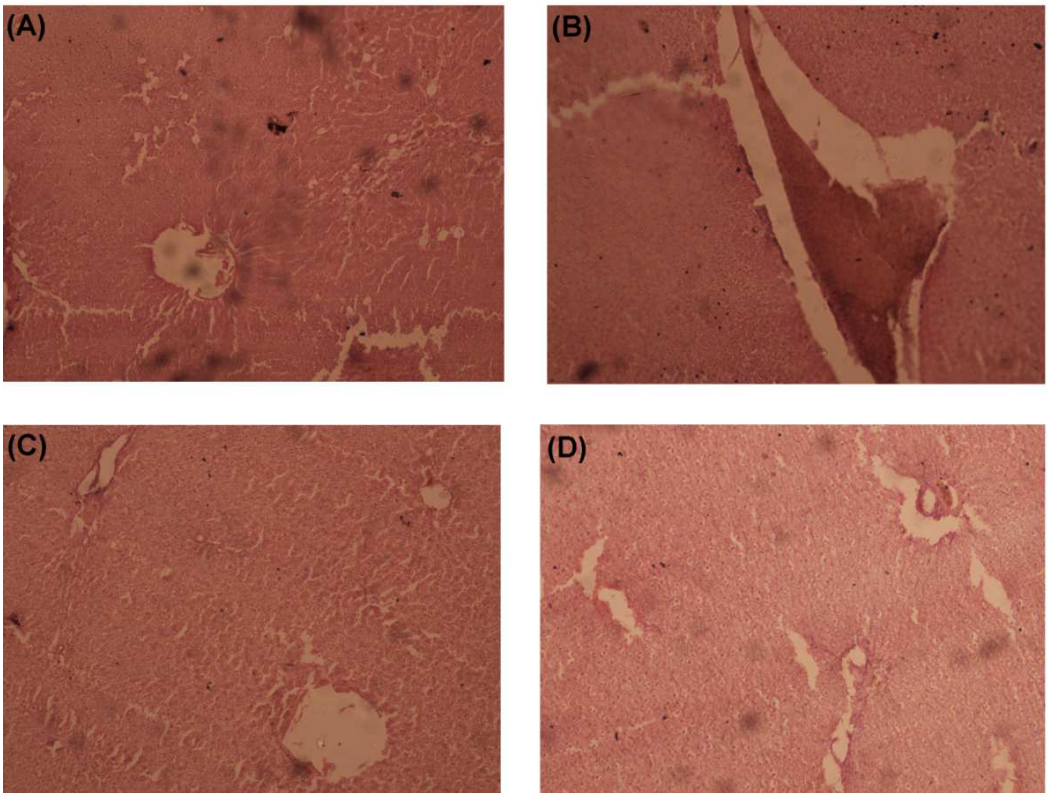

Figure 5.34. Microphotograph of the section of hematoxylin and eosin stained rat liver. Group: (A) Control (B) CCl_4-treated (C) **MDA-7** (D) **MDA-9**. Magnification: 10x.

5.3.4. *In-silico* molecular property analysis and ADMET prediction studies

All the structural elements were selected to check their adherence to Lipinski's rules for possible drug-likeness using molinspiration software (**Table 5.22.**).

The lipophilicity (expressed as MiLogP) predicted for all the compounds were found to be well the traditionally cut-off value of 5 used in drug design with the exception of compounds **MDA-10** and **MDA-11**, which violated the Lipinski's rules. All the structures reported herein show suitable MW values (MW < 500) necessary for a successful penetration to CNS. The topological polar surface area (TPSA) for all the compounds was observed to be in the range 71.96-150.64 $Å^2$ which is well below the limit of 160 $Å^2$. Thus, the predicted values for all compounds **MDA-1** to **MDA-14** fall into the appropriate range indicating good bioavailability of the drug molecule. The number of hydrogen bond acceptors (HBA) and donors (HBD) for all the compounds were in accordance with the Lipinski's rule of five with the exception of compound **MDA-14** in

which HBA was calculated to be 11. Thus it was predicted that almost all compounds are likely to be orally active.

Table 5.22. *In-silico* drug-likeness[a] prediction studies for **MDA-1** to **MDA-14**

Code	MW	MiLogP	TPSA	HBA	HBD	$n_{violations}$	Volume
Rule	<500	≤5	<160 Å^2	≤10	≤5	≤1	
MDA-1	297.31	3.22	71.96	6	2	0	262.99
MDA-2	331.76	3.90	71.96	6	2	0	276.53
MDA-3	315.30	3.38	71.96	6	2	0	267.92
MDA-4	299.29	2.82	92.19	7	3	0	254.45
MDA-5	352.18	4.56	71.96	6	2	0	273.50
MDA-6	352.18	4.59	71.96	6	2	0	273.50
MDA-7	352.18	4.56	71.96	6	2	0	273.50
MDA-8	343.34	3.35	90.42	8	2	0	297.52
MDA-9	359.38	4.44	71.96	6	2	0	317.84
MDA-10	393.83	5.11	71.96	6	2	1	331.38
MDA-11	428.27	5.79	71.96	6	2	1	344.91
MDA-12	324.30	2.54	104.82	8	3	0	266.97
MDA-13	358.74	3.19	104.82	8	3	0	280.51
MDA-14	369.29	2.47	150.64	11	3	1	290.31

[a]MW = Molecular weight, MiLogP = octanol-water partition coefficient, TPSA = Topological Polar Surface Area, HBA = Number of hydrogen bond acceptor, HBD = Number of hydrogen bond donor, $n_{violations}$ = violations from Lipinski's rule

The results of ADMET property calculation are listed in **Table 5.23.** and **Table 5.24.** respectively.

Human intestinal absorption (HIA) property is the determinant for those drugs that purport oral administration. All the compounds **MDA-1** to **MDA-14** expressed greater than 70% HIA values indicating good permeation across the membrane.

The *in-vitro* Caco-2 cell permeability is an important parameter to assess intestinal absorption of the drug since Caco-2 cells are derived from human colon adenocarcinoma, possessing transports *via* the intestinal epithelium. The results indicated that all compounds **MDA-1** to **MDA-14** exhibited moderate permeation.

The *in-vitro* MDCK cell permeability test utilizes canine kidney cells for the analysis of permeability. All the compounds **MDA-1** to **MDA-14** showed permeation less than 25 nm/s indicating low permeability.

The skin permeability is an important factor for the delivery of drug *via* transdermal administration. All the compounds **MDA-1** to **MDA-14** exhibited negative permeability values, indicating that transdermal mode of administration is not the suitable means to administer these drugs.

The percent of drug bound with plasma proteins was estimated and almost all the compounds (except **MDA-9** and **MDA-11**) were predicted to bind weakly to plasma proteins, thereby, indicating that the compounds will be available for diffusion or transport across cell membranes and hence finally interact with the target.

Table 5.23. *In-silico* ADME prediction data[a] of compounds **MDA-1** to **MDA-14**

Code	**Absorption**				**Distribution**	
	HIA (%)	***In-vitro* CP (nm/s)**	***In-vitro* MDCK (nm/s)**	***In-vitro* SP (log K_p, cm/h)**	***In-vitro* PPB (%)**	***In-vivo* BBB (C_{brain}/ C_{blood})**
Rule	0-20 (poor) 20-70 (moderate) 70-100 (well)	<4 (low) 4-70 (moderate) >70 (high)	<25 (low) 25-500 (moderate) >500 (high)		>90 (strongly bound) <90 (weakly bound)	>0.1 (CNS active) <0.1 (CNS inactive)
MDA-1	92.87	21.69	6.39	-3.62	78.09	0.32
MDA-2	93.84	21.71	0.25	-3.60	83.89	0.67

MDA-3	92.88	21.56	0.37	-3.85	80.49	0.37
MDA-4	88.07	20.02	5.09	-4.41	76.09	0.37
MDA-5	94.54	22.38	0.43	-3.51	88.81	1.57
MDA-6	94.54	21.30	0.13	-3.52	87.33	1.52
MDA-7	94.54	21.30	0.23	-3.49	89.59	1.56
MDA-8	93.32	24.03	4.51	-3.79	75.23	0.19
MDA-9	94.58	22.92	0.44	-2.78	91.39	1.02
MDA-10	95.31	23.68	0.11	-2.78	88.97	2.03
MDA-11	95.85	24.59	0.06	-2.72	93.52	3.48
MDA-12	91.14	20.19	6.04	-4.81	78.13	0.09
MDA-13	92.36	20.85	0.69	-4.77	89.43	0.13
MDA-14	74.26	18.12	4.10	-4.78	79.56	0.05

[a]HIA – Human Intestinal Absorption, CP – Caco2 cell permeability, MDCK – MDCK cell permeability, SP – skin permeability, PPB – Plasma protein binding, BBB – Blood brain barrier.

The blood-brain barrier (BBB) is a separation of circulating blood and cerebrospinal fluid in the CNS, and is responsible for limiting and regulating the exchange of substances between the CNS and blood. Predicting BBB penetration means predicting whether compounds pass across the blood-brain barrier. This is crucial in drug design since CNS active compounds must pass across it. According to the computed values; all the compounds except **MDA-12** and **MDA-14** were predicted to be CNS active and could be good candidates for CNS penetration.

The Ames test assesses mutagenicity of the compounds. All the compounds were predicted as mutagen. Besides, carcinogenicity test was performed to identify the tumerogenic potential of compounds in animals (mouse and rat). When analyzing carcinogenicity in mice, all the compounds were predicted as negative. By analyzing rat carcinogenicity, compounds **MDA-1**, **MDA-3**, **MDA-4**, **MDA-8**, **MDA-9**, **MDA-12** and **MDA-14** were predicted positive while rest of the compounds presented negative predictions. Human ether-a-go-go-related gene (hERG) encodes potassium channels,

which are responsible for normal repolarization of cardiac action potentials. Blockage or any other impairment of these channels in the heart can lead to fatal cardiac problems. Hence, drug-induced blockage of potassium channels has been a major concern. All the compounds presented medium risk except compound **MDA-10** which presented high risk while compound **MDA-9** presented ambiguous results against hERG inhibition.

Table 5.24. *In-silico* toxicity prediction data of compounds **MDA-1** to **MDA-14**

Code	Ames test	Carcinogenicity (Mouse)	Carcinogenicity (Rat)	hERG inhibition
MDA-1	Mutagen	Negative	Positive	Medium risk
MDA-2	Mutagen	Negative	Negative	Medium risk
MDA-3	Mutagen	Negative	Positive	Medium risk
MDA-4	Mutagen	Negative	Positive	Medium risk
MDA-5	Mutagen	Negative	Negative	Medium risk
MDA-6	Mutagen	Negative	Negative	Medium risk
MDA-7	Mutagen	Negative	Negative	Medium risk
MDA-8	Mutagen	Negative	Positive	Medium risk
MDA-9	Mutagen	Negative	Positive	Ambiguous
MDA-10	Mutagen	Negative	Negative	High risk
MDA-11	Mutagen	Negative	Negative	Medium risk
MDA-12	Mutagen	Negative	Positive	Medium risk
MDA-13	Mutagen	Negative	Negative	Medium risk
MDA-14	Mutagen	Negative	Positive	Medium risk

To sum up, despite other compounds exhibiting good brain penetration profiles, it can be concluded that **MDA-7** presents the best drug-like characteristics and ADMET properties among all the compounds of the series.

5.4. 3-HYDROXY-3-SUBSTITUTED OXINDOLE ANALOGUES OF ISATIN & ITS DERIVATIVES [HPO -1 to HPO-14]

5.4.1. Synthesis

3-Hydroxy-3-substituted oxindole analogues of isatin (**HPO-1** to **HPO-7** and **HPO-13**) and 5-bromoisatin (**HPO-8** to **HPO-12** and **HPO-14**) were obtained through Knoevenagel condensation of the appropriate isatin with acetone or substituted acetophenones or cyclohexanone in the presence of diethylamine as basic catalyst according to the reaction scheme depicted in **Scheme 4.7.** and **Scheme 4.8.** by optimizing the various reaction variables, viz. solvents, catalyst, temperature, stirring time, etc. The final compounds (**HPO-1** to **HPO-14**) were recrystallized using ethanol as a solvent.

All the final products were stable to open air environment. Considering the percentage yield of synthesized compounds, 3-hydroxy-3-substituted oxindole analogues of isatin (**HPO-1** to **HPO-7** and **HPO-13**) were obtained in moderate to moderate to good yields (20-90%) while 3-hydroxy-3-substituted oxindole analogues of 5-bromoisatin (**HPO-8** to **HPO-12** and **HPO-14**) were obtained in extremely low to moderate yields (10 to 60%).

All the products (**HPO-1** to **HPO-14**) were obtained as solid and in the powdered form. The final compounds were of orange (**HPO-1**, **HPO-2** and **HPO-6**), maroon (**HPO-3**, **HPO-7**, **HPO-8**, **HPO-13** and **HPO-14**) and red (**HPO-4**, **HPO-5 and HPO-9** to **HPO-12**) colour.

5.4.2. Characterization

5.4.2.1. Physicochemical characterization

5.4.2.1.1. Melting point

Melting points were determined in one end open capillary tubes on Sonar melting point apparatus and were uncorrected. All the synthesized compounds displayed a phase change from solid to liquid state and thus exhibited melting range between 2 to 5 °C indicating the purity of compounds. The observed melting point ranges for the synthesized compounds **HPO-1** to **HPO-14** are presented in the **Table 4.10.**

5.4.2.1.2. Solubility

The solubility of all the synthesized compounds was determined in various solvents at room temperature. All were insoluble in water and chloroform, partially soluble in

methanol but soluble in ethanol, DMSO and DMF. The observed solubility data are presented in **Table 4.10.**

5.4.2.1.3. Thin layer chromatography

Thin layer chromatography (TLC) was performed during the synthesis to monitor the progress of the reaction. A single distinct spot was observed which indicated the purity and confirmation of the product formation in each reaction, by comparing with the reactant spot as the R_f of the product which was different from that of the reactant. TLC was also performed for the final compounds (**HPO-1** to **HPO-14**) after purification to determine their R_f values. The observed R_f values are presented in the **Table 4.10.** Depending upon the polarity of compounds, eluents used for TLC analysis included (A) Chloroform: Methanol: Toluene – 7:1:2 (B) Chloroform: Methanol: Toluene – 7:2:1.

5.4.2.1.4. Determination of partition coefficient (LogP)

The synthesized compounds were found to exhibit experimental LogP values in the range 1.1 – 2.7 (shake flask method) indicating that they possess suitable lipophilicity necessary for their solubility in the lipid phase. The experimental (determined through shake flask method) and calculated LogP (software calculated) values are presented in **Table 4.10.**

5.4.2.2. Spectral characterization and elemental analysis

5.4.2.2.1. Ultraviolet (UV) spectroscopy

All the compounds showed prominent absorption with respect to the chromophore. The compounds of **HPO** series exhibited absorption bands due to C=O chromophores at λ_{max} 274-383 nm owing to $n \rightarrow \pi^*$ transition.

5.4.2.2.2. Infrared (IR) spectroscopy

The 3-hydroxy-3-substituted oxindole derivatives were confirmed by the presence of characteristic absorptions in the range **3300-3500 cm^{-1}**, 3150-3400 cm^{-1} and 1600-1700 cm^{-1} **for the O-H (str)**, N-H (str) and C=O (str) groups respectively. The presence of C=O (str) group of indole ring of isatin was confirmed by the characteristic absorption in the range 1680-1740 cm^{-1}. The presence of characteristic absorptions around 2890-3000 cm^{-1} confirmed the presence of CH_2 stretching while the presence of C=C (str) in the aromatic ring was confirmed by the characteristic absorptions in the range 1400-1620 cm^{-1}. The characteristic absorptions at 1523.82, 1344.43 (**HPO-6**) and at 1464.02, 1346.36 (**HPO-12**) confirms the presence of $–NO_2$ (str). The presence of halogens was

confirmed by the absorptions in the range 400-700 cm^{-1} for C-Br (**HPO-3**, **HPO-7**, **HPO-8** to **HPO-12** and **HPO-14**), 500-850 cm^{-1} for C-Cl (**HPO-4** and **HPO-9**) and 950-1100 cm^{-1} for C-F groups (**HPO-5** and **HPO-10**).

5.4.2.2.3. Nuclear magnetic resonance (NMR) spectroscopy

^{1}H NMR spectra of the 3-hydroxy-3-substituted oxindole derivatives showed a characteristic singlet at δ 4.04-5.12 ppm, δ 1.17-3.90 ppm and δ 2.76 ppm corresponding to hydroxyl (OH), methylene ($–CH_2–$) and methyl ($–CH_3$) (**HPO-1**) protons respectively. Oxindole protons and aromatic protons showed a singlet, doublet or doublet of doublets in the range δ 6.03-8.02 ppm and δ 6.85-7.98 ppm respectively. In ^{1}H NMR spectrum of 3-hydroxy-3-substituted oxindole derivatives having indolyl group, a singlet was observed at δ 7.12-8.33 ppm due to secondary amino (N–H) group of indole ring.

In ^{13}C NMR spectra, the appearance of signals in the range of δ 155.89-179.60 ppm confirmed the presence of oxindole carbonyl group and signals in the range δ 190.29-199.73 ppm confirmed the presence of aliphatic C=O (**HPO-1** to **HPO-12**) or cyclohexyl C=O group (**HPO-13** and **HPO-14**). Signals at δ 60.20-85.91 ppm (**HPO-1** to **HPO-14**), δ 45.18-64.29 ppm (**HPO-1** to **HPO-14**), δ 35.81 ppm (**HPO-1**) and δ 21.85-61.53 ppm (**HPO-13** and **HPO-14**) corresponded to oxindole hydroxyl (oxindole C-OH), methylene ($–CH_2–$), methyl ($–CH_3$) and cyclohexyl $–CH_2–$ respectively. The presence of oxindole C-H and aromatic C-H was confirmed by presence of peaks in the range δ 102.14-154.85 ppm and δ 111.16-166.73 ppm respectively.

5.4.2.2.4. Mass spectrometry

Compounds **HPO-4** and **HPO-9** were subjected to mass analysis. **HPO-4** (Mol. wt. = 301.72) showed an $[M+1]^+$ peak of 302.78 and a peak at 303.87 indicated the presence of Cl group thereby confirming the structure of the compound **HPO-4** (**Figure 4.79.**). Further, **HPO-9** (Mol. wt. = 380.62) showed an $[M+1]^+$ peak of 381.88 and peaks at 382.78 and 383.57 indicated the presence of Cl and Br group thereby confirming the structure of the compound **HPO-9** (**Figure 4.87.**).

5.4.2.2.5. Elemental analysis

All the compounds **HPO-1** to **HPO-14** were subjected to elemental analysis and the observed values were within ± 0.4% of the calculated values.

5.4.2.2.6. Powder X-ray diffraction analysis

Compound **HPO-4** was subjected to the powder X-ray diffraction analysis to confirm the crystallinity of the compound. The diffraction pattern of **HPO-4** (**Figure 4.80.**) showed sharp peaks indicating the crystalline nature of the compound.

5.4.3. Biological evaluation

5.4.3.1. MAO enzyme inhibition studies

5.4.3.1.1. *In-vitro* MAO inhibition assay

MAO-A and MAO-B inhibitory activities of test compounds **HPO-1** to **HPO-14** expressed in terms of IC_{50} values are reported in **Table 5.25**. The inhibitory activity of test compounds was measured *in-vitro* through a spectrophotometric method, by using crude rat brain mitochondrial suspensions as reported. For comparison, the inhibitory potencies of reference inhibitors isatin (**ISN**), clorgyline (**CLG**), harmine (**HRM**), selegiline (**SEL**) and rasagiline (**RAS**) are also presented in the **Table 5.25.**

Table 5.25. *In-vitro* and computational MAO inhibition data for **HPO-1** to **HPO-14**

Code	MAO-A			MAO-B			Expt. SI[a]
	In-vitro	Computational		*In-vitro*	Computational		
	IC_{50} (µM) ± SEM	ΔG*	K_i (µM)	IC_{50} (µM) ± SEM	ΔG*	K_i (µM)	
HPO-1	18.75 ± 1.319	-4.1	986.24	34.9 ± 2.181	-5.4	110.05	1.86
HPO-2	1.057 ± 0.019	-4.95	235.65	5.654 ± 0.043	-6.21	28.28	5.35
HPO-3	0.265 ± 0.003	-6.31	23.51	0.391 ± 0.005	-7.08	6.47	1.48
HPO-4	0.738 ± 0.008	-5.63	74.05	0.787 ± 0.013	-6.93	8.26	1.07
HPO-5	0.911 ± 0.006	-5.57	82.75	3.615 ± 0.052	-6.6	14.49	3.97
HPO-6	4.921 ± 0.143	-6.36	21.91	6.741 ± 0.211	-6.6	14.58	1.37
HPO-7	0.092 ± 0.002	-6.43	19.41	0.192 ± 0.006	-7.67	2.38	2.09
HPO-8	0.301 ± 0.012	-6.14	31.57	0.342 ± 0.008	-7.27	4.69	1.14
HPO-9	0.071 ± 0.003	-6.49	17.36	0.235 ± 0.003	-7.33	4.27	3.31

HPO-10	0.681 ± 0.007	-5.86	50.62	0.925 ± 0.017	-6.89	8.86	1.36
HPO-11	0.591 ± 0.002	-6.06	35.85	1.326 ± 0.029	-6.81	10.18	2.24
HPO-12	0.148 ± 0.004	-6.31	23.66	0.513 ± 0.016	-7.04	6.92	3.47
HPO-13	1.075 ± 0.041	-5.05	197.62	0.732 ± 0.012	-6.96	7.92	0.68
HPO-14	1.478 ± 0.092	-5.24	143.35	4.874 ± 1.315	-6.33	22.74	3.29
ISN	31.8 ± 4.50	-	-	12.4 ± 0.693	-4.74	333.71	-
CLG	0.00042	-	-	0.26	-	-	-
HRM	3.00	-5.3	130.82	7000	-	-	-
SEL	67.25 ± 1.02	-	-	0.019 ± 0.0008	-	-	-
RAS	0.412 ± 0.123	-	-	0.004 ± 0.0009	-6.51	16.8	-

ΔG values are expressed in $kcalmol^{-1}$; [a]The selectivity index is the selectivity for the MAO-A isoform and is given as the ratio of experimental IC_{50}(MAO-B)/IC_{50}(MAO-A); Reference inhibitors: ISN – Isatin, CLG – Clorgyline, HRM – Harmine, SEL – Selegiline, RAS – Rasagiline

NOTE: Each IC_{50} value is the mean ± SEM. It refers to the assay concentration of test compound which leads to 50% inhibition of enzyme activity. Level of statistical significance: $P < 0.05$ versus the corresponding IC_{50} values obtained against MAO-A and MAO-B, as determined by ANOVA/Dunnett's.

The test compounds exhibited significant MAO inhibitory activity with the IC_{50} values at micromolar (µM) to submicromolar range. The IC_{50} values are in the range of 0.071 ± 0.003 µM (**HPO-9**) to 18.757 ± 1.319 µM (**HPO-1**) for MAO-A and 0.192 ± 0.006 µM (**HPO-7**) to 34.9 ± 2.181 µM (**HPO-1**) for MAO-B. Also noteworthy is the observation that all the compounds displayed mild to moderate selectivity for the MAO-A isoform over MAO-B (**Table 5.25.**).

To gain more insights into the SARs, focused structural modifications were attempted on the isatin scaffold to vary the lipophilic, electronic and steric properties. In general, all structural variations attempted in the scaffold resulted in improved inhibitory activity. Particularly, the enhancement of lipophilicity of compounds by incorporating bromo group at position 5 and chloro aryl or dibromo aryl substitution at position 3 of isatin scaffold has resulted in improved inhibitory activity against MAO isozymes.

5-bromo-3-hydroxy-3-(4'-chlorophenacyl)oxindole (**HPO-9**, IC_{50} = 0.071 ± 0.003 µM) emerged as the most active inhibitor examined towards MAO-A. Whereas the most active MAO-B inhibitor, 3-hydroxy-3-(2',4'-dibromophenacyl)oxindole (**HPO-7**), was found to exhibit an IC_{50} value of 0.192 ± 0.006 µM.

Structure-activity relationship (SAR)

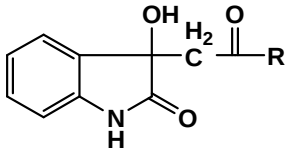

(HPO-1 to HPO-7)

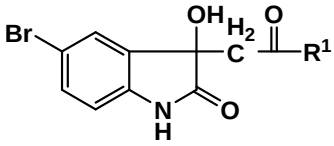

(HPO-8 to HPO-12)

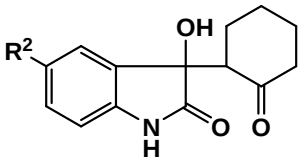

(HPO-13 and HPO-14)

- The alterations in the electronic and steric features afforded by the presence of various mono- (**HPO-3** to **HPO-6**, **HPO-8** to **HPO-12**) or disubstituted phenyl ring (**HPO-7**) or cyclohexanone ring (**HPO-13** to **HPO-14**) at C3 significantly influenced the MAO inhibitory profile of these compounds.
- Interestingly, the 4-chloro-substituted analogue (**HPO-9**) was found to be the most potent MAO-A inhibitor among the other analogues with the selectivity index of 3.31. This potential activity and selectivity can be attributed to the presence of 4-chloro substitution on the phenacyl side chain.
- However, bromo (**HPO-7**, **HPO-12** and **HPO-3** which are 1.3, 2.08 and 3.73 times less potent respectively than **HPO-9**) and fluoro (**HPO-10** and **HPO-5**, almost 10 and 13 times less potent than **HPO-9**) substitutions on the phenacyl side chain resulted in reduction in the inhibitory potency against MAO-A which may be because of the variation in the electronic property imparted by these groups.
- Moreover, nitro (**HPO-6**) substitution on the phenacyl side chain resulted in decrease in the inhibitory potency against MAO-A.
- However, introduction of bromo group at position 5 of isatin ring along with the presence of nitro on the phenacyl side chain (**HPO-12**) increased the potency towards MAO-A.
- In contrast to its effect on the MAO-A inhibition potency, the presence of methyl group on the phenacyl side chain (**HPO-1**) did not exhibit pronounced

enhancement in MAO-B inhibition potency. **HPO-7**, 3-hydroxy-3-(2',4'-dibromophenacyl)oxindole only moderately inhibited MAO-B with an IC_{50} value of 0.192 µM, approximately 10-fold less potent than the inhibition potency of selegiline.

- Introduction of unsubstituted cyclohexanone ring at position 3 (**HPO-13**) lead to increased potency towards MAO-B while incorporation of bromo group at position 5 in addition to cyclohexanone ring on isatin moiety (**HPO-14**) increased the potency towards MAO-B.
- Thus, substitution with functionalized groups like hydroxyl, bromo, chloro and fluoro on the C3 phenacyl ring in addition to bromo group at position 5 of isatin moiety increased the potency towards MAO-A.
- MAO inhibition results also indicated the crucial role of the rigid -CH_2-CO- linker on the potent MAO-A inhibitory activity.

These results guided us towards the influence of the steric groups and electronic substituents on the MAO inhibitory profile.

5.4.3.1.2. Kinetic studies of lead MAO inhibitors

To further examine the modes of MAO-A and MAO-B inhibition, sets of Lineweaver-Burk plots were constructed for the inhibition of MAO-A enzyme by **HPO-9** and MAO-B by **HPO-7**, the selected representative MAO-A and MAO-B inhibitors respectively (**Figure 5.35.**). Inspection of Lineweaver-Burk plots suggested that **HPO-9** and **HPO-7** inhibited respectively MAO-A and MAO-B competitively since the plots are linear and intersect at the Y-axis.

5.4.3.1.2.1. Determination of K_i for lead MAO inhibitors (HPO-9 and HPO-7)

For each type of mode of inhibition, the dissociation constant (K_i) can be calculated for the inhibitor that reflects the strength of interactions between the enzyme and the inhibitor. K_i for the lead inhibitors (**HPO-9** and **HPO-7**) was calculated using the GraphPad Prism resulting in the K_i value of 7.802 ± 0.005 nM for **HPO-9** against MAO-A and 18.952 ± 0.015 nM for **HPO-7** against MAO-B. Comparison of the IC_{50} values with the K_i values reflects tight binding of these inhibitors to the enzyme.

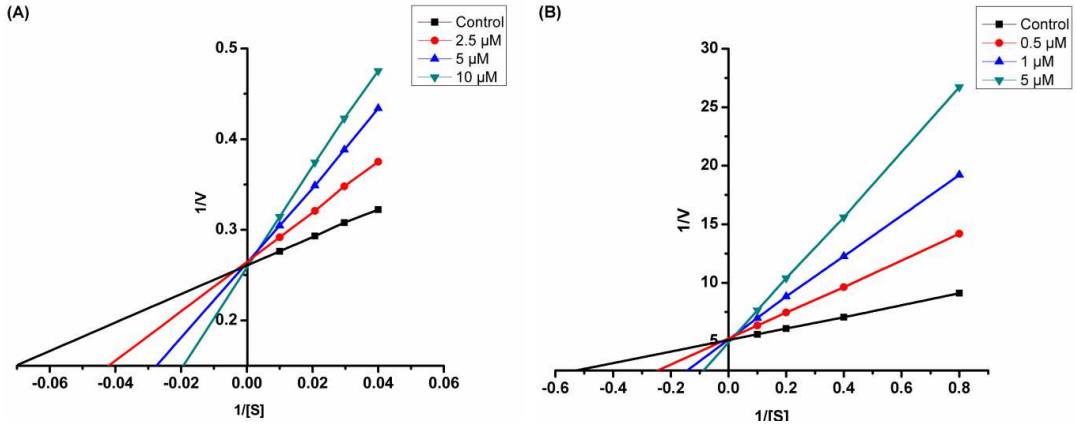

Figure 5.35. Kinetics of rat brain MAO-A inhibition by **HPO-9** and MAO-B inhibition by **HPO-7**. (A) Lineweaver-Burk plot of the rat brain MAO-A catalyzed oxidation of serotonin in the absence (control) and presence of various concentrations of **HPO-9** (2.5 µM, 5 µM, 10 µM). (B) Lireweaver-Burk plot of the rat brain MAO-B catalyzed oxidation of benzylamine in the absence (control) and presence of various concentrations of **HPO-7** (0.5 µM, 1 µM, 5 µM). The rates (V) are expressed as nmol product formed/min/mg protein.

5.4.3.1.3. Reversibility and irreversibility experiments

Further **HPO-9**, the most active MAO-A inhibitor and **HPO-7**, the most active MAO-B inhibitor was subjected to time-dependent inhibition studies to investigate whether the observed enzyme inhibition is reversible or irreversible.

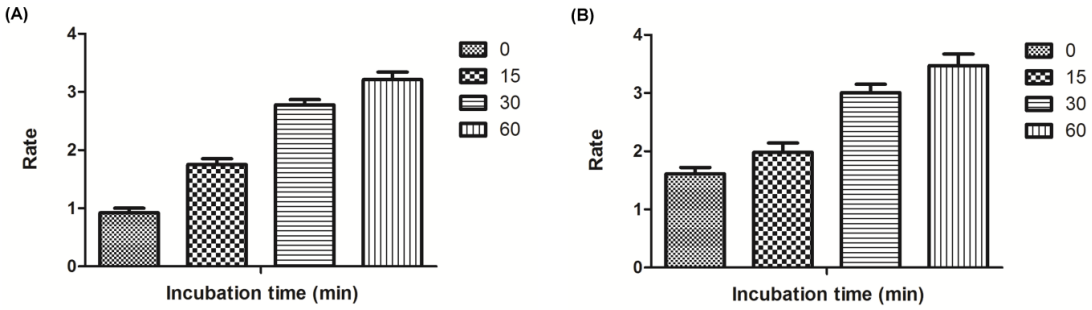

Figure 5.36. Time-dependant inhibition of (A) MAO-A catalyzed oxidation of serotonin by compound **HPO-9** (B) MAO-B catalyzed oxidation of benzylamine by compound **HPO-7**. Rate data are expressed as nmol product formed/min/mg protein.

Reversibility test was determined using the slightly modified method described by Legoabe *et al*. As shown in **Figure 5.36.**, there is no time-dependent reduction in the rates of MAO-A catalyzed oxidation of serotonin and MAO-B catalyzed oxidation of

benzylamine when **HPO-9** and **HPO-7** were preincubated with MAO-A and MAO-B enzyme respectively for various periods of time i.e. 0, 15, 30, and 60 min. From this result it may be concluded that the inhibition of both MAO-A and MAO-B is reversible, at least for the time period (60 min). Interestingly, marked increase of MAO-A and MAO-B catalytic rate with increased preincubation time of **HPO-9** and **HPO-7** with the respective enzymes was observed.

5.4.3.1.4. Molecular modeling studies

Molecular docking studies were carried out to shed some light on the peculiar binding modes and interactions of MAO inhibitors into the MAO isozymes in addition to affinity and selectivity.

All the experimentally tested inhibitors (**HPO-1 to HPO-14**) were docked successfully into the catalytic site of MAO-A and MAO-B isozymes using the automated docking program AutoDock 4.2 as per the protocol. The best scoring conformers from the largest cluster were considered for further structural and interaction studies. The results of the molecular docking studies for both MAO-A and MAO-B expressed in terms of theoretical inhibition constants (K_i values) and estimated binding energies (ΔG) for each virtual enzyme – inhibitor complex are given in **Table 5.25.** Visual inspection of binding modes of all inhibitors within the active site of MAO-A and MAO-B was done to gain more insight on the binding orientation and possible inhibitor-enzyme interactions.

5.4.3.1.4.1. Pose analysis of MAO-A inhibitors

The inhibitor binding site of MAO-A represented a single cavity extending from the flavin ring to the cavity-shaping loop. The volume of this cavity was estimated to be ~ 500 cm^3 and is quite hydrophobic. All the inhibitors were found to be located in the active center cavity of the MAO-A. Compounds **HPO-2**, **HPO-3**, **HPO-4**, **HPO-5**, **HPO-6**, **HPO-7**, **HPO-9**, **HPO-12** and **HPO-14**; and **HPO-1**, **HPO-8**, **HPO-10**, **HPO-11** and **HPO-13** (**Figure 5.37.**) shared a common binding mode within the active site cavity of MAO-A.

Further investigation of interactions of all inhibitors (**HPO-1** to **HPO-14**) with the anchoring amino acid residues present in the active site of MAO-A lead to the following observations. The potential binding sites of these inhibitors was found to be surrounded by the residues Tyr69, Ile180, Asn181, Phe208, Val210, Gln215, Cys323, Ile325, Ile335,

Met350, Phe352, Tyr407, Tyr444 and FAD (**Figure 5.37.)** which was very much similar to the binding sites of reference MAO-A inhibitor, harmine.

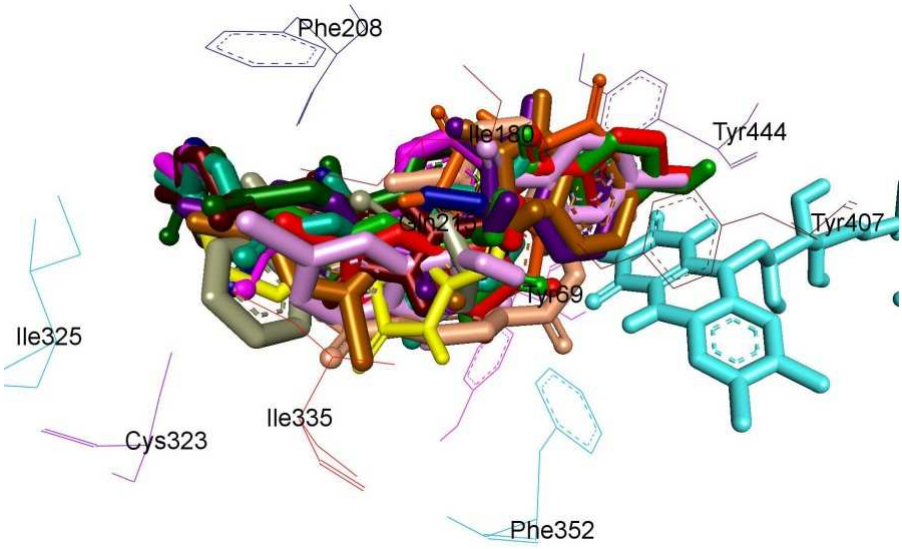

Figure 5.37. Structural screenshot of superimposed MAO-A inhibitors docked into the active site of MAO-A. FAD is displayed in cyanin. Selected amino acids are depicted in black. **HPO-1**, **HPO-2**, **HPO-3**, **HPO-4**, **HPO-5**, **HPO-6**, **HPO-7**, **HPO-8**, **HPO-9**, **HPO-10**, **HPO-11**, **HPO-12**, **HPO-13** and **HPO-14** are displayed in dark orange, dark blue, dark brown, dark violet, dark pink, dark green, light brown, light pink, peacock green, red, parrot green, skin, gray and yellow color respectively.

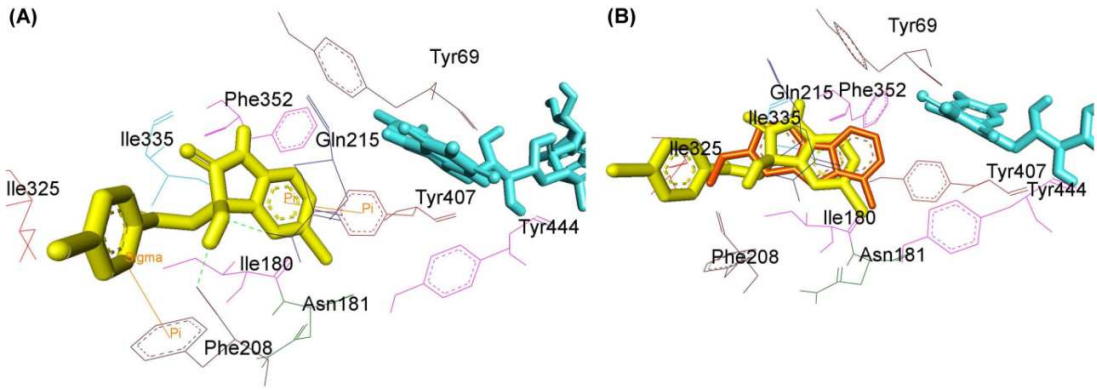

Figure 5.38. Structural screenshot of superimposed MAO-A inhibitors docked into the active site of MAO-A. FAD is displayed in cyanin. Selected amino acids are displayed in black. (A) Binding orientation of **HPO-9** (yellow) within MAO-A active site showing π – π (orange colored lines) and H-bond (green dashes) interactions. (B) Superimposed binding mode of **HPO-9** (yellow) within MAO-A originally docked with harmine (orange).

Almost in all compounds the oxindole moiety occupied the cavity extending towards FAD while the substituted phenacyl group occupies the opening of the cavity (**Figure 5.37.**). At the bottom of the cavity, Tyr444, FAD and Tyr407 formed an aromatic cage which decided the final orientation of the inhibitors and hence their stabilization and activity. This proved that the effective complimentary binding sites for MAO-A were present in the 3-hydroxy-3-substituted oxindole analogues. Further, these inhibitors were stabilized by π – π stacking and hydrogen bonding (H-bond) interactions.

HPO-1, **HPO-4**, **HPO-7, HPO-8, HPO-9, HPO-10** and **HPO-11** showed π – π interactions. π – π interaction with residue Tyr407 was observed with **HPO-4**, **HPO-7**, **HPO-8**, **HPO-9**, **HPO-10**, **HPO-11** and **HPO-12**; likewise with **Tyr444** in compounds **HPO-8**, **HPO-10** and **HPO-11**. Besides, **HPO-1** was stabilized by π – σ interaction with Tyr444; **HPO-9** with Phe208; and **HPO-10** with FAD respectively. All compounds showed one or more H-bond interactions except **HPO-8**. Thus, in most of the potent compounds, preferably π – π, π – σ and hydrogen bonding interactions were found to be responsible for mediating the inhibitory activity against MAO-A isozyme.

5.4.3.1.4.2. Binding mode of lead MAO-A inhibitor HPO-9

Examination of one of the best-ranked docking solution of lead MAO-A inhibitor **HPO-9** (**Figure 5.38. (A)**) revealed that oxindole nucleus is located towards the opening of MAO-A receptor while the phenacyl side chain extends towards the FAD. From the molecular modeling study, it was depicted that **HPO-9** has good access into deep inside the cavity of MAO-A. Entire molecule seems to be entrapped by the amino acid residues Tyr69, Asn181, Phe208, Ile325, Ile335, Phe352, Tyr407, Tyr444 and FAD. The benzene ring of oxindole was observed to possess π – π interaction with the phenyl ring of Tyr407 at an inter-plane distance of 6.18 Å. Additionally, the C-2 of the phenyl ring at phenacyl side chain exhibited π – σ interaction with Phe208 at an inter-plane distance of 3.93 Å. Besides this, the molecule was found to be stabilized by several H-bond interactions also. Hydrogen of 3-OH group on the oxindole ring was involved in H-bond interactions with oxygen of C=O of Phe208 at an inter-plane distance of 2.24 Å. Moreover oxygen of 3-OH group on the oxindole ring also stabilized the molecule by forming H-bond interactions with hydrogen of NH_2 of Gln215 at an inter-plane distance of 2.14 Å. These interactions, as a whole, resulted in the firmness of the ligand in the active site cavity of MAO-A and hence proved the greater stability of the complex. The docked pose of

HPO-9 in the MAO-A cavity superimposed with docked pose of harmine (yellow) showed that both share a similar binding orientation (**Figure 5.38. (B)**) which further strengthened our findings.

5.4.3.1.4.3. Pose analysis of MAO-B inhibitors

In contrast to MAO-A, the active site of MAO-B consisted of two cavities, a 420 $Å^3$ hydrophobic substrate cavity interconnected to an entrance cavity of 290 $Å^3$. **HPO-2**, **HPO-3**, **HPO-4**, **HPO-5**, **HPO-6**, **HPO-7**, **HPO-9**, **HPO-10, HPO-11, HPO-12** and **HPO-14** and **HPO-1**, **HPO-8** and **HPO-13** (**Figure 5.39.)** shared a common binding mode within the active site cavity of MAO-B.

Almost all the inhibitors were situated in the active centre cavity of MAO-B. The inhibitors (**HPO-1** to **HPO-14**) were found to be embedded in the space surrounded by the residues Leu171, Cys172, and Tyr398 on one side and by Ile198, Ile199, and Tyr435 on the other side in addition to the aromatic residues Tyr60, Tyr326 and Phe343. Visual inspection revealed that the binding sites of the inhibitors (**HPO-1** to **HPO-14**) were almost similar to the binding sites of standard MAO-B inhibitor, rasagiline. Further, $\pi - \pi$ stacking and hydrogen bonding (H-bond) interactions imparted stability to these inhibitors.

All compounds showed $\pi - \pi$ interactions except **HPO-1**, **HPO-2**, **HPO-6**, **HPO-11**, **HPO-12** and **HPO-14**. $\pi - \pi$ interactions with residue Tyr398 was observed in compounds **HPO-3**, **HPO-4**, **HPO-5**, **HPO-7**, **HPO-8**, **HPO-9** and **HPO-10**. Moreover, **HPO-13** showed $\pi - \pi$ interactions with Phe343; likewise **HPO-3**, **HPO-4**, **HPO-5**, **HPO-7** and **HPO-10** with Tyr435. **HPO-9** was stabilized by $\pi - \sigma$ interaction with Tyr326; **HPO-4** and **HPO-8** with FAD; and **HPO-8** with Ile199. Besides, all compounds showed H-bond interactions. H-bond interactions were observed with Tyr435 in **HPO-9**; with FAD in **HPO-11**, **HPO-12** and **HPO-13**; with Tyr326 in **HPO-1** and **HPO-2**; with Pro102 in **HPO-1** and **HPO-2**; with Cys172 in **HPO-3**, **HPO-4**, **HPO-7 and HPO-11**; with Gln206 in **HPO-3**, **HPO-4**, **HPO-7**, **HPO-11 and HPO-8**; with Ile198 in **HPO-3**, **HPO-4**, **HPO-7**, **HPO-10**, **HPO-11** and **HPO-12**; with Tyr188 in **HPO-5**; with Tyr398 in **HPO-5**, **HPO-10** and **HPO-14**; with Leu171 in **HPO-5**, **HPO-6**, **HPO-13 and HPO-14**; and with Phe168 in **HPO-12**.

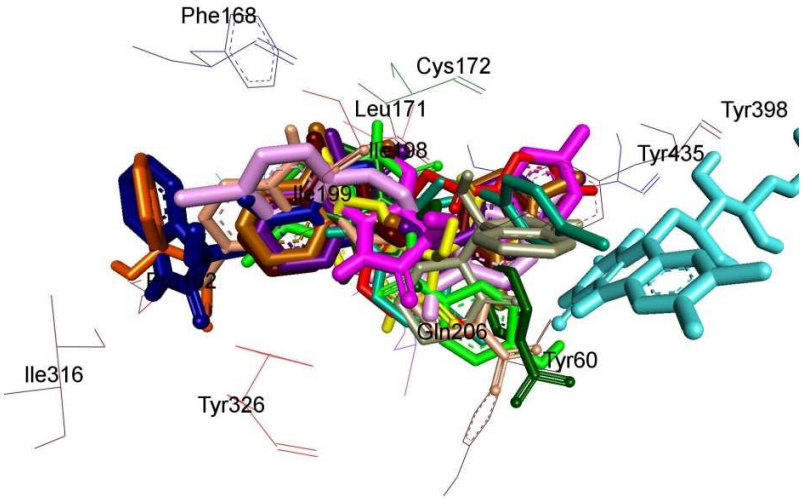

Figure 5.39. Structural screenshot of superimposed MAO-B inhibitors docked into the active site of MAO-B. FAD is displayed in cyanin. Selected amino acids are depicted in black. **HPO-1**, **HPO-2**, **HPO-3**, **HPO-4**, **HPO-5**, **HPO-6**, **HPO-7**, **HPO-8**, **HPO-9**, **HPO-10**, **HPO-11**, **HPO-12**, **HPO-13** and **HPO-14** are displayed in dark orange, dark blue, dark brown, dark violet, dark pink, dark green, light brown, light pink, peacock green, red, parrot green, skin, gray and yellow color respectively.

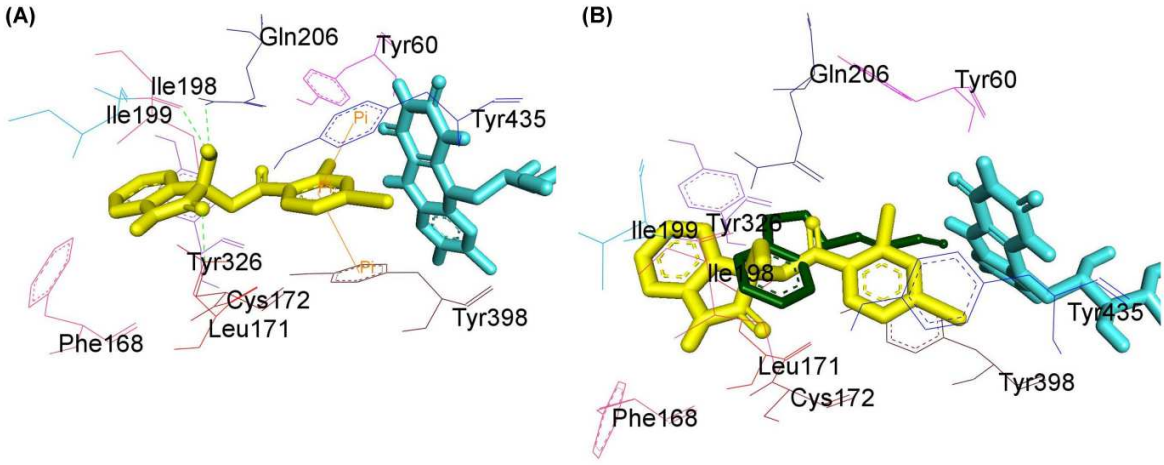

Figure 5.40. Structural screenshot of superimposed MAO-B inhibitors docked into the active site of MAO-B. FAD is displayed in cyanin. Selected amino acids are displayed in black. (A) Binding orientation of **HPO-7** (yellow) within MAO-B active site showing π – π interactions (orange colored lines). (B) Superimposed binding mode of **HPO-7** (yellow) in MAO-B originally docked with rasagiline (dark green).

Thus, in most of the potent compounds, preferably π – π and H-bond interactions were to be responsible for mediating the inhibitory activity against MAO-B enzyme. Good van der Waals and electrostatic interactions were also observed for all the docked molecules.

5.4.3.1.4.4. Binding mode of lead MAO-B inhibitor HPO-7

Inspection of the virtual complex between the lead MAO-B inhibitor **HPO-7** and MAO-B revealed that, in the substrate cavity, the oxindole ring was oriented towards the entrance cavity and the 3-phenacyl side chain pointed out towards the flavin cofactor (**Figure 5.40. (A)**). This suggested that the whole molecule traverses both cavities. The entire molecule was stabilized in both the cavities surrounded by the residues Leu171, Cys172, Ile198, Ile199 and Tyr326 towards the entrance cavity space and residues Tyr60, Tyr398 and Tyr435 framed the aromatic cage in the substrate cavity. The binding was further stabilized by various π – π interactions. π – π interaction was observed between the aromatic ring at phenacyl side chain and the amino acid residues Tyr398 and Tyr435 respectively at an inter-plane distance of approximately 4.03 Å and 4.54 Å. Moreover, H-bond interactions were observed between oxygen of 3-OH of phenacyl side chain and H of NH_2 of Gln206; and between H of 3-OH of phenacyl side chain and O of C=O of Ile198. Also, oxygen of 2C=O of isatin was also H-bonded to H of SH of Cys172. Thus, H-bond and π – π interactions were found to be involved in displaying the overall activity towards MAO-B. The docked pose of **HPO-7** in the MAO-A cavity superimposed with docked pose of rasagiline (dark green) showed that both share a similar binding orientation (**Figure 5.40. (B)**) which further strengthened our findings.

Overall analysis of interactions of all inhibitors (**HPO-1** to **HPO-14**) with the anchoring amino acid residues present in the active site of MAO-B lead to the following observations. (i) H-bond and π – π interactions were found to play an important role in mediating activity against MAO-B. (ii) In addition to the oxindole skeleton, another hydrophobic aryl ring with electronegative substituents such as bromo, chloro and fluoro groups is crucial for their effective binding and stabilization in the active site cavity of MAO-B.

Thus, a good correlation between the *in-vitro* and computational data was observed for both MAO-A and MAO-B inhibition.

5.4.3.2. Acetylcholinesterase (AChE) enzyme inhibition studies

5.4.3.2.1. *In-vitro* AChE inhibition assay

Inhibitory activities of the target compounds against rat AChE was tested by the spectrophotometric method of Ellman *et al.* but with minor modifications using donepezil

and tacrine as reference standards. The IC_{50} values for AChE inhibition are summarized in **Table 5.26.**

Table 5.26. *In-vitro* and computational AChE inhibition data for compounds **HPO-1** to **HPO-1**

Code	*In-vitro*	Computational	
	IC_{50} (µM) ± SEM	**ΔG (kcal mol^{-1})**	**K_i (µM)**
HPO-1	195.8 ± 2.77	-4.16	890.39
HPO-2	44.44 ± 1.85	-5.37	115.84
HPO-3	3.529 ± 0.093	-6.29	24.61
HPO-4	3.599 ± 0.079	-5.86	50.27
HPO-5	6.527 ± 0.097	-5.84	52.19
HPO-6	11.73 ± 1.138	-5.61	77.77
HPO-7	2.361 ± 0.069	-6.26	25.61
HPO-8	1.736 ± 0.058	-6.45	18.63
HPO-9	0.967 ± 0.004	-6.97	7.72
HPO-10	3.894 ± 0.094	-6.11	33.35
HPO-11	4.401 ± 0.28	-5.91	46.2
HPO-12	14.49 ± 1.65	-5.29	131.96
HPO-13	7.215 ± 0.55	-5.94	44.27
HPO-14	34.82 ± 1.41	-5.63	74.09
DNP	0.021 ± 0.005	-6.01	39.45
TRN	0.225 ± 0.04	-	-

Reference inhibitors: DNP – Donepezil, TRN – Tacrine.

Note: Each IC_{50} value is the mean ± SEM. It refers to the assay concentration of test compound which leads to 50% inhibition of enzyme activity. Level of statistical significance: $P < 0.05$ versus the corresponding IC_{50} values obtained against AChE; as determined by ANOVA/Dunnett's.

All the synthesized compounds (**HPO-1** to **HPO-14**) were found to show activity against AChE displaying inhibition abilities in micromolar range. Among them, **HPO-9** was obtained as the lead candidate showing highest inhibition with IC_{50} value of 0.9672 ± 0.004 µM, which is ~46-fold less potent as compared to donepezil and ~4.3-fold less

potent in comparison to tacrine; followed by **HPO-8** and **HPO-7** with IC_{50} values of 1.736 ± 0.058 µM and 2.361 ± 0.069 µM respectively. All these compounds (**HPO-9**, **HPO-8** and **HPO-7**) possessed both chloro and bromo substitution or two bromo substitution in the ligand.

A careful insight and analysis of the data listed in **Table 5.26.** led to several eventual structure-activity relationships (SAR).

Structure-activity relationship (SAR)

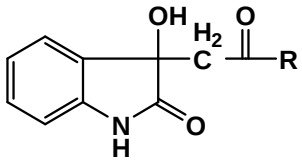

(HPO-1 to HPO-7)

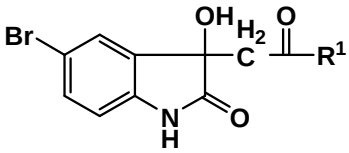

(HPO-8 to HPO-12)

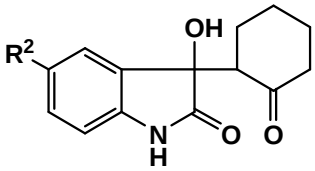

(HPO-13 to HPO-14)

- The variations in the electronic and steric features afforded by the presence of various mono- (**HPO-3** to **HPO-6**, **HPO-8** to **HPO-12**) or disubstituted phenyl ring (**HPO-7**) or cyclohexanone ring (**HPO-13** to **HPO-14**) at C3 significantly influenced the AChE inhibitory profile of these compounds.
- 5-Bromoisatin substituted analogues were found to be more potent than the isatin substituted analogues.
- Interestingly, the 4-chloro-substituted analogue (**HPO-9**) was found to be the most potent AChE inhibitor among the other analogues. This potential activity and selectivity can be attributed to the presence of 4-chloro substitution on the phenacyl side chain and the presence of bromo group at position 5 of the isatin moiety.
- However, bromo (**HPO-8**) and fluoro (**HPO-10**) substitutions on the phenacyl side chain along with the presence of bromo group at position 5 of the isatin moiety resulted in slight reduction in the inhibitory potency against AChE which may be because of the variation in the electronic property imparted by these groups.

- ❖ Dibromo substitution on the phenacyl side chain (**HPO-7**) decreased the potency against AChE compared to **HPO-9**.
- ❖ Hydroxy substitution also reduced the potency towards AChE (**HPO-11**).
- ❖ Moreover, nitro (**HPO-6** and **HPO-12**) substitution on the phenacyl side chain resulted in excessive decrease in the inhibitory potency against AChE.
- ❖ However, unsubstituted phenyl ring on the phenacyl side chain (**HPO-2**) also decreased the potency.
- ❖ Replacement of phenyl group at phenacyl side chain by methyl group (**HPO-1**) abolished the AChE activity.
- ❖ Introduction of unsubstituted isatin incorporated with cyclohexanone ring at position 3 (**HPO-13**) was found to be more potent towards AChE while substitution of isatin moiety with bromo group at position 5 was less potent (**HPO-14**).
- ❖ The presence of rigid -CH_2-CO- linker may contribute to the variations in the results towards AChE inhibitory activity.

5.4.3.2.2. Kinetic study of lead AChE inhibitor HPO-9

To gain further insight into the mechanism of action of this family of compounds on AChE, kinetic studies were carried out with the most promising compound **HPO-9**, using rat brain AChE. Graphical analysis of the reciprocal Lineweaver-Burk plots (**Figure 5.41. (A)**) showed both increased slopes (decreased V_{max}) and intercepts (higher K_m) at increasing concentration of the inhibitor. This pattern indicates a competitive-type inhibition.

5.4.3.2.3. Reversibility and irreversibility experiment for lead AChE inhibitor HPO-9

Further, the most active AChE inhibitor, **HPO-9**, was subjected to time-dependent inhibition studies to investigate whether the observed enzyme inhibition is reversible or irreversible. As shown in **Figure 5.41. (B)**, there is no time-dependent reduction in the rates of AChE catalyzed oxidation of acetylthiocholine iodide (ACTI) when **HPO-9** was preincubated with the AChE for various periods of time i.e. 0, 15, 30, and 60 min (**Figure 5.41. (B)**). From this result it may be concluded that the inhibition of AChE is reversible,

at least for the time period (60 min). An increase of AChE catalytic rates with increased preincubation time of **HPO-9** with the enzyme was observed.

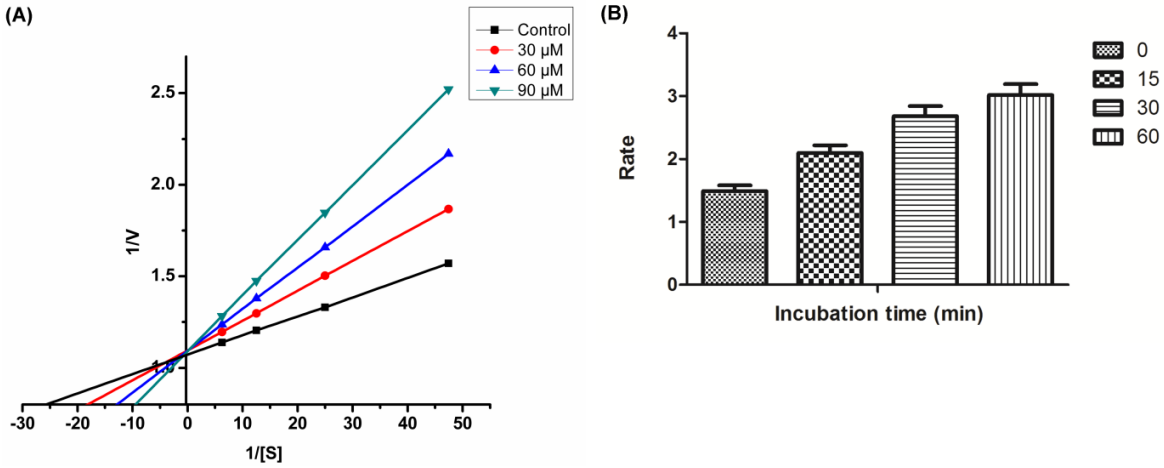

Figure 5.41. (A) Kinetics of rat brain AChE inhibition by **HPO-9**. Lineweaver-Burk plot of the rat brain AChE catalyzed oxidation of ACTI in the absence (control) and presence of various concentrations of **HPO-9** (30 µM, 60 µM, 90 µM). (B) Time-dependant inhibition of AChE catalyzed oxidation of ACTI by compound **HPO-9**. Rate data are expressed as nmol product formed/min/mg protein.

5.4.3.2.4. Molecular docking studies of AChE inhibitors

To further investigate the binding orientation of inhibitors, molecular docking study was performed using AutoDock 4.2. The X-ray crystal structure of the recombinant human AChE (rhAChE) in complex with donepezil (PDB code: 4EY7) was obtained from the Protein Data Bank. The results of molecular docking studies for AChE is expressed in terms of theoretical inhibition constants (K_i values) and estimated free energies of binding (ΔG) for each virtual enzyme-inhibitor complex and are shown in **Table 5.26.**

5.4.3.2.4.1. Pose analysis of AChE inhibitors

Examination of the computationally docked binding poses of all compounds within the AChE active site resulted in the following observations: All the test inhibitors were found to fit into the gorge of AChE formed by catalytic anionic site (CAS) and peripheral anionic site (PAS) and were enclosed by the residues Asp74, Trp86, Gly121, Gly122, Tyr124, Ser125, Gly126, Tyr133, Glu202, Ser203, Ala204, Trp236, Trp286, Phe295, Arg296, Phe297, Tyr337, Phe338, Tyr341, His447 (**Figure 5.42.).** All the test inhibitors

were found to occupy both the catalytic anionic site and the peripheral anionic site (PAS) (**Figure 5.42.**). Superimposition of the reference drug donepezil within the AChE binding site revealed that almost all the test inhibitors exhibit a similar binding orientation to donepezil. Further, these inhibitors are stabilized by hydrogen bonding (H-bond) and π – π stacking interactions.

All compounds showed one or more H-bond interactions. H-bond interaction with residue Asp74 was observed with **HPO-1, HPO-2, HPO-4 and HPO-9**; likewise with Trp86 in **HPO-12**; with Tyr124 in **HPO-4**, **HPO-7**, **HPO-10**, **HPO-11** and **HPO-14**; with Gly122 and Ala204 in **HPO-6**; with Ser293 in **HPO-13**; with Ser298 in **HPO-10**; with Phe295 in **HPO-5**, **HPO-10**, **HPO-11**, **HPO-12**, **HPO-13** and **HPO-14**; with Arg296 in **HPO-5** and **HPO-13**; with Tyr337 in **HPO-1**, **HPO-2** and **HPO-9**; and with Tyr341 in **HPO-3**, **HPO-6** and **HPO-8**. In addition, all the compounds showed π – π interactions. π – π interaction with residue Trp86 was observed in HPO-1, HPO-2, HPO-8, HPO-9 and HPO-12; likewise with Trp286 in **HPO-10**; with Phe297 in **HPO-6**; with Tyr337 in **HPO-3**; with Phe338 in **HPO-5** and **HPO-8**; and with Tyr341 in **HPO-4**, **HPO-6**, **HPO-7**, **HPO-10**, **HPO-11**, **HPO-12** and **HPO-14**. In addition, π – σ interactions were observed with Phe297 in **HPO-10**; likewise with Tyr337 in **HPO-10** and **HPO-14**; and with Tyr341 in **HPO-13** and **HPO-14**.

5.4.3.2.4.2. Binding mode of lead AChE inhibitor HPO-9

Assessment of the virtual complex of the lead AChE inhibitor **HPO-9** and AChE (**Figure 5.43. (A)**) revealed that the entire molecule occupies the active site cavity gorge of the AChE receptor spanning both the PAS and the CAS, whereas the $–CH_2–C=O$ linker was situated in the middle of the gorge between CAS and PAS. The benzene ring of oxindole was involved in π – π interaction with both the rings of Trp86 at an inter-plane distance of approximately 4.73 Å and 5.78 Å respectively. Besides this, the H atom of NH of dioxole ring was bridged to O of Asp74; and H of 3-OH of oxindole moiety was found to bridge with O of OH of Tyr337 *via* H-bonding (**Figure 5.43. (A)**). Superimposition of rhAChE: **HPO-9** complex with the rhAChE:donepezil complex suggests that **HPO-9** mimics the binding mode of donepezil (**Figure 5.43. (B)**).

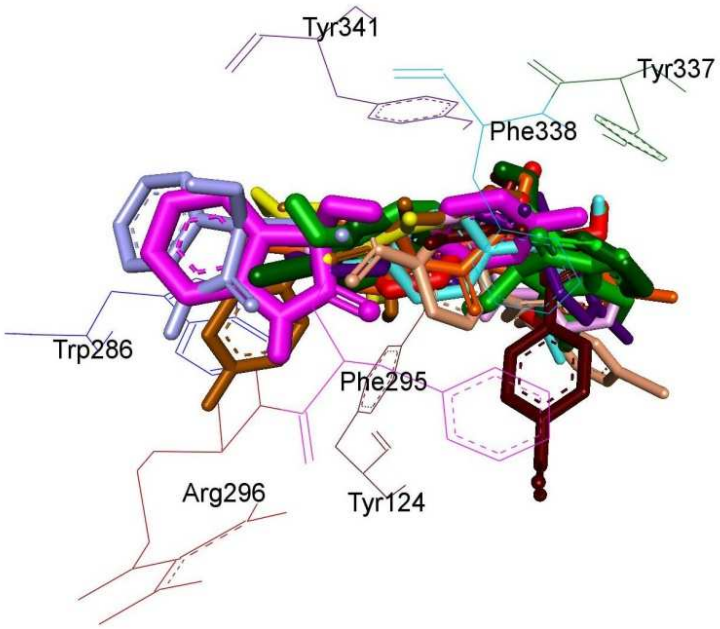

Figure 5.42. Structural screenshot of superimposed AChE inhibitors docked into the active site of AChE. Selected amino acids are depicted in black. **HPO-1**, **HPO-2**, **HPO-3**, **HPO-4**, **HPO-5**, **HPO-6**, **HPO-7**, **HPO-8**, **HPO-9**, **HPO-10**, **HPO-11**, **HPO-12**, **HPO-13** and **HPO-14** are displayed in fluorescent green, red, dark green, light pink, dark pink, dark brown, dark violet, dark orange, fluorescent blue, light brown, parrot green, skin, gray and yellow color respectively.

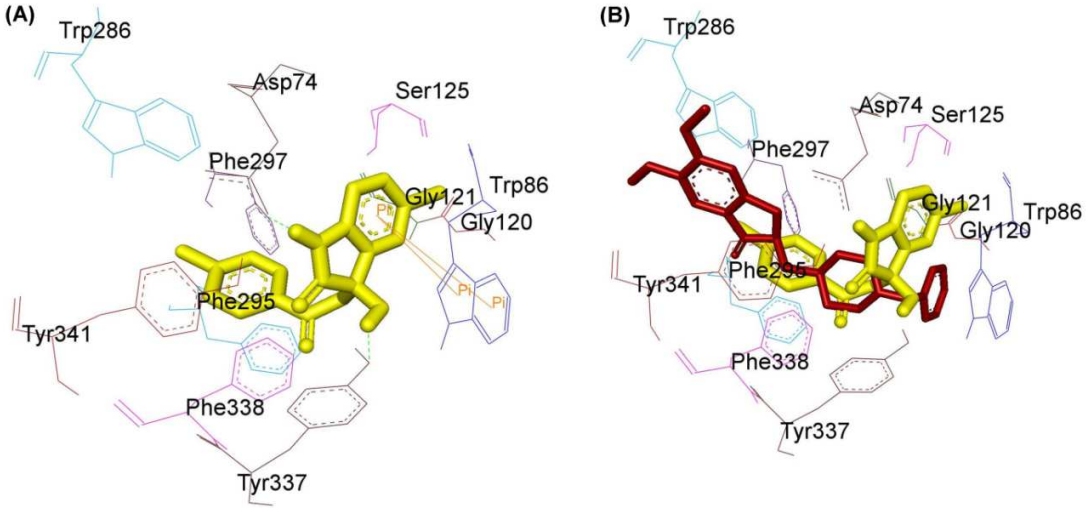

Figure 5.43. Structural screenshot of superimposed AChE inhibitors docked into the active site of AChE. Selected amino acids are displayed in black. (A) Binding orientation of **HPO-9** (yellow) within AChE active site showing π – π (orange colored lines) and H-

bond (green dashes) interactions. (B) Superimposed binding mode of **HPO-9** (yellow) in AChE originally docked with donepezil (maroon).

5.4.3.3. Behavioural studies

5.4.3.3.1. Antidepressant activity (Porsolt's forced swim test)

The synthesized compounds were also evaluated for the antidepressant activity using Porsolt's forced swim test and the results are presented in **Figure 5.44.** The compounds **HPO-9**, **HPO-7** and **HPO-3** were found to be most active compounds among the series but less active than citalopram (CIT), thereby indicating that these compounds produce less CNS depression. Rest of the compounds were found to emerge as CNS depressants as they increased the immobility time.

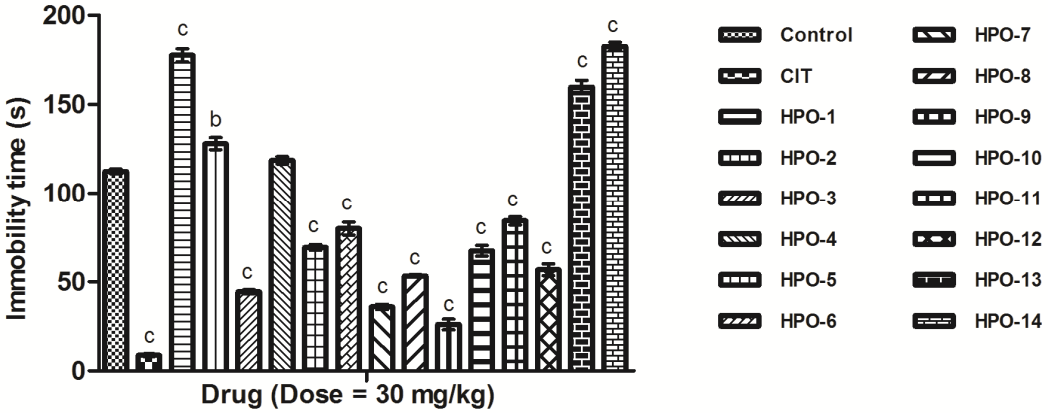

Figure 5.44. Antidepressant activity of 3-hydroxy-3-substituted oxindole analogues of isatin. The results are expressed as mean ± SEM (*n = 6*). The statistical significance was calculated by one-way ANOVA followed by Dunnett's test. CIT – Citalopram. $^{b}P < 0.01$, $^{c}P < 0.001$ when compared with control group.

5.4.3.3.2. Anxiolytic activity (Elevated plus maze test)

All the compounds were subjected to anxiolytic activity using Elevated plus maze apparatus and the results are presented in **Figure 5.45.** Compounds **HPO-9, HPO-7, HPO-3 and HPO-6** possessed greater anxiolytic activity than diazepam (DZM). **HPO-12** expressed potency equivalent to diazepam. Rest of the compounds was found to be less active than diazepam.

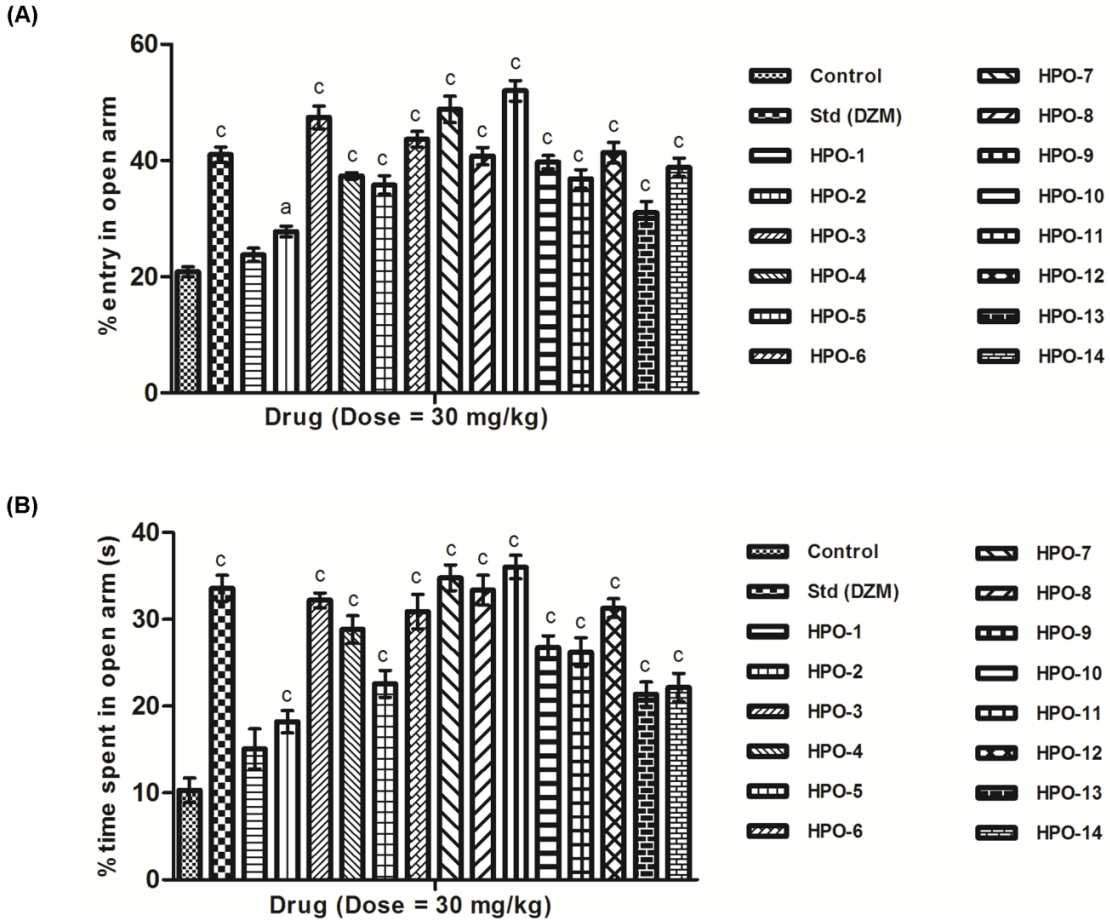

Figure 5.45. Anxiolytic activity of 3-hydroxy-3-substituted oxindole analogues of isatin. The results are expressed as mean ± SEM (*n* = *6*). The statistical significance was calculated by one-way ANOVA followed by Dunnett's test. DZM – Diazepam. $^{c}P < 0.001$ when compared with control group.

5.4.3.3.3. Sedative-hypnotic activity (Pentobarbitone potentiation test)

All the synthesized compounds were evaluated in sedative and hypnotic test at a dose of 30 mg/kg and the results are presented in **Figure 5.46.** Most of the compounds showed significant variation from control. None of the compounds except **HPO-6** and **HPO-8** resulted in elongation of mean sleeping time than control confirming that all compounds except **HPO-6** and **HPO-8** do not potentiate narcosis. Thus, all the compounds except **HPO-6** and **HPO-8** showed antagonistic properties to barbiturates indicating that they lack the sedative side effect.

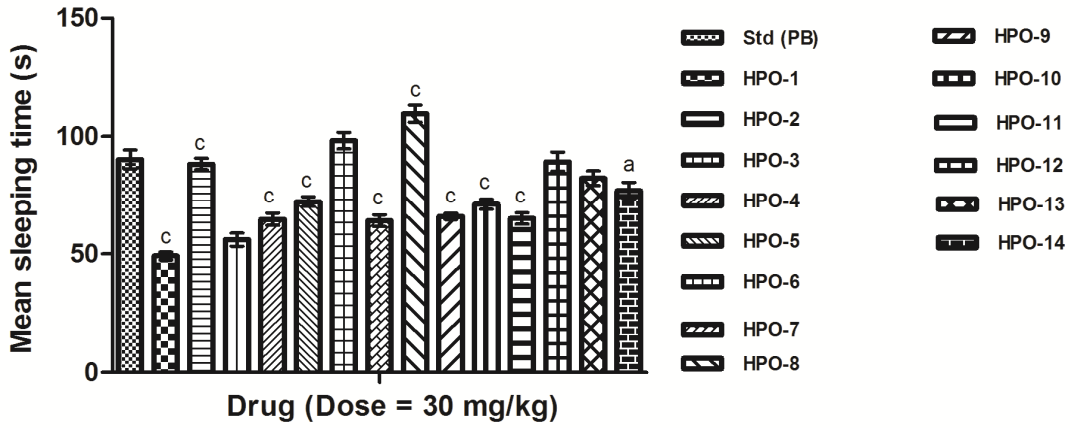

Figure 5.46. Sedative hypnotic activity of 3-hydroxy-3-substituted oxindole analogues of isatin. The results are expressed as mean ± SEM (*n = 6*). The statistical significance was calculated by one-way ANOVA followed by Dunnett's test. PB – Pentobarbitone . $^{a}P < 0.05$, $^{c}P < 0.001$ when compared with control group.

5.4.3.4. Neurotoxicity screening (Rotarod test)

Selected compounds were screened for neurotoxicity by rotarod apparatus at a dose of 30 mg/kg at four time intervals viz. 0.5 h, 1 h, 2 h and 4 h. The results are presented in **Table 5.27.** Among the tested compounds, all compounds were found to be non-neurotoxic except **HPO-12**. Compound **HPO-12** was found to be moderately neurotoxic compared to standard drug phenytoin (PHT).

Table 5.27. Neurotoxicity screening results of selected compounds of **HPO** series

Code	Neurotoxicity (Time in h)*			
	0.5	**1**	**2**	**4**
HPO-3	0/4	0/4	0/4	0/4
HPO-7	0/4	0/4	0/4	0/4
HPO-8	0/4	0/4	0/4	0/4
HPO-9	0/4	0/4	0/4	0/4
HPO-10	0/4	0/4	0/4	0/4

HPO-11	0/4	0/4	0/4	0/4
HPO-12	1/4	1/4	2/4	0/4
PHT	0/4	0/4	0/4	0/2

* The figures indicate the number of animals exhibiting toxicity/total number of animals tested. Reference drug: PHT – Phenytoin

5.4.3.5. Antioxidant activity (DPPH radical scavenging assay)

The percentage antioxidant activity of some of the selected compounds is listed in **Table 5.28.** The DPPH· radical was scavenged by antioxidants *via* donation of hydrogen resulting in the formation of DPPH-H·. The colour of the DPPH is changed from purple to yellow after reduction, which was quantified by the decline of absorbance at a wavelength of 517 nm. From the experimental results, the enhancement in the antioxidant activity is observed for **HPO-7**, **HPO-9** and **HPO-10** (**Table 5.28.**).

Table 5.28. Antioxidant activity data of selected compounds of **HPO** series

Code	% inhibition	Code	% inhibition
HPO-3	50.77	**HPO-9**	63.76
HPO-4	42.71	**HPO-10**	61.35
HPO-5	56.23	**HPO-11**	55.29
HPO-6	28.02	**HPO-12**	28.92
HPO-7	62.03	**Ascorbic acid**	61.24
HPO-8	44.70		

The statistical significance was calculated by one-way ANOVA followed by Dunnett's test. $P < 0.05$ when compared with control.

5.4.3.6. Liver toxicity studies

Enzyme estimation and histopathological studies of the selected compounds were done to check the magnitude of liver toxicity.

5.4.3.6.1. Assessment of liver function

Table 5.29. shows the liver function results with reference to most potent compounds **HPO-7** and **HPO-9**. The estimation revealed that there was no significant increase in SGOT, SGPT, ALP and decrease in protein level in serum in **HPO-9** as compared to the control level while SGPT, ALP and total protein level in **HPO-7** was found to exceed the limits. Results indicated that compound **HPO-7** showed malfunctioning or toxicity of the liver whereas **HPO-9** was found to be non-toxic to liver as compared to control.

Table 5.29. Estimation of biochemical parameters of **HPO-7** and **HPO-9**

Code	SGOT[a] (U/L)	SGPT[b] (U/L)	ALP[c] (U/L)	Albumin (g/dl)	Globulin (mg/dl)	Total protein (g/dl)
Range	25.8-80.8	17.5-90	62-190	3.3-4.8	1.5-3.5	5.2-7.6
HPO-7	80.3±2.53	112.87±2.17	273.6±1.43	4.53±0.17	3.56±0.08	8.13±0.23
HPO-9	39.86±1.35	95.1±1.5	146.26±1.85	2.93±0.14	3.13±0.14	5.36±0.26
Control	38.56±1.62	51.73±2.17	151.56±2.75	3.9±0.12	1.86±0.14	6.8±0.17

Results are expressed as Mean ± SEM. The mean level was calculated using ANOVA followed by Dunnett's test; [a]Serum glutamate oxaloacetate transaminase (SGOT); [b]Serum glutamate pyruvate transaminase (SGPT); [c]Serum alkaline phosphatase (ALP)

5.4.3.6.2. Liver histopathological studies

The Lucas technique was used to access the livers of rat, which was administered with test compounds at the dose level of 30 mg/kg body weight for 15 days and a comparison was done with the control group. Liver samples from **HPO-7** were found to show signs of hepatotoxicity though less than CCl_4-treated liver samples. While liver samples from **HPO-9** were within normal histopathological limits (**Figure 5.47.**)

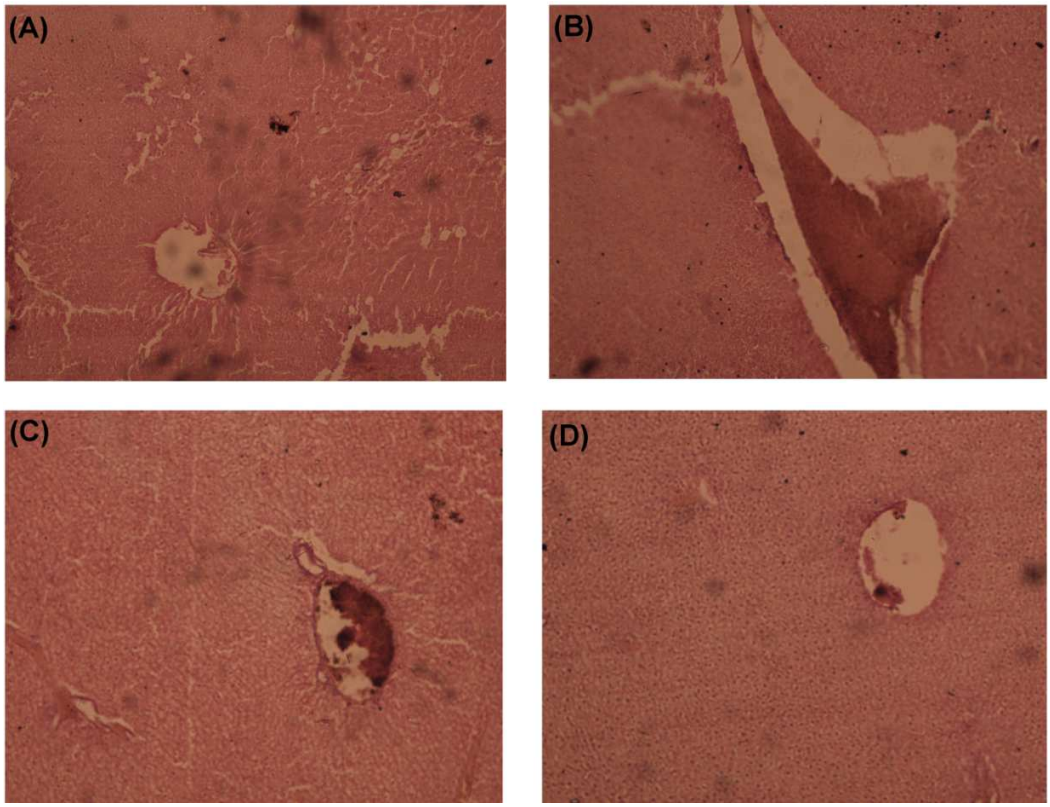

Figure 5.47. Microphotograph of the section of hematoxylin and eosin stained rat liver. Group: (A) Control (B) CCl_4-treated (C) **HPO-7** (D) **HPO-9**. Magnification: 10x.

5.4.4. *In-silico* molecular property and ADMET prediction studies

All the structural elements were selected to check their adherence to Lipinski's rules for possible drug-likeness using molinspiration software (**Table 5.30.**).

The lipophilicity (expressed as MiLogP) predicted were found to be well the traditionally cut-off value of 5 indicating that none of the compounds violated the Lipinski's rules. All the structures show suitable MW values (MW < 500) necessary for a successful penetration to CNS. The topological polar surface area (TPSA) was observed to be in the range 66.40-112.22 $Å^2$ which is well below the limit of 160 $Å^2$. Thus, the predicted values for all compounds **HPO-1** to **HPO-14** fall into the appropriate range indicating good bioavailability of the drug molecule. The number of hydrogen bond acceptors (HBA) and donors (HBD) for all the compounds were in accordance with the Lipinski's rule of five. Thus it was predicted that almost all compounds are likely to be orally active.

Table 5.30. *In-silico* drug-likeness[a] prediction data for **HPO-1** to **HPO-14**

Code	MW	MiLogP	TPSA	HBA	HBD	$n_{violations}$	Volume
Rule	<500	≤5	<160 Å^2	≤10	≤5	≤1	
HPO-1	205.21	0.14	66.40	4	2	0	181.46
HPO-2	267.28	1.74	66.40	4	2	0	236.30
HPO-3	346.18	2.55	66.40	4	2	0	254.19
HPO-4	301.73	2.42	66.40	4	3	0	249.84
HPO-5	285.27	1.91	66.40	4	2	0	241.23
HPO-6	312.28	1.70	112.22	7	2	0	259.64
HPO-7	425.08	3.29	66.40	4	2	0	272.07
HPO-8	425.08	3.34	66.40	4	2	0	272.07
HPO-9	380.62	3.21	66.40	4	2	0	267.72
HPO-10	364.17	2.69	66.40	4	2	0	259.12
HPO-11	362.18	2.05	86.62	5	3	0	262.21
HPO-12	391.18	2.49	112.22	7	2	0	277.52
HPO-13	245.28	1.28	66.40	4	2	0	221.29
HPO-14	324.17	2.06	66.40	4	2	0	239.17

[a]MW = Molecular weight, MiLogP = octanol-water partition coefficient, TPSA = Topological Polar Surface Area, HBA = Number of hydrogen bond acceptor, HBD = Number of hydrogen bond donor, $n_{violations}$ = violations from Lipinski's rule

The results of ADMET prediction studies are listed in **Table 5.31.** and **Table 5.32.** respectively.

Human intestinal absorption (HIA) property is the determinant for those drugs that purport oral administration. All the compounds **HPO-1** to **HPO-14** expressed greater than 70% HIA values indicating good permeation across the membrane.

The *in-vitro* Caco-2 cell permeability is an important parameter to assess intestinal absorption of the drug since Caco-2 cells are derived from human colon adenocarcinoma, possessing transports *via* the intestinal epithelium. The results indicated that all compounds **HPO-1** to **HPO-14** exhibited moderate permeation.

The *in-vitro* MDCK cell permeability test utilizes canine kidney cells for the analysis of permeability. All the compounds except **HPO-2**, **HPO-4** and **HPO-5** showed permeation less than 25 nm/s indicating low permeability. **HPO-2**, **HPO-4** and **HPO-5** showed moderate permeability for MDCK cell**.**

The skin permeability is an important factor for the delivery of drug *via* transdermal administration. All the compounds **HPO-1** to **HPO-14** exhibited negative permeability values, indicating that transdermal mode of administration is not the suitable means to administer these drugs.

Table 5.31. *In-silico* ADME prediction data[a] for compounds **HPO-1** to **HPO-14**

Code	Absorption				Distribution	
	HIA (%)	***In-vitro* CP (nm/s)**	***In-vitro* MDCK (nm/s)**	***In-vitro* SP (log K_p, cm/h)**	***In-vitro* PPB (%)**	***In-vivo* BBB (C_{brain}/C_{blood})**
Rule	0-20 (poor) 20-70 (moderate) 70-100 (well)	<4 (low) 4-70 (moderate) >70 (high)	<25 (low) 25-500 (moderate) >500 (high)		>90 (strongly bound) <90 (weakly bound)	>0.1 (CNS active) <0.1 (CNS inactive)
HPO-1	89.66	19.03	2.11	-4.55	26.28	0.33
HPO-2	92.92	20.15	144.03	-3.49	87.62	0.53
HPO-3	94.46	20.55	3.71	-3.27	91.39	0.36
HPO-4	93.86	20.73	137.24	-3.39	86.33	0.33
HPO-5	92.93	20.9	56.66	-3.72	85.98	0.18
HPO-6	86.71	17.49	14.21	-3.65	84.15	0.01
HPO-7	95.57	19.85	0.57	-3.02	100.00	0.89

HPO-8	95.57	19.85	0.26	-2.98	91.86	0.88
HPO-9	95.18	20.33	0.43	-3.22	95.49	0.78
HPO-10	94.47	20.58	0.21	-3.51	96.29	0.38
HPO-11	91.94	20.41	0.29	-3.91	94.34	0.38
HPO-12	94.58	18.15	0.06	-3.49	97.05	0.01
HPO-13	91.32	20.89	21.98	-4.26	58.82	0.46
HPO-14	93.39	15.59	1.88	-4.07	82.53	0.76

[a]HIA – Human Intestinal Absorption, CP – Caco2 cell permeability, MDCK – MDCK cell permeability, SP – skin permeability, PPB – Plasma protein binding, BBB – Blood brain barrier.

The percent of drug bound with plasma proteins was estimated and **HPO-1**, **HPO-2**, **HPO-4**, **HPO-5**, **HPO-6**, **HPO-13** and **HPO-14** were predicted to bind weakly to plasma proteins, thereby, indicating that the compounds will be available for diffusion or transport across cell membranes and hence finally interact with the target. While rest of the compounds were strongly bound to plasma proteins.

Predicting BBB penetration means predicting whether compounds pass across the blood-brain barrier. According to the computed values; all the compounds except **HPO-12** were predicted to be CNS active and could be good candidates for CNS penetration.

The Ames test assesses mutagenicity of the compounds. All the compounds were predicted as mutagen. Besides, carcinogenicity test was performed to identify the tumerogenic potential of compounds in animals (mouse and rat). When analyzing carcinogenicity in mice, all the compounds were predicted as negative. By analyzing rat carcinogenicity, compounds **HPO-3** and **HPO-10** were predicted positive while rest of the compounds presented negative predictions. Human ether-a-go-go-related gene (hERG) encodes potassium channels, which are responsible for normal repolarisation of cardiac action potentials. Blockage or any other impairment of these channels in the heart can lead to fatal cardiac problems. Hence, drug-induced blockage of potassium channels has been a major concern. All the compounds presented medium risk except **HPO-1**, **HPO-2**, **HPO-13** and **HPO-14** which presented low risk against hERG inhibition.

Table 5.32. *In-silico* toxicity prediction data of compounds **HPO-1** to **HPO-14**

Code	Ames test	Carcinogenicity (Mouse)	Carcinogenicity (Rat)	hERG inhibition
HPO-1	Mutagen	Negative	Negative	Low risk
HPO-2	Mutagen	Negative	Negative	Low risk
HPO-3	Mutagen	Negative	Positive	Medium risk
HPO-4	Mutagen	Negative	Negative	Medium risk
HPO-5	Mutagen	Negative	Negative	Medium risk
HPO-6	Mutagen	Negative	Negative	Medium risk
HPO-7	Mutagen	Negative	Negative	Medium risk
HPO-8	Mutagen	Negative	Negative	Medium risk
HPO-9	Mutagen	Negative	Negative	Medium risk
HPO-10	Mutagen	Negative	Positive	Medium risk
HPO-11	Mutagen	Negative	Negative	Medium risk
HPO-12	Mutagen	Negative	Negative	Medium risk
HPO-13	Mutagen	Negative	Negative	Low risk
HPO-14	Mutagen	Negative	Negative	Low risk

To sum up, despite other compounds exhibiting good brain penetration profiles, it can be concluded that **HPO-9** presented the best drug-like characteristics and ADMET properties among all the compounds of the series.